Научном већу Института за физику у Београду

Београд, 05.08.2020.

Предмет: Покретање поступка за избор у звање истраживач сарадник

Молим Научно веће Института за физику у Београду да покрене поступак за мој избор у звање истраживач сарадник.

У прилогу достављам:

1. мишљење руководиоца лабораторије са предлогом комисије за избор у звање;
2. стручну биографију;
3. преглед научне активности;
4. списак и копије објављених научних радова и публикација;
5. уверење о последњем овереном и уписаном семестру на докторским студијама;
6. фотокопију диплома са основних и мастер студија;
7. потврду о прихватању предлога теме докторске дисертације.

С поштовањем,

Јелена Митрић
истраживач приправник

Научном већу Института за физику у Београду

Београд, 05.08.2020.

Предмет: Мишљење руководиоца лабораторије о избору Јелене Митрић у звање истраживач сарадник

Јелена Митрић је запослена у Лабораторији за истраживање у области електронских материјала Института за физику у Београду. У поменутој лабораторији ради на темама из области физике и физичке хемије чврстог стања, нарочито на полупроводничким наноматеријалима, њиховој синтези и структурној и оптичкој карактеризацији. С обзиром да испуњава све предвиђене услове у складу са Правилником о поступку, начину вредновања и квантитативном исказивању научноистраживачких резултата МПНТР, сагласан сам са покретањем поступка за избор Јелене Митрић у звање истраживач сарадник.

За састав комисије за избор Јелене Митрић у звање истраживач сарадник предлажем:

(1) др Небојша Ромчевић, научни саветник, Институт за физику у Београду,
(2) др Јелена Трајић, виши научни сарадник, Институт за физику у Београду,
(3) ванр. проф. Ивана Стојковић – Симатовић, ванредни професор Факултета за физичку хемију Универзитета у Београду.

др Небојша Ромчевић
научни саветник
руководилац Лабораторије за истраживање у области електронских материјала Института за физику

Биографија

Јелена (Миодраг) Митрић рођена је 03. јула 1993. године у Београду, Република Србија. Основне студије на Факултету за физичку хемију Универзитета у Београду уписала је 2012. године, а завршила 2016. године одбраном дипломског рада под називом „Оптимизација услова јонске измене Fe^{3+} јонима у циљу контролисања њихове дисперзије у зеолиту ZSM – 5". За исти рад добила је награду фондације *Сестре Булајић* за најбоље одбрањен дипломски рад у области физичке хемије. Исте године је уписала мастер академске студије Факултета за физичку хемију и завршила их 2017. године, одбранивши рад „Карактеризација сребром измењених и дехидратисаних зеолита типа А и Х". Од 2017. године је студент докторских студија Факултета за физичку хемију. Од 2019. године је студент мастер академских студија на Рударско – геолошком факултету, на смеру *Минералогија и кристалографија*.

На Институту за физику је запослена од 2018. године у *Лабораторији за истраживања у области оптоелектронских материјала*. Од 2017. године ангажована је на националном пројекту „Оптоелектронски нандоимензиони системи – пут ка примени" (ИИИ 45003, руководилац др Небојша Ромчевић, научни саветник). Јелена се у склопу своје докторске дисертације бави синтезом и оптичком и структурном карактеризацијом полупроводничких нискодимензионих материјала. У новембру и децембру 2016. године боравила је у Љубљани (Словенија) у Јожеф Стефан институту у Лабораторији за нове материјале на студенској пракси. У априлу 2017. године боравила је у Загребу, у Институту за физику у Лабораторији за кохерентну оптику, где је вршила истраживања на мембранама од графена. Током 2019. пет месеци је провела у Гранади, Шпанија (у склопу ERASMUS организације) у Геолошком институту у Лабораторији за кристалографију где се бавила синтезом и карактеризацијом биоморфа баријум - сулфата и калцијум - карбоната. До сада је била стипендиста Министарства образовања, науке и технолошког развоја Републике Србије у школским 2013/2014, 2014/2015 и 2015/2016. годинама. Коаутор је 15 научних радова и саопштења.

Преглед научне активности

Јелена Митрић се у свом досадашњем научном раду бави истраживањем структурних и оптичких својстава различитих полуопроводничких наноматеријала, нарочито из халкогенидне групе елемената, оксида и телурида. Посебан акценат дат је на разматрању утицаја смањења димензије са балк на нанокристал на њихове структурне и оптичке особине.
Досадашња истраживања тицала су се четири важна представника халкогенидних полупроводничких наноматеријала из групе оксида и телурида и то:

1. гадолинијум – цирконат,
2. итријум – ванадат,
3. кадмијум – телурид и
4. цинк оксид (модификован рутенијумовим комплексима)

Фононске особине балк кристала су од изузетне важности за разумевање вибрационих особина малих честица. Као последица минијатуризације (преласка са балк кристала на нанокристал), очекују се промене у вибрационим спектрима, померање и ширење модова нанокристала у односу на балк кристал, што ће бити и праћено у овом истраживању.
Циљ истраживања је регистровање различитих нанообјеката у различитим полупроводничким наноматеријалима синтетисаним различитим методама и описивање њихових структурних и оптичких промена у односу на балк материјале.

Комплексни оксидни и халкогенидни полупроводнички наноматеријали су материјали који, као што је речено, имају широке примене у свим пољима индрустрије и технологије. Иако је интересовање за њих започело већ пре више од три деценије, они не престају да се интензивно користе како у биомедицинским истраживањима, тако и у конверзији соларне енергије, наноелектронским уређајима, ласерској технологији, таласоводима, хемијским и биосензорима, суперапсорберима, компонентама за војну опрему и др. Како технологија напредује, ови материјали иако већ веома популарни, постаће још актуелнији, што сведоче стотине радова на тему полупроводничких наноматеријала, објављених само у последњих неколико година.

Међу овим материјалима издвајају се изабране структуре које се испитују у овој дисертацији, попут **гадолинијум-цирконата** који припада важној групи пирохлора који имају бројне примене попут: складиштења нуклеарног отпада, електро/фото катализи, луминисценцији, хемисорпцији CO_2, фотолуминисценцији и др. Пирохлори засновани на ретким земљама попут гадолинијум-цирконата популарни су због своје ниске термалне проводности и високе фазне стабилности. Јони ретких земаља често се користе као активатори оваквих пирохлора због своје високе чистоће боје, дугог времена

луминисценције и ниског емисионог профила. Такође, познато је да при синтези овако допираних нанопирохлора може доћи до појаве електрон-фонон интеракције и то је показано раманском спектроскопијом, а ова истраживања то потврђују и инфрацрвеном спектроскопијом. У овом истраживању гадолинијум – цирконат се допира јонима еуропијума. Због свих предности које допирани пирохлор гадолинијума пружа, као и због популарности и његове широке примене, изабран је баш овај материјал за испитивање смањења његових димензија на наноскалу и утицај на његове структурне и оптичке особине, чије ће разумевање довести до још лакше и ефикасније примене у многим пољима индустрије, технологије и привреде.

Још један актуелан материјал којим се ова дисертација бави је **итријум-ванадат**. Он припада важној групи вандата због својих примена у фотокатализи, фотолуминисценцији и генерално, фотохемији. Веома је погодна домаћинска решетка за јоне ретких земаља, а у овом случају еуропијума. Јони итријума се лако могу изменити јоном еуропијума у структури итријум-вандата због исте валенце и сличности у пречнику. Ово доводи до интересантног феномена названог *квази -изотопски ефекат* који описује измену јона док се апроксимира константна константа силе, а једино што се мења је маса измећених јона. Овако приказан механизам измене указује на физичкохемијске процесе у оваквим материјалима и омогућава лакше разумевање структурно-оптичких особина оваквих материјала, а самим тим и њихову примену у фотохемији.

Један од популарнијих халкогенидних полупроводника је **кадмијум-телурид**. У овом истраживању показује се синтеза танког филма кадмијум-телурида који има велике примене у конверзији соларне енергије, због свог коефицијента оптичке апсорпције (филм дебљине 2 μm ће апсорбовати скоро 100% упадног зрачења) и због своје скоро идеалне вредности енергетског процепа за фотоволтаичну конверзију од 1,45 eV. С друге стране, електрон-фонон интеракција која је показана у овом истраживању, важна је за полупроводничке материјале. Откриће ових фонона и њихове интеракције утиче на испитивање оптичких и структурних оваквих материјала и њихову примену пре свега у електронским и оптоелектронским уређајима.

Цинк-оксид је са титанијум-диоксидом најпопуларнији полупроводнички наноматеријал. Бројне предности овог материјала чине га веома популарним и применљивим, а због великог броја начина синтезе, поседује најбогатију разноликост наноструктура. Комплекси рутенијума, којима су модификоване наноплочице често су коришћени комплекси у областима повезаним са биомедицинским истраживањима. Изузетна актуелност овог материјала разлог је да се, као и претходни халкогенидни полупроводници, испитује када се синтетише као наноматеријал када ће доћи до промене његових структурних и оптичких особина. Објашњење феномена које се притом дешавају на наноскали ће знатно утицати на проширење његових већ великих примена.

1. **Гадолинијум – цирконат**

Гадолинијум – цирконат ($Gd_2Zr_2O_7$) синтетише се методом сагоревања раствора. Ова метода је изабрана, са једне стране, као брза и једноставна, а са друге, погодна због контролисања величине кристалита узорка, специфичне површине узорка и других карактеристика. Циљ при истраживању овог материјала је откривање потенцијалних феномена унутар наноскале када се његове димензије са балк кристала смање на нанодимензију. Задатак овог дела истраживања је описивање структурно – електронских промена код гадолинијум-цирконата, односно описивање електрон – фонон интеракције до које долази због утицаја смањења димензија кристала.

2. **Итријум – ванадат**

У другом делу истраживања које се бави **итријум-ванадатом**, испитују се феномени унутар наноскале који се тичу измене допантног јона са јоном домаћинске решетке. Показује се како и зашто долази до квази – изотопског ефекта и како то утиче на структурне и оптичке особине овог наноматеријала. Такође, разматран је и утицај две различите методе синтезе нанопрахова: методе сагоревања раствора и класичне керамичке методе, као и утицај допирања на овај метални ванадат.

3. **Кадмијум – телурид**

Трећи део истраживања се бави танким филмовима **кадмијум-телурида,** припремљеним методом термалног напаравања – испитују се интеракције површинског оптичког фонона и плазмона услед смањења димензија балк кристала кадмијум-телурида на нанокристални материјал (танки филм). Такође, разматра се како наведена интеракција утиче на структурне и оптичке особине овог материјала. Између осталог, циљ је и размотрити како дебљина филма утиче на поменуту интеракцију и генерално на структурно – оптичке карактеристике.

4. **Цинк – оксид модификован рутенијумовим – комплексима**

У четвртом делу, код наноплочица **цинк-оксида** модификованим рутенијумовим комплексима, синтетисаних преципитационом методом, карактерише се новодобијени композит, разматра се како модификатори утичу на структурне и оптичке особине почетног материјала цинк-оксида и феномени унутар наноскале који проузрокују оптичке и структурне промене смањењем димензије материјала, а тичу се преноса налектрисања унутар структуре.

Списак објављених научних радова и саопштења

Научни радови објављени у часописима међународног значаја:

<u>У врхунским међународним часописима (категорија M_{21}):</u>

1. **<u>J. Mitrić</u>**, J. Križan, J. Trajić, G. Križan, M. Romčević, N. Paunović, B. Vasić, N. Romčević, *Structural properties of Eu^{3+} doped $Gd_2Zr_2O_7$ nanopowders: Far – infrared spectroscopy*, Optical Materials, 75, 662 – 665, **(2018)**.
2. **<u>J. Mitrić</u>**, U. Ralević, M. Mitrić, J. Ćirković, G. Križan, M. Romčević, M. Gilić, N. Romčević, *Isotope – like effect in $YVO_4:Eu^{3+}$ nanopowders: Raman spectroscopy, Journal of Raman Spectroscopy*, 50, 802 – 808, **(2019)**.
3. J. L. Ristić – Đurović, L. Fernández – Izquierdo, B. Hadžić, L. Jiménez – Hernández, A. M. Díaz – García, **<u>J. Mitrić</u>**, B. Babić, M. Romčević, S. Ćirković, N. Romčević, *Raman spectroscopy of zinc oxide nanoplatelets modified with ruthenium (II) complexes*, Journal of Raman spectroscopy, 1829 – 1838, **(2019)**.

<u>У истакнутим међународним часописима (категорија M_{22})</u>

4. **<u>J. Mitrić</u>**, N. Paunović, M. Mitrić, B. Vasić, U. Ralević, J. Trajić, M. Romčević, W. D. Dobrowolski, I. S. Yahia, N. Romčević, *Surface optical phonon – plasmon interaction in nanodimensional CdTe thin films*, Physica E: Low – dimensional Systems and Nanostructures, 104, 64 – 70, **(2018)**.
5. M. Romcevic …., **<u>J. Mitrić</u>**, ..., *Plasmon – Phonon interaction in ZnSnSb2 + Mn semiconductors,* Infrared Physics & Technology, 108, 103345, **(2020)**.

Научна саопштења:

<u>На међународним скуповима штампана у књигама радова (категорија M_{34}):</u>

1. **<u>J. Mitrić</u>** et al., *Digital holography of graphene oxide paper acoustic membranes*, The 6th International School and Conference on Photonics; PHOTONICA2017, 6, 128, Belgrade, Serbia, **2017**.

2. **<u>J. Mitrić</u>**, D. Grujić, D. Abramović, I. Salom, N. Demoli, D. Pantelić, D. Todorović, M.Spasenović, *Digital holography of graphene oxide paper acoustic membranes and comparison to other paper – like materials*, The 16th Young Researches Conference – Materials Science and Engineering, 16, 39, Belgrade, Serbia, **2017**.

3. **<u>J. Mitrić</u>** et al., *Digitalna holografija akustičkih membrana od grafenskog papira*, The 4th International Acoustics and Audio Engineering Congerence, TAKTONS & DOGS, Novi Sad, Serbia, **2017**.

4. **<u>J. Mitrić</u>**, N. Paunović, M. Mitrić, B. Vasić, U. Ralević, J. Trajić, M. Romčević, W. D. Dobrowolski, I. S. Yahia, B. Hadžić, M. Gilić, S. Ćirković, N. Romčević, *Surface optical phonon – Plasmon interaction in nanodimensional CdTe thin films*, 11th Photonics Workshop, Kopaonik, March **2018**.

5. **J. Mitrić**, N. Paunović, M. Mitrić, B. Vasić, U. Ralević, J. Trajić, M. Romčević, W. D. Dobrowolski, Y. S. Yahia, N. Romčević, *Surface optical phonon – Plasmon interaction in Nanodimensional CdTe thin films*, 17th Young Researchers' Conference Materials Science and Engineering, 17, 68, Belgrade, Serbia, **2018.**

6. M. Gilić, **J. Mitrić**, S. Petrović, D. Peruško, J. Ćirković, L. Reissig, N. Romčević, *Optical and Structural Investigations of Cr_2O_3 Thin Films: The Effect of Thickness on Their Applicability in Differential Photodetectors*, PHOTONICA2019, 7, 90, Belgrade, Serbia, **2019**.

7. **J. Mitrić**, N. Paunović, J. Ćirković, M. Gilić, M. Romčević, N. Romčević, *Structural properties of Eu^{3+} doped YVO_4: Far – Infrared Spectroscopy*, PHOTONICA2019, 7, 93, Belgrade, Serbia, **2019**. ***(Award for best Poster Presentation)***

8. **J. Mitrić**, M. Gilić, Z. Lazarević, M. Romčević, N. Romčević, *Isotope – like in YVO_4:Eu^{3+} nanopowders*, 8th Serbian Ceramic Society Conference *Advanced Ceramics and Applications*, Serbian Academy of Sciences and Arts, Knez Mihajlova 35, Belgrade, Serbia, **2019**.

9. M. Gilić, **J. Mitrić**, J. Ćirković, S. Petrović, D. Peruško, L. Reissig, N. Romčević, Optical and structural investigation of Cr2O3 thin films: The effect of thickness for possible application for differential photodetectors; 5th Conference of the Serbian Society for Ceramic Materials, P25 – pp.93, Belgrade, Serbia, **2019**.

10. **J. Mitrić**, B. Hadžić, J. Trajić, S. Ćirković, M. Romčević, N. Romčević, *Structural and optical characterization of europium doped yttrium orthovanadate: isotope – like effect*, 13th Photonics Workshop, Kopaonik, March **2020**.

Optical Materials 75 (2018) 662–665

Contents lists available at ScienceDirect

Optical Materials

journal homepage: www.elsevier.com/locate/optmat

Structural properties of Eu^{3+} doped $Gd_2Zr_2O_7$ nanopowders: Far-infrared spectroscopy

J. Mitrić [a, *], J. Križan [b], J. Trajić [c], G. Križan [b], M. Romčević [c], N. Paunović [c], B. Vasić [c], N. Romčević [c]

[a] School of Computing, University Union, Knez Mihailova 6, Belgrade 11 000, Serbia
[b] AMI, d. o. o., Ptuj, Slovenia
[c] Institute of Physics, University of Belgrade, Pregrevica 118, 11080 Belgrade, Serbia

ARTICLE INFO

Article history:
Received 2 October 2017
Accepted 15 November 2017

Keywords:
$Gd_2Zr_2O_7$
Eu^{3+}
Nanopowders
Phonons
Light absorption and reflection

ABSTRACT

The Solution Combustion Synthesis (SCS) method was used to prepare nanopowders of europium doped cubic $Gd_2Zr_2O_7$ nanopowders. The surface of the samples have been investigated using atomic force spectroscopy (AFM) and far-infrared spectroscopy (FIR). Far-infrared reflectivity spectra of Eu^{3+} doped $Gd_2Zr_2O_7$ nanopowders were measured at room temperature in spectral region between 80 and 650 cm^{-1}. The Maxwell–Garnet formula was used to model dielectric function of Eu^{3+} doped $Gd_2Zr_2O_7$ nanopowders as mixtures of homogenous spherical inclusions in air.

1. Introduction

$A_2B_2O_7$ type of pyrochlores are important class of materials because of their diverse scientific and technological applications like in nuclear waste storage [1], electro/photo catalysis [2,3], luminescence [3], CO_2 hemisorption [4], photoluminescence hosts [5], topological Mott insulator [6] etc.

Pyrochlore oxides which occur in various crystalline phases, manifest numerous interesting and important physicochemical properties which make them eligible for potential hosts for the chemical substitution [7].

Rare earth based zirconates ($Re_2Zr_2O_7$) pyrochlores have wide scientific and technological applications as: potential thermal barrier coatings (TBC), high temperature heating devices or luminescence hosts [8].

Among all rare earth based pyrochlores, $Gd_2Zr_2O_7$ stands out as a material with a distinctively low thermal conductivity and high phase stability [9]. Besides that, $Gd_2Zr_2O_7$ could be an excellent candidate for potential photoactive materials [10].

As shown through our previous work [4,11], there are two different crystal structures for $Gd_2Zr_2O_7$, pyrochlore and the fluorite type.

Rare earth ions are widely used as activators for various phosphors and other organic and inorganic luminescent materials, because they offer high color purity, high luminescence lifetime and also a narrow emission profile, thanks to its optically active 4f electrons which are strongly shielded from the rest of ions by the other 5s and 5p shells [12].

Among all lanthanides, Eu^{3+} ion is in advantage as a dopant ion for structural probing, as well as for synthesis of red light emitting phosphor [8]. The reason this ion is a useful spectroscopic probe is because of its main source of luminescence - single level, $^5D_0$ state, which prevents the convolution of overlapping emission peaks from different levels [13]. Also, doping any aliovalent ion in these oxides is not only used for structural probing, but it could also generate significant changes in photophysical behavior of those materials in such way that doping creates various kinds of defects like ion/oxygen vacancies, which can alter the band gap of materials, i.e. photophysical characteristics of one material. Particularly for $Gd_2Zr_2O_7$, it is proven that efficient doping results in tuning of thermal [14], electrical [15], optical [4] and other properties.

In this paper, we present the results obtained by using far – infrared spectroscopy (FIR) to study optical properties of the Eu^{3+} doped $Gd_2Zr_2O_7$ nanopowders which were prepared by the Solution Combustion Synthesis (SCS) method. The dielectric function of Eu^{3+} doped $Gd_2Zr_2O_7$ nanopowder is modeled as a mixture of

* Corresponding author.
E-mail address: jmitric@ipb.ac.rs (J. Mitrić).

https://doi.org/10.1016/j.optmat.2017.11.026
0925-3467/

homogenous spherical inclusions in air, by the Maxwell-Garnet formula.

2. Sample and characterization

Europium doped cubic $Gd_2Zr_2O_7$ nanopowders were prepared by Solution Combustion Synthesis (SCS) method. Starting chemicals $Gd(NO_3)\cdot 6H_2O$, $Zr(NO_3)_2\cdot H_2O$, $Eu(NO_3)\cdot 6H_2O$ with the purity of 99,99% were purchased from ABCR, Gd_2O_2 (99,9%) from the NOAH Technologies and urea $(NH_2)_2CO$ from Sigma-Aldrich.

Due to its simplicity and low cost of the synthesis procedures and possibility of tailoring the size and morphology of particles, the flame combustion process is the most frequently used. After the synthesis, the nanopowder was annealed, in order to achieve the full crystallinity, in air atmosphere at 1200 °C for 2 h. The Eu^{3+} concentration in $Gd_2Zr_2O_7$ was 2 mol%. The morphology analysis of the synthesized materials indicates the irregular crystallite size distribution and existence of agglomerated grains which are in the submicron size.

In our previous work [4,11] we performed X – ray powder diffraction (XRD) and photoluminescence measurements of the same material. XRD analysis confirmed that sample was crystallized in fluorite (F) type structure (space group Fm3m). The photoluminescence spectra showed a number of electronic transitions, among them were those at 705 nm and 713 nm ($^5D_0 - {}^7F_4$), 654 nm ($^5D_0 - {}^7F_3$), 630 and 611 nm ($^5D_0 - {}^7F_2$), 593 nm ($^5D_0 - {}^7F_1$), 584 nm ($^5D_0/{}^5D_1 - {}^7F_1$) and 578 nm ($^5D_0/{}^5D_1 - {}^7F_0$).

The Raman spectra of Eu^{3+} doped $Gd_2Zr_2O_7$ nanopowders were measured. We registered three phonons at 177 cm^{-1}, 268 cm^{-1} and 592 cm^{-1}, as well as their overtones at 354 cm^{-1}, 445 cm^{-1}, 708 cm^{-1}, 1062 cm^{-1}, 1184 cm^{-1}, ~1530 cm^{-1} and ~1720 cm^{-1}. The phonon at 592 cm^{-1} was already known to be characteristic for $Gd_2Zr_2O_7$ fluorite – type structure, and we found that other two phonon positions to be characteristic with the observed electron – phonon observed interaction and that the registered multiphonon processes were a consequence of miniaturization that further induces changes in electronic structure of Eu^{3+} doped $Gd_2Zr_2O_7$ nanopowders. All the above mentioned results will be useful in the far – infrared spectroscopy analysis of Eu^{3+} doped $Gd_2Zr_2O_7$ nanopowders.

3. Results and analysis

3.1. AFM

Atomic force microscopy (AFM) measurements were done using NTEGRA Prima system from NT-MDT at room temperature and ambient conditions. Imaging was done in tapping mode using NSG01 probes. Phase lag of AFM cantilever was recorded simultaneously during tapping mode imaging.

Two dimensional and three dimensional topography of the sample surface are shown in Fig. 1(a) and (b), respectively (scan size is 5 × 5 μm^2). As can be seen, the surface is rather flat with characteristic holes represented with dark color. Cross section of one characteristic hole (along dashed line in Fig. 1(a)) is given in the inset of Fig. 1(a). Hole width and depth are around 1 μm and 200 nm, respectively. Apart from this holes, the sample surface consists of small grains. They are better visualized in Fig. 1(c) and (d) showing the topography and phase contrast image of a zoomed part (scan size is 1 × 1 μm^2). Grains are clearly visible, especially

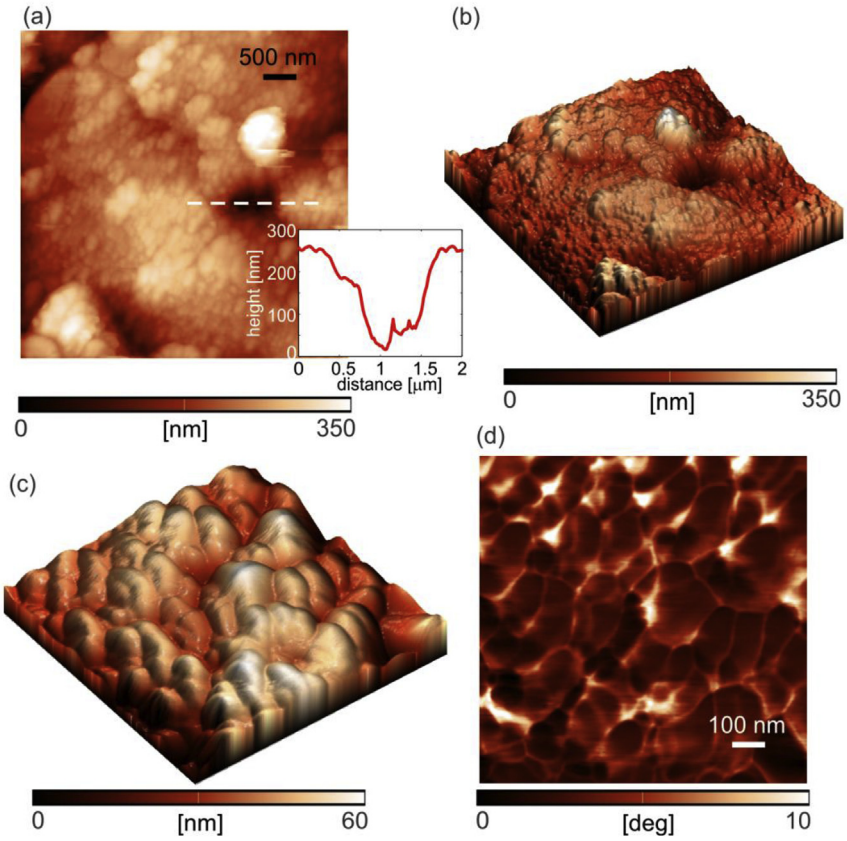

Fig. 1. (a) Two-dimensional and (b) three-dimensional topography of the sample surface. The inset in part (a) shows the cross-section along the corresponding dashed line. (c) Three-dimensional topography and (b) corresponding phase contrast image of a zoomed region from part (a).

grain boundaries in the phase contrast image since the phase is very sensitive to abrupt changes in the topography. Dispersion of grain size is rather wide, but still we can conclude that the characteristic grain size is in the order of 100 nm.

3.2. Far-infrared spectroscopy

The infrared reflectivity measurements were performed at room temperature with a BOMEM DA-8 Fourier-transform infrared spectrometer. A Hyper beamsplitter and deuterated triglycine sulfate (DTGS) pyroelectric detector were used to cover the wave number region from 80 to 650 cm^{-1}. Spectra were collected with 2 cm^{-1} resolution and with 500 interferometer scans added for each spectrum.

When visible light, λ, interacts with semiconducting nanoparticles (characteristic size d, dielectric function ε_2) which are distributed in a medium with the dielectric constant ε_1 in the limit $\lambda \gg d$, the heterogeneous composite can be treated as a homogeneous medium and effective medium theory is applied. There are many mixing models for the effective dielectric permittivity of such mixture [16]. Since our samples are well defined and separated nanosized grains, we used Maxwell-Garnet model for present case. For the spherical inclusions case, the prediction of the effective permittivity of mixture, ε_{eff}, according to the Maxwell-Garnet mixing rule is [17]:

$$\varepsilon_{eff} = \varepsilon_1 + 3f\varepsilon_1 \frac{\varepsilon_2 - \varepsilon_1}{\varepsilon_2 + 2\varepsilon_1 - f(\varepsilon_1 - \varepsilon_2)} \quad (1)$$

Here, spheres of permittivity ε_2 are located randomly in homogeneous environment ε_1 and occupy a volume fraction f. The observed nanoparticles are situated in air, therefore the ε_1 is 1. For dielectrical function of observing nanoparticles (ε_2) we used the standard model [18]:

$$\varepsilon_2(\omega) = \varepsilon_\infty \left(\prod_{k=1}^{n} \frac{\omega_{LOk}^2 - \omega^2 + i\gamma_{LOk}\omega}{\omega_{TOk}^2 - \omega^2 + i\gamma_{TOk}\omega} - \frac{\omega_P^2}{\omega(\omega - i\tau^{-1})} \right) \quad (2)$$

where ε_∞ is the bound charge contribution and it is assumed to be a constant, ω_{TOk} and ω_{LOk} are transverse and longitudinal frequencies, γ_{TOk}, and γ_{LOk} are their dampings, ω_P is the plasma frequency and τ is the free carrier relaxation time. The first term in (2) is the lattice contribution, whereas the second term is the Drude expression for the free carrier contribution to the dielectric constant. In this case, we will consider ω_{TOk} as a characteristic frequency of material (ν_k), and we will link ω_{LOk} with oscillator strength ($S_k \sim \omega_{LOk}^2 - \omega_{TOk}^2$) which does not have big influence on discussion.

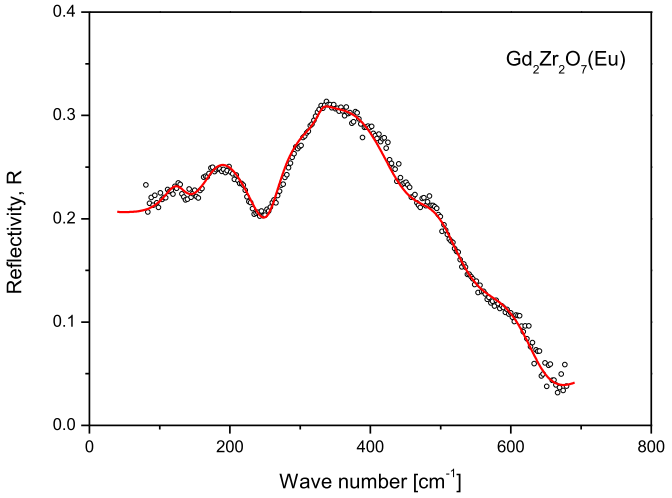

Fig. 2. Far – infrared reflection spectra of Eu^{3+} doped $Gd_2Zr_2O_7$ nanopowder. The experimental data are represented by circles. The solid lines are the calculated spectra obtained with the parameter values given in Table 1 and the fitting procedure based on the model given by Eqs. (1) and (2).

The far-infrared spectra of Eu^{3+} doped $Gd_2Zr_2O_7$ nanopowders, in the spectral range of 80–650 cm^{-1}, at room temperature, are presented in Fig. 2. The experimental data are presented by circles, while the solid lines are calculated spectra obtained by a fitting procedure based on the previously presented model. In Table 1 the best fit parameters are presented. Values for Eu^{3+} doped $Gd_2Zr_2O_7$ single crystal are taken from literature [11,19–22].

McCauley [23], and Vandenborre [24] came to the result that of the total number of 26 normal modes ($\Gamma = A_{1g} + E_g + 2F_{1g} + 4F_{2g} + 3A_{2u} + 3E_u + \mathbf{8F_{1u}} + 4F_{2u}$) only those of F_{1u} vibrations are active in the IR absorption. One of the eight F_{1u} modes is associated with three degrees of translation of the unit cell and refers to the acoustic branch of the crystal vibrations and thus analysis predict 7 IR – active optic modes [22]. Our results confirm all of the seven active vibrations and their assignations are shown in Table 1 and also indicate that anharmonicity factors are not significant. The analysis [23,24] also predicts that six vibrations of the types A_{1g}, E_g and $4F_{2g}$ are Raman – active modes. As per the selection rules, the remaining modes (F_{1g}, A_{2u}, E_u and F_{2u}) are inactive both in the IR and Raman spectra. According to the group-theoretical analysis, all the atoms of the crystal lattice are involved in the seven IR active F_{1u} vibrations (and six Raman – active modes) of the pyrochlore [22–24].

Following other authors' and our previous work [11,25] we started our analysis from the bulk material, considering that understanding bulk properties will lead to better understanding of properties of small particles, and therefore, as a result we expect the bulk modes to be shifted and broadened.

All modes are shifted compared to literature data. We believe that this is not because of the doping with Eu^{3+} and that in relatively small concentrations/amounts, doping did not induce changes in phonon spectra of $Gd_2Zr_2O_7$ [26]. We confirm our previous work [11] where we used Raman spectroscopy to obtain modes at 177 cm^{-1} and 268 cm^{-1} which noticeably differed from results obtained by many other authors who claimed that these modes occur at ~140 cm^{-1} (O-A-O vibrations) and ~220 cm^{-1} (O-B-O vibrations), respectively. Using FIR spectroscopy we obtained significant modes at 175 cm^{-1} and 255 cm^{-1} which describe O-A-O and O-B-O vibrations, respectively. The reason for this shift, as we believe, is electron – phonon interaction which led to the breakdown of the selection rules and appearance of the new phonons in fluorite structure $Gd_2Zr_2O_7$:Eu spectrum [11].

Interesting thing is, FIR spectrum shows two modes characteristic for pyrochlore type of structure, at 365 cm^{-1} and 490 cm^{-1}, although they are weak [19]. These two modes correspond to the vibrations of GdO_8 and ZrO_6 polyhedra, respectively. This confirm some earlier thoughts of P phase and F phase co-existing in the sample [19]. As it was said earlier [4,11], $Gd_2Zr_2O_7$ has two isometric structures, disordered fluorite (F) and ordered pyrochlore (P). In general, disordered fluorite structure type for this compound is confirmed [4]. But, it is also known that $Ln_2Zr_2O_7$ (Ln = elements of lanthanide series) have a pyrochlore-type structure stable at low temperature [19]. The Raman activity allowed for the pyrochlore structure results from oxygen vibrations, and only four bands are observed in the Raman spectra of $Ln_2Zr_2O_7$ pyrochlore-type compounds (Table 1 [21]). In the ordered structure there is no evidence of the significant band at 125 cm^{-1}, like our FIR spectrum shows.

Table 1
Best fit parameters of far – infrared spectra of Eu^{3+} doped $Gd_2Zr_2O_7$.

Exp. results: $Gd_2Zr_2O_7$: Eu^{3+} nanopowder	Literature: $Gd_2Zr_2O_7$: Eu^{3+} single crystal	Assignment
50	–	ν_7: O′-Gd-O′ bending vibrations
126	–	ν_6: Gd-ZrO_6 streching vibrations
175	177 [11]	ν_5: O-Gd-O bending vibrations
255	268 [11]	ν_4: O-Zr-O bending vibrations
330	310 [20], 315 [21]	ν_3: Zr-O + O-Zr-O vibrational mode (O-Zr-O bending)
365	370 [19], 400 [21]	ν_2: vibrations of GdO_8 polyhedra
490	500 [19], 538 [21]	ν_1: Zr-O stretching vibration, vibrations of ZrO_6 polyhedra
610	599 [20], 592 [21]	E_g: Zr-O′ stretching vibration

The thing is, for $Ln_2Zr_2O_7$ compounds, an order – disorder transition pyrochlore ↔ defective fluorite may occur when the temperature is raised [21]. This confirms that in $Gd_2Zr_2O_7$:Eu nanopowder P- and F- phase coexist. At first, this is not in agreement with XRD results for $Gd_2Zr_2O_7$:Eu nanopowder [4], but using FIR spectroscopy in reflectivity mode, we concern mainly the surface of material and coexistence of two phases is characteristic for the surface, but not for the general structure which is generally investigated using XRD.

Modes at 330 cm^{-1} and 610 cm^{-1} are clearly visible in both F phase and P phase spectra [20] and they correspond to Zr-O + O-Zr-O vibrational mode.

The rest of well known IR active vibrations, O-Gd-O and O′-Gd-O′ (O′ represents the 8(a) site oxide ion [27,28]) bending vibrations, are not yet assigned for Gd - zirconates. We assume that these vibrations correspond to 50 cm^{-1}, 126 cm^{-1} modes, respectively. The mode at 50 cm^{-1} clearly could not be obtained with our spectrometer which works in 80–650 cm^{-1} region, but that mode is well-suited to the fitting procedure based on the model given by Eqs. (1) and (2). Value of 50 cm^{-1} for Gd-zirconate is expected, regarding [[22], pg. 78, Table VII] which shows O′-Gd-O′ assignments for lanthanide series from La to Sm, but not for the Gd. We find answer in the isotope effect. The change in spectrum is conditioned with the mass of nuclei, and if the mass of some element is greater, spectral lines will move to lower values of wave number. Therefore, considering the increase in mass from La to Gd, we assume that previously unknown wave number value of O′-Gd-O′ vibration for Gd-zirconates corresponds to our result of 50 cm^{-1} (value of wave numbers from La to Gd are decreasing). We also use isotopic shift to explain the 126 cm^{-1} for which we assume corresponds to O-Gd-O vibration band and it also may suggest the possibility of a lowered local symmetry for some crystallographic sites [24] (that is in agreement with our assumptions with order ↔ disorder transition).

4. Conclusion

In this paper far-infrared reflectivity measurements were used to obtain phonon properties of Eu^{3+} doped $Gd_2Zr_2O_7$ nanopowders. We registered phonons of both isomeric structures characteristic for $Gd_2Zr_2O_7$ nanopowder and concluded coexistence of these two phases on the surface of the material, whereas fluorite structure is typical for the general structure. Low frequency modes were registered and regarding isotope effect they have been assigned.

Acknowledgments

This work was supported by Serbian Ministry of Education, Science and Technological Development under Project III45003.

References

[1] C. Fischer, S. Finkeldei, F. Brandt, D. Bosbach, A. Luttge, Direct measurement of surface dissolution rates in potential nuclear waste forms: the example of pyrochlore, ACS Appl. Mater. Interfaces 7 (32) (2015) 17857–17865.
[2] M.C. Hsieh, G.C. Wu, W.G. Liu, W.A. Goddard, C.M. Yang, Nanocomposites of tantalum-based pyrochlore and indium hydroxide showing high and stable photocatalytic activities for overall water splitting and carbon dioxide reduction, Angew. Chem. Int. Ed. 53 (51) (2014) 14216–14220.
[3] J. Parrondo, M. George, C. Capuano, K.E. Ayers, V. Ramani, Pyrochlore electrocatalysts for efficient alkaline water electrolysis, J. Mater. Chem. A 3 (20) (2015) 10819–10828.
[4] M.S. Rabasovic, D. Sevic, J. Krizan, M. Terzic, J. Mozina, B. Marinkovic, N.R.M. Mitric, M.D. Rabasovic, Characterization and luminescent properties of Eu^{3+} doped $Gd_2Zr_2O_7$ nanopowders, J. Alloys Compd. 622 (3) (2014) 292–295.
[5] R.J. Walker, et al., Surface termination and CO2 adsorption onto bismuth pyrochlore oxides, Chem. Mater. 28 (1) (2016) 90–96.
[6] T. Kondo, et al., Quadratic Fermi node in a 3D strongly correlated semimetal, Nat. Commun. 6 (2015) 10042.
[7] S.K. Gupta, P.S. Ghosh, C. Reghukumar, N. Pathak, R.M. Kadam, Experimental and theoretical approach to account for green luminescence from $Gd_2Zr_2O_7$ pyrochlore: exploring the site occupancy and origin of host-dopant energy transfer in $Gd_2Zr_2O_7$, RSC Adv. 6 (50) (2016) 44908–44920.
[8] J. Wu, et al., Thermal-barrier-coating applications, J. Am. Ceram. Soc. 35 (2002) 3031–3035.
[9] L. Wang, J.I. Eldridge, S.M. Guo, Thermal radiation properties of plasma-sprayed $Gd_2Zr_2O_7$ thermal barrier coatings, Scr. Mater. 69 (9) (2013) 674–677.
[10] K.-J. Hu, Z.-G. Liu, J.-Y. Wang, T. Wang, J.-H. Ouyang, Synthesis and photoluminescence properties of Eu^{3+}- doped $Gd_2Zr_2O_7$, Mater. Lett. 89 (2012) 276–278.
[11] G. Križan, M. Gilić, J.L. Ristić - Đurović, J. Trajić, M. Romčević, J. Križan, B. Hadžić, B. Vasić, N. Romčević, Raman Spectroscopy and electron - phonon coupling in Eu^{3+} doped $Gd_2Zr_2O_7$ nanopowders, Opt. Mater. (2017) (In press).
[12] Y.S. Chang, H.J. Lin, Y.L. Chai, Y.C. Li, Preparation and luminescent properties of europium-activated $YInGe_2O_7$ phosphors, J. Alloys Compd. 460 (1–2) (2008) 421–425.
[13] W. Zheng, P. Huang, D. Tu, E. Ma, H. Zhu, X. Chen, Lanthanide-doped upconversion nano-bioprobes: electronic structures, optical properties, and biodetection, Chem. Soc. Rev. (6) (2015) 1379–1415.
[14] K.S. Lee, K.I. Jung, Y.S. Heo, T.W. Kim, Y.G. Jung, U. Paik, Thermal and mechanical properties of sintered bodies and EB-PVD layers of Y_2O_3 added $Gd_2Zr_2O_7$ ceramics for thermal barrier coatings, J. Alloys Compd. 507 (2) (2010) 448–455.
[15] X.L. Xia, Z.G. Liu, J.H. Ouyang, S. Gao, X.M. Liu, Effect of Ce substitution for Zr on electrical property of fluorite-type $Gd_2Zr_2O_7$, Solid State Sci. 13 (6) (2011) 1328–1333.
[16] J. Trajić, M.S. Rabasović, S. Savić-Šević, D. Šević, B. Babić, M. Romčević, J.L. Ristić-Djurović, N. Paunović, J. Križan, N. Romčević, Far-infrared spectra of dysprosium doped yttrium aluminium garnet nanopowder, Infrared Phys. Technol. 77 (2016) 226–229.
[17] J.C.M. Garnett, Colours in metal glasses and in metallic films i (1904).
[18] I.J. Uhanov, Opt. Svojstva Poluprovodnikov, Nauka, Moskva, 1977.
[19] L. Zhou, et al., Thermal-driven fluorite–pyrochlore–fluorite phase transitions of $Gd_2Zr_2O_7$ ceramics probed in large range of sintering temperature, Metall. Mater. Trans. A Phys. Metall. Mater. Sci. (2015) 1–8.
[20] T. Moriga, S. Emura, A. Yoshiasa, S. Kikkawa, F. Kanamaru, X-ray and Raman study on coordination states of fluorite- and pyrochlore- type compounds in the system ZrO_2-Gd_2O_3 50 (1990) 357–361.
[21] D. Michel, M.P.Y. Jorba, R. Collongues, Study by Raman spectroscopy of order-disorder phenomena occurring in some binary oxides with fluorite-related structures, J. Raman Spectrosc. 5 (2) (1976) 163–180.
[22] M.A. Subramanian, G. Aravamudan, G.V. Subba Rao, Oxide pyrochlores - a review, Prog. Solid State Chem. 15 (2) (1983) 55–143.
[23] R.A. McCauley, Infrared-absorption characteristics of the pyrochlore structure, J. Opt. Soc. Am. 63 (6) (1973) 721.
[24] R.A. McCauley, Infrared-absorption characteristics of the pyrochlore structure, J. Opt. Soc. Am. 63 (6) (1973) 721.
[25] C.S.S.R. Kumar, Raman Spectroscopy for Nanomaterials Characterization, Springer-Verlag, Berlin Heidelberg, 2012.
[26] X.L. Xia, J.H. Ouyang, Z.G. Liu, Electrical properties of gadolinium-europium zirconate ceramics, J. Am. Ceram. Soc. 93 (4) (2010) 1074–1080.
[27] M.T. Vandenborre, E. Husson, J.P. Chatry, D. Michel, Rare-earth titanates and stannates of pyrochlore structure; vibrational spectra and force fields, J. Raman Spectrosc. 14 (2) (1983) 63–71.
[28] M.T. Vandenborre, E. Husson, Comparison of the force field in various pyrochlore families II. Phases presenting structural defects, J. Solid State Chem. 5359 (1984) 253–262.

Received: 30 October 2018 | Revised: 1 February 2019 | Accepted: 2 February 2019

DOI: 10.1002/jrs.5584

RESEARCH ARTICLE

WILEY Journal of RAMAN SPECTROSCOPY

Isotope-like effect in YVO_4:Eu^{3+} nanopowders: Raman spectroscopy

Jelena Mitrić[1] | Uroš Ralević[1] | Miodrag Mitrić[2] | Jovana Ćirković[3] | Gregor Križan[4] | Maja Romčević[1] | Martina Gilić[1] | Nebojsa Romčević[1]

[1] Institute of Physics, University of Belgrade, Belgrade, Serbia

[2] Laboratory for Theoretical Physics and Condensed Matter Physics, Vinca Institute of Nuclear Sciences, University of Belgrade, Belgrade, Serbia

[3] Department for Material Science, Institute for Multidisciplinary Research, University of Belgrade, Belgrade, Serbia

[4] AMI d.o.o, Crystal growth, Ptuj, Slovenia

Correspondence
Jelena Mitrić, Institute of Physics, University of Belgrade, Belgrade, Serbia.
Email: jmitric@ipb.ac.rs

Funding information
Serbian Ministry of Education, Science and Technological Development, Grant/Award Number: Project 45003

Abstract

In this paper, we describe synthesis and characterization of YVO_4 and Eu^{3+}-doped YVO_4 nanopowders. Two methods of preparation were used—solution combustion synthesis (SCS) and classical ceramic method (CCM)—and compared. Morphology and structure of all samples were characterized with atomic-force microscopy (AFM), X-ray diffraction (XRD), and field-emission scanning electron microscopy (SEM). Raman spectroscopy was used to discuss the isotope-like effect. It is confirmed that doping with Eu ions results in a change of Raman spectra of doped samples—new modes arise, and intensity of existing ones change. Influence of different preparation methods on isotope-like effect is presented with detailed calculations of shifted modes.

KEYWORDS

isotope-like effect, nanopowders, phosphor

1 | INTRODUCTION

The revelation of new materials, processes, and phenomena in general within the nanoscale proposes wide opportunities for evolution and expansion of innovative nanosystems and nanostructures. Nanostructured materials attract great attention of researches because of their wide industrial and technological applications. When doped, these kind of materials could exhibit enhanced properties, and when doped with rare-earth (RE) ions specifically oxide nanostructures show improved optical properties when compared with their bulk structures.[1–3]

The yttrium orthovandate (YVO_4) belongs to the group of important metal vanadates, MVO_4(M = Bi, Y, Fe, Cr, In, etc), because of its wide range of applications, especially in photonics.[4] Doped YVO_4 is very popular because of its photocatalytic properties[5,6] and is a very common semiconducting material in photochemistry because of this feature, as well for its enhanced luminescence when doped with RE ions.[7,8] Excellent thermal stability, robustness, and other physicochemical properties of YVO_4 ensured this nanostructure to be a very used material in optical devices.[9] Very convenient thing about YVO_4 is that it is an attractive host material (eg, for RE ions) that could be well excited under UV light irradiation; ie, the vanadate group, V^{5+} – O^{2-}, in YVO_4:Eu^{3+} is excited, and in that way, phonon energy is transferred to the doped RE ions. Eu ions exhibit red and orange emission, which corresponds to $^5D_0$–$^7F_2$ and $^5D_0$–$^7F_1$ transitions, respectively.[10] There are lot of

examples where nanostructures were doped with Eu ions because of its great luminescent characteristics.[11] RE ions are well known for their luminescence characteristics, which occur because of inner shell electronic transitions between the $4f^n$ energy levels. Yttrium ion in vanadate structure can be easily replaced with RE ions. Because of the similar properties of RE and yttrium ions, the concentration of RE ions can be larger in yttrium oxide than in other hosts. In our earlier work, we showed how doping with Eu ions could result in their replacement with R^{3+} ions in oxide nanopowders (R stands for a trivalent ion in oxide nanopowders, eg, Y^{3+} in YVO_4).[12] That results in more efficient optical properties of MVO_4 materials.[13] However, it has been shown that even a small amount of impurity could drastically enhance optical characteristics of these kinds of phosphors.[1] The inclusion of RE ions may be of a twofold nature: It could cause the shift of the gravity center of the energy levels, which is related to the nephelauxetic effect,[14] which is a measure of the metal-ligand covalency, and it could cause the splitting of the degenerate energy levels. The difference in size between bulk and nanocrystal cause different impact of the neighborhood on the metal ion, and in that way results in splitting of the energy levels, kinetics of the metastable levels, and metal-ligand covalency.[15]

There are many methods for nanopowder preparation,[16–20] and in this paper, we choose solution combustion synthesis (SCS), which is an important technique used for powder preparation, generally used to produce fine complex oxide ceramics. Even though SCS represents one of the simplest techniques, it offers numerous important advantages like homogeneity and high surface area of the samples, as well as high purity in combination with considerably lower temperatures and reduced processing time. Also, with this technique, fine particle size and crystalline samples can be obtained. Another method we used is classical ceramics method (CCM), which also offers significantly reduced time of powder preparation and controlled size of particles with respect only to temperature parameter. The goal was to represent two simple but yet effective methods of nanopowder preparation, which are cheap, fast, and reproducible and can be used for advanced applications. At the same time, they provide an insight in an interesting phenomenon, which we call isotope-like effect where with the use of Raman spectroscopy we observe substitution of Eu with Y ions. This occurrence in oxide nanopowders prepared by SCS and CCM is not explained in details by Raman spectroscopy in the literature yet, and to the best of our knowledge, this is the first report so far.

2 | SAMPLE PREPARATION AND CHARACTERIZATION METHODS

For sample preparation, two methods have been used. First, the solution combustion process is the most frequently used due to the low cost of the synthesis procedures and also due to the possibility of tailoring the size and morphology of particles. Eu^{3+}-doped YVO_4 nanopowders were prepared as described in previous research.[21,22] Eu^{3+} concentration was 1%, and it was obtained using stoichiometric quantities of starting chemicals Y $(NO_3)_3{\cdot}6H_2O$, NH_4VO_3, NH_4NO_3, and Eu $(NO_3)_3{\cdot}6H_2O$ with the purity of 99.99%. Starting chemicals were purchased from ABCR and urea, $(NH_2)_2CO$, from Sigma-Aldrich. The dry mixture of 0.357 g Eu $(NO_3)_3$ $\cdot 6H_2O$, 4.676 g of NH_3VO_3, and 15.32 g of Y $(NO_3)_3$ $6H_2O$ was combined with the mixture of 4.8 g of NH_4NO_3 and 3.003 g of $(NH_2)_2CO$, which were used as organic fuels. When all mixtures were prepared, they were combusted with the flame burner at ~500°C. After the synthesis, the nanopowders were annealed in air atmosphere at 1200°C for 2 hr. The annealing of material is needed in order to achieve the full crystallinity. That sample is labeled with YVO_4:Eu^{3+} (I).

Second sample, YVO_4:Eu^{3+} (II), and the undoped YVO_4 were prepared using simple classic ceramic procedure. Stoichiometric quantities of starting chemicals of Y_2O_5, Y_2O_3, and Eu_2O_3 were used with the purity of 99.99% purchased from ABCR, then powdered and baked on 900°C for 5 hr. Concentration of Eu^{3+} was 1%. In the case of undoped sample, no Eu^{3+} was added, but the rest of the procedure was the same as in preparation of doped sample.

In this way, we got morphologically different samples, and we can also make a comparison regarding two different (but at the same time, simple) preparation methods.

First characterization technique used for examining the topography of obtained samples was atomic force microscopy (AFM). Sample surfaces were investigated using NTMDT's NTEGRA PRIMA atomic force microscope, which operates in semicontact mode. The AFM topography and phase images were acquired simultaneously using NSG01 probes with a typical resonant frequency of 150 kHz and 10 nm curvature radius of the tip apex.

Further structural characteristics were obtained using the X-ray diffraction (XRD) powder technique. All samples were examined under the same conditions, using a Philips PW 1050 diffractometer equipped with a PW 1730 generator, 40 kV × 20 mA, using Ni filtered Co Kα radiation of 0.1778897 nm at room temperature. Measurements were carried out in the 2 h range of 10–100° with a

scanning step of 0.05° and 10-s scanning time per step. Crystallite size was determined by using XFIT computing program which is based on fundamental parameter convolution approach.[23]

Field-emission scanning electron microscopy with energy dispersive X-ray spectrometer, FESEM-EDS, (FEI Scios 2) was used for morphology studies of our samples. The acceleration voltage between cathode and anode was equal to 15 kV. High-resolution SEM images and EDS spectra from the chosen microareas and high-resolution maps were shown elemental composition and surface distribution.

Raman measurements were performed using commercial NTegra Spectra system from NT-MDT with a laser operating at a wavelength of 532 nm. Laser power was set to 2 mW within the ~0.5 × 0.5 μm sized focus with exposure time of 600 s. All the Raman spectra are unpolarized.

3 | RESULTS AND DISCUSSION

3.1 | Atomic force spectroscopy

The results of AFM measurements are shown in Figure 1. The samples of YVO_4 and YVO_4:Eu^{3+} (II) have granular surfaces whereas the surface of YVO^4:Eu^{3+} (I) has flat domains separated by deep holes with depths up to several hundred nanometers. The lateral size of the flat domains has an average value of 3–4 μm. The grain and domain boundaries are also visible in the corresponding phase images, whose large phase contrast originates mainly from the abrupt changes in the topography at these boundaries. The average grain size cannot be estimated accurately as the AFM tip is not able to penetrate deep enough between the tightly packed grains. Finally, the root-mean-square roughness (RMS) parameter assessed for the YVO_4 and YVO_4:Eu^{3+}(II) surfaces has

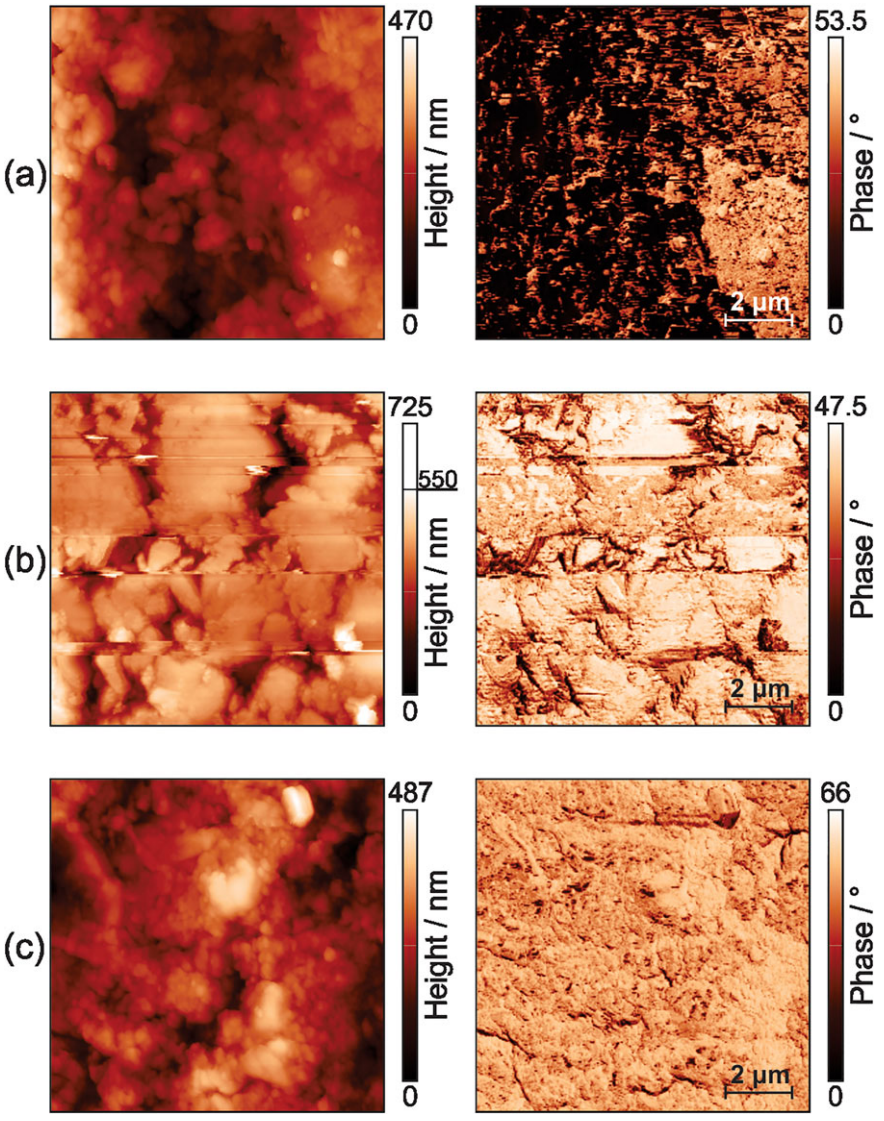

FIGURE 1 AFM topography and corresponding phase images for (a) YVO4, (b) YVO4:Eu3 + (I) and (c) YVO4: Eu3 + (II). [Colour figure can be viewed at wileyonlinelibrary.com]

values of about 67.2 and 67.8 nm, respectively, whereas the morphologically distinctive YVO4:Eu^{3+}(I) surface has smaller RMS of around 64.5 nm.

3.2 | XRD analysis

Structure of synthesized samples of YVO_4 and YVO_4:Eu^{3+} nanopowders were identified by XRD patterns as shown in Figure S1. All the observed peaks are in good agreement with the JCPDS card 17-0341. The samples are monophased and they crystallize in body-centered tetragonal lattice in the zircon-type structure (Figure 2). No additional peaks other than ones of YVO_4, confirm that doping of Eu^{3+} does not change the crystalline structure. Calculated crystallite size for YVO_4, YVO_4:Eu^{3+}(I), and YVO_4:Eu^{3+} (II) are 52, 58, and 53 nm, respectively. It was expected that YVO_4 and YVO_4:Eu^{3+} (II) have similar crystallite size because of the same method of preparation. It was also showed that using classical ceramic method we get smaller crystallite size of nanopowders when compared with solution combustion method.

3.3 | FESEM analysis

The surface morphology and size of the prepared samples were inspected using field emission scanning electron microscopy (FESEM) equipped with an energy-dispersive X-ray spectrometer (EDX). Results are shown in Figure S2. All samples have spherical nanoparticles; size of particles are around 2 μm for the samples prepared with classical ceramic method (YVO_4 and YVO_4:Eu^{3+} (II)) and 3 μm for the sample prepared with solution combustion synthesis (YVO_4:Eu^{3+} (I)). The particles sizes obtained directly from FESEM images are much bigger than those calculated by XRD patterns, revealing the particle aggregation. However, even after aggregation, particle size is rather similar. It could be said that YVO_4:Eu^{3+} (II) crystallized in more fluffier structure, whereas YVO_4:Eu^{3+} (I) is more crystalline, but that does not have any impact on aggregation.

EDX spectra confirm that our samples consist only of Y, V, and O for the undopped and Y, V, O and Eu ions for the dopped samples.

3.4 | Raman spectroscopy

Primitive cell of YVO_4 consists of 12 atoms (Figure 2), which support 36 modes of vibration of which 12 of them are Raman active can be divided into external and internal modes. External modes originate from translations of the $(VO_4)^{3-}$ and R^{3+} ions and librational mode of the whole $(VO_4)^{3-}$ tetrahedra, whereas internal modes occur due to vibrational oxygen modes within the tetrahedral groups $(VO_4)^{3-}$.[24] Seven of twelve Raman active modes are labeled as internal – $2A_{1g}$, $2B_{1g}$, $1B_{2g}$, $2E_g$, and four are known as external – $2B_{1g}$, $2E_g$.

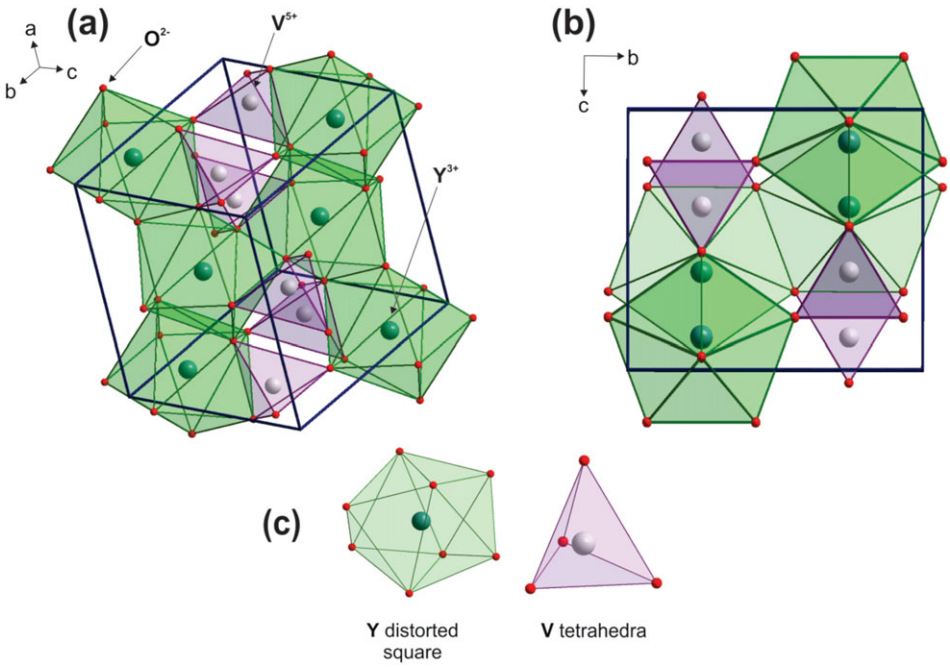

FIGURE 2 Structure of YVO4. (a) Pictorial representation of 3D structure of YVO4. (b) The same structure along one direction. (c) Polyhedral surroundings of Y and V ions are shown.Y3+ has distorted square surrounding eight O2− ions around one Y3+, and V5+ has tetrahedral surrounding four O2− ions around one V5+ ion. [Colour figure can be viewed at wileyonlinelibrary.com]

Figure 3 presents unpolarized Raman spectra obtained for three samples. Assignations of all the modes registered are given in Table 1.

The most of the Raman active modes registered come from YVO_4 structure, external, and internal vibrations, and just couple of them arise or are amplified by doping with Eu^{3+} (see Table 1). In Eu^{3+} doped YVO_4 structure, Eu^{3+} can be regarded as a substitution impurity ion, where Y gets substituted for Eu. The impurity mode could arise due to complex mechanism of electron–phonon interaction[25] or simply because of the difference between masses of the doping ions and ions of the host material (known as isotope effect).[26] In our case, there is no electron–phonon interaction, we have impurity modes that arise due to the difference between mass of ions exchanged. Even though we do not have actual isotopes, we observe a substitution of one ion with a heavier one, with approximation that force constant remains unchanged. Therefore, we call it isotope-like effect.

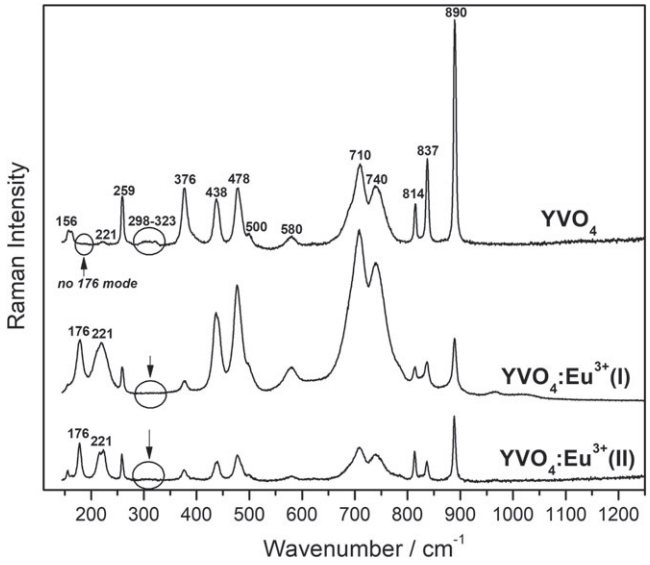

FIGURE 3 Raman spectroscopy of three samples of YVO4 and YVO4:Eu3+ (I) and (II)

First, let us define well known equation, which connects force constant and oscillator frequency:

$$k = 4\pi^2 m\omega_{osc}^2, \tag{1}$$

where k is force constant, m is mass of molecule, and ω_{osc} is an oscillator frequency.

From Equation 1, it is clear that oscillator frequency is proportional to force constant and inversely proportional to the mass. That means that (if we assume that force constant is not changing when impurity is added) change of vibrational (oscillator) frequency depends only on mass of observed molecule.

If we observe molecules with masses m_i ($i = 1, 2, \ldots n$), their corresponding vibrational frequencies, ω_{osc} are given with Equation 2.

$$\omega_{osc}^{i} = \frac{1}{2\pi}\sqrt{\frac{k}{m_i}}. \tag{2}$$

If we observe two molecules, their ratio is given with ρ:

$$\frac{\omega_{osc}^2}{\omega_{osc}^1} = \sqrt{\frac{\mu_1}{\mu_2}} = \rho. \tag{3}$$

If $m_2 > m_1$, then $\omega_{osc}^2 < \omega_{osc}^1$.

TABLE 1 Assignation of YVO_4:Eu^{3+} vibrational modes registered by Raman spectroscopy

Vibrational Mode (cm^{-1})	Assignation
156	$\mathbf{B_{1g}}$; *external vibration*; vibrational modes of oxygen atoms within $(VO_4)^{3-}$ tetrahedral group[21]
176	vibration caused by doping with Eu^{3+}
221	amplified vibration by doping with Eu^{3+}
259	$\mathbf{B_{2g}}$; *external mode*; symmetrical stretching vibration mode[4] in $(VO_4)^{3-}$
376	$\mathbf{A_{1g}}$; *internal mode*; symmetrical deformation vibration[4] in $(VO_4)^{3-}$
438	*internal mode*; *amplified in* YVO_4:Eu^{3+} (I) and weakened in YVO_4:Eu^{3+} (II).
478	$\mathbf{B_{1g}}$; *internal mode*; antisymmetric stretching vibration mode[4] in $(VO_4)^{3-}$
500	$\mathbf{B_{1g}}$; *internal mode*;
580 710 740	*internal modes*; Amplified or weakened vibrations by doping, depending on the method of fabrication. In the YVO_4:Eu^{3+} (I) these vibrations are amplified, whereas in the YVO_4:Eu^{3+} (II) they are weakened.
814	$\mathbf{B_{1g}}$; *internal mode*;
837	$\mathbf{E_g}$; *internal mode*; antisymmetric stretching deformation vibration mode in $(VO_4)^{3-}$
890	$\mathbf{A_{1g}}$; *internal mode*;

In that way, we get the frequency of shifted mode, which appeared when substitution of heavier ion is made.

Mode at 176 cm^{-1} arises when YVO_4 is doped with Eu^{3+}. We explain this with isotope-like effect. Eu ion substitutes Y ion, and as a result mode at 176 cm^{-1} is obtained. Calculation was made using Eq. (1-3). They confirm that mode at 221 cm^{-1} shifted to 176 cm^{-1} within the error limits, but also is significantly amplified. This is due to interaction of modes at 221 and 176 cm^{-1}, also provoked by doping with Eu^{3+}. Also, we have a wide mode in the range 298–323 cm^{-1} in the sample that is not doped with Eu^{3+}, but it vanishes when doped.

The intensities of modes obtained should also be discussed. Same type symmetry modes, A_{1g}, at 890 cm^{-1} and 376 cm^{-1} are both reduced when YVO_4 nanopowder is doped with Eu ions. Same thing happens with modes at 156, 259, and 814 cm^{-1}, which are in B_{1g} and B_{2g} symmetry. E_g mode at 814 cm^{-1} also shows significant reducing in intensity after doping (see Table 1). A_{1g} modes are internal and they represent symmetrical deformation vibrations in $(VO_4)^{3-}$, whereas B_{1g} and B_{2g} are antisymmetric and symmetric stretching vibrations in $(VO_4)^{3-}$; E_g represent antisymmetric stretching deformation vibration mode in $(VO_4)^{3-}$. Irreducible representations noted with A and B are one dimensional, whereas E_g is two dimensional. The modes at 438, 580, 710, and 740 cm^{-1} could not be found in the earlier literature. We think those are internal modes which also arise due to $(VO_4)^{3-}$ vibrations but are amplified or weakened according to method of fabrication. These modes are amplified when nanopowders are prepared by solution combustion method. As we said earlier, this method results in smaller particles and less grained structure. As a result modes are somewhat wider and more intense when compared with samples prepared by CCM, which have more grained structure. This by no means influence on isotope-like effect in these structures.

4 | CONCLUSION

In this paper, we showed how doping of Eu ions affect on YVO_4 nanopowders. We conclude that Eu ions substitute Y ions in YVO_4 structure and new modes in Raman spectra occur. Detailed calculation of isotope-like effect was presented. Same symmetry modes show the same tendency of reducing intensity which we attribute to the doping with Eu ions, because of the symmetry disturbance of $(VO_4)^{3-}$ tetrahedra. No effect of method preparation of doped samples on isotope-like effect are observed, which means that the size of crystallites nor morphology of samples affect on substitution of doped ions into YVO_4 nanostructures. It was noticed that particles agglomerate, but that does not have an impact on isotope-like effect. To our knowledge, there is no similar and more detailed study in the literature concerning this effect, therefore this work is one of the firsts to discuss it.

ACKNOWLEDGMENTS

This research was financially supported by the Serbian Ministry of Education and Science (Project 45003).

ORCID

Jelena Mitrić https://orcid.org/0000-0002-1526-3976
Maja Romčević https://orcid.org/0000-0002-5064-175X

REFERENCES

[1] S. Thakur, A. K. Gathania, *J. Electronic Mater.* **2015**, *44*, 3444.
[2] S. M. Rafiaei, A. Kim, M. Shokouhimehr, *Curr. Nanosci.* **2016**, *12*(2), 244.
[3] S. Rafiaei, T. Isfahani, H. Afshari, M. Shokouhimehr, *Mater. Chem. Phys.* **2018**, *203*, 274.
[4] M. S. Rabasović, J. Križan, P. Gregorčič, M. D. Rabasović, N. Romčević, D. Šević, *Opt. Quant. Electron.* **2016**, *48*, 163.
[5] R. M. Mohamed, F. A. Harraz, I. A. Mkhalid, *J. Alloy. Compd.* **2012**, *532*, 55.
[6] H. Xu, H. Wang, H. Yan, *J. Hazard. Mater.* **2007**, *144*, 82.
[7] M. Shokouhimehr, S. M. Rafiaei, *Ceram. Int.* **2017**, *43*, 11469.
[8] S. M. Rafiaei, A. Kim, M. Shokouhimehr, *Nanosci. Nanotechn. Lett.* **2014**, *6*(8), 692.
[9] X. Xiao, G. Lu, S. Shen, D. Mao, Y. Guo, Y. Wang, *Mater. Sci. Eng. B* **2011**, *176*, 72.
[10] D. Šević, M. S. Rabasović, J. Križan, S. Savić-Šević, M. Mitrić, M. Gilić, B. Hadžić, N. Romčević, *Mater. Res. Bull.* **2017**, *88*, 121.
[11] S. Ram, *J. Raman Spectrosc.* **1987**, *18*, 537.
[12] J. Mitrić, J. Križan, J. Trajić, G. Križan, M. Romčević, N. Paunović, B. Vasić, N. Romčević, *Opt. Mater.* **2018**, *75*, 662.
[13] Y. Zhou, Q. Ma, M. Lü, Z. Qui, A. Zhang, *J. Phys. Chem. C* **2008**, *112*, 19901.
[14] C. K. Jorgensen, *Modern Aspects of Ligand Field Theory*, North-Holland, Amsterdam **1971**.
[15] S. Georgescu, E. Cotoi, A. M. Voiculescu, O. Toma, C. Matei, *Rom. J. Phys.* **2010**, *55*, 750.
[16] Z. De-Quing, W. Shao-Jun, S. Hong-Shan, W. Xiu-Li, C. Mao-Sheg, *J. Sol-Gel Sci. Techn.* **2007**, *41*, 157.
[17] W. Feng, L. Mu-Sen, L. Yu-peng, Q. Yong-xin, *Mater. Lett.* **2005**, *59*, 916.
[18] S. Hua Xiao, W. Fen Jiang, L. Y. Li, X. Jian Li, *Mater. Chem. Phys.* **2007**, *16*, 82.
[19] C. Xu, L. Ma, X. Liu, W. Qui, Z. Su, *Mater. Res. Bull.* **2004**, *39*, 881.
[20] K. Zhang, X. Sun, G. Lou, X. Liu, H. Li, Z. Su, *Mater. Lett.* **2005**, *59*, 2729.

[21] M. S. Rabasović, D. Šević, J. Križan, M. Terzić, J. Mozina, B. P. Marinković, S. Savić –Šević, M. Mitrić, M. D. Rabasović, N. Romčević, *J. Alloy. Compd.* **2015**, *622*, 292.

[22] J. Križan, M. Mazaj, V. Kančič, J. Bajsić, J. Mozina, *Acta Chim. Slov.* **2014**, *61*, 608.

[23] R. W. Cheary, A. Coelho, *J. Appl. Cryst.* **1992**, *25*, 109.

[24] A. Sanson, M. Giarola, B. Rossi, G. Mariotto, E. Cazzanelli, A. Speghini, *Phys. Rev. B* **2012**, *86*, 214305.

[25] A. A. Gogolin, E. I. Rashba, *Solid State Commun.* **1976**, *19*, 1177.

[26] N. Romčević, J. Trajić, T. A. Kuznetsova, M. Romčević, B. Hadžić, D. R. Khokhlov, *J. Alloy. Compd.* **2007**, *442*, 324.

SUPPORTING INFORMATION

Additional supporting information may be found online in the Supporting Information section at the end of the article.

How to cite this article: Mitrić J, Ralević U, Mitrić M, et al. Isotope-like effect in $YVO_4:Eu^{3+}$ nanopowders: Raman spectroscopy. *J Raman Spectrosc*. 2019;1–7. https://doi.org/10.1002/jrs.5584

Physica E: Low-dimensional Systems and Nanostructures 104 (2018) 64–70

Contents lists available at ScienceDirect

Physica E: Low-dimensional Systems and Nanostructures

journal homepage: www.elsevier.com/locate/physe

Surface optical phonon – Plasmon interaction in nanodimensional CdTe thin films

J. Mitric[a,*], N. Paunovic[a], M. Mitric[b], B. Vasic[a], U. Ralevic[a], J. Trajic[a], M. Romcevic[a], W.D. Dobrowolski[c], I.S. Yahia[d,e], N. Romcevic[a]

[a] Institute of Physics, University of Belgrade, Pregrevica 118, 11080 Belgrade, Serbia
[b] Institute Vinca, University of Belgrade, P.O. Box 522, 11001 Belgrade, Serbia
[c] Institute of Physics, Polish Academy of Science, al. Lotnikov 32/46, 02-668 Warsaw, Poland
[d] Department of Physics, Faculty of Science, King Khalid University, P.O. Box 9004, Abha, Saudi Arabia
[e] Nano-Science & Semiconductor Labs, Department of Physics, Faculty of Education, Ain Shams University, Roxy, Cairo, Egypt

ARTICLE INFO

Keywords:
Thin film
Surface optical phonon
Raman spectroscopy
Far–infrared spectroscopy
Plasmon-phonon interaction

ABSTRACT

Structural and optical properties of CdTe thin films were investigated applying atomic force microscopy (AFM), XRD powder technique, Raman spectroscopy and far–infrared spectroscopy. CdTe thin films were prepared by using thermal evaporation technique. In the analysis of the far – infrared reflection spectra, numerical model for calculating the reflectivity coefficient for system which includes films and substrate has been applied. Effective permittivity of film mixture (CdTe and air) was modeled by Maxwell – Garnet approximation. We reveal the existence of surface optical phonon (SOP) mode and coupled plasmon-SOP modes (CPSOPM).

1. Introduction

II – VI semiconductor compounds, especially thin films, have become very popular because of their applications in numerous electronic and optoelectronic devices. Due to low production cost, thin films nowadays enjoy great attention in basic research and solid state technology.

The interest in various properties of photonic CdTe is well justified, as this material plays an important role in expanding variety of applications as in: integrated optics, optoelectronics, or solar energy conversion [1].

Two main properties of CdTe thin film are its high optical absorption coefficient (a thin film of CdTe with thickness of approximately 2 μm will absorb nearly 100% of the incident solar radiation) and its near ideal band gap for photovoltaic conversion efficiency of 1.45eV [2]. Also, its ease of film fabrication and low cost make it a representative material among II – VI semiconductors.

For fabrication of the CdTe films, various techniques have been applied: RF magnetron sputtering [3], molecular beam epitaxy (MBE) [4], pulsed laser deposition (PLD) [5], successive ionic layer adsorption and reaction method (SILAR) [6], metal organic chemical vapor deposition [7], screen printing [8], thermal evaporation method [9] etc. Thermal evaporation method shows some advantages such as: minimalization of impurities proportional to the growing layer, reduced chances of oxidation and direction of propagation (occurs from the source to the substrate) [9,10]. This makes thermal evaporation technique the most suitable method, thanks to very high deposition rate, low material consumption and low cost of fabrication [11].

In the case of crystal with relatively small dimension, in the frequency range between bulk longitudinal optical phonon frequency (ω_{LO}) and transversal optical phonon frequency (ω_{TO}), a new mode known as a surface phonon mode appears [12,13]. It is known for the case of real crystal, that when its dimension is relatively small, surface modes and effects of dimension will be manifested in addition to the normal modes of infinite lattice. But, when crystal is reduced to extremely small dimensions, only the surface mode will persevere [12–14].

On the other side, electron – phonon interaction takes an important place in semiconducting materials [15]. In our earlier work we have registered plasmon (collective electron excitation) and LO phonons interaction in different systems [16–19]. Besides that, we have studied the impact of damping on interaction appearance [20], interaction between plasmon and different phonons [21,22], as well as interaction between plasmon and impurity local phonons [23–25].

In this work we report experimental studies of CdTe thin films prepared by thermal evaporation technique. Existence of nanodimensional structures in these thin films enabled us to observe effects associated with interactions between surface optical phonon (SOP) and

* Corresponding author.
E-mail address: jmitric@ipb.ac.rs (J. Mitric).

https://doi.org/10.1016/j.physe.2018.07.021
Received 27 April 2018; Received in revised form 5 July 2018; Accepted 16 July 2018
Available online 18 July 2018
1386-9477/

plasmon for the first time.

Samples characterization was performed using atomic force microscopy (AFM). Structural properties were analyzed using XRD powder technique, and optical properties were characterized using Raman and far–infrared spectroscopy.

2. Sample preparation and characterization methods

CdTe single crystal was grown by the Bridgman technique. Different thickness of CdTe thin films were deposited by thermal evaporation from a resistance heating quartz glass crucible onto glass substrates using high vacuum coating unit type Edward 306 A. Films were grown at a pressure of 106 Pa. The mechanical rotation of the substrate holder during deposition produced homogeneous film. The distance between the source heater and substrates holder is 21 cm, in order to avoid any heat flow from the source to the substrates.

The morphology of the four CdTe thin films of different thicknesses was investigated by Atomic force microscopy (AFM). Atomic force microscopy measurements were performed using NT-MDT system NTEGRA Prima. Imaging was done in tapping mode using NSG01 probes. All AFM measurements were done at ambient conditions. For the sake of statistical analysis of sample surface, we calculated histograms and bearing ratios for each topographic image. The histogram represents a height distribution density of all points in a two-dimensional topographic image, or in other words, it is a number of points with height given on x-axis. On the other hand, the bearing ratio curve gives a percent of points in a corresponding two-dimensional topographic image with a height less than the number given on x-axis.

The structural characteristics were obtained by the XRD powder technique. All samples were examined under the same conditions, using a Philips PW 1050 diffractometer equipped with a PW 1730 generator, 40 kV × 20 mA, using Ni filtered Co Kα radiation of 0.1778897 nm at room temperature. Measurements were carried out in the 2 h range of 10–100° with a scanning step of 0.05° and 10 s scanning time per step. Crystallite size was determined by using XFIT computing program which is based on Fundamental Parameter convolution approach [26].

Raman measurements were performed using commercial NTegra Spectra system from NT-MDT. A linearly polarized semiconductor laser operating at a wavelength of 532 nm was used. All the spectra were obtained by setting the laser power to 2 mW within the ~0.5 × 0.5 μm sized focus with exposure time of 600 s.

The far-infrared (FIR) reflectivity measurements were performed at room temperature with a BOMEM DA-8 Fourier-transform infrared spectrometer. A Hyper beamsplitter and deuterated triglycine sulfate (DTGS) pyroelectric detector were used to cover the wave number region from 80 to 650 cm^{-1}.

3. Results and discussion

3.1. Atomic force microscopy

Three dimensional topographic images of all four samples are shown in the left side of Fig. 1. As can be seen, sample surfaces are rather flat, but still they are characterized with bright protrusions and dark holes (which represent air) resulting in a small surface roughness of several nanometers.

In order to characterize fraction of both observed topographic features, the statistical analysis have been performed by calculating histograms and bearing ratios from two dimensional topographic images. The results for all four samples are given in the right side of Fig. 1. They show that the peaks in the histograms are positioned in the middle of bearing ratio curves. Therefore, from these curves we can conclude that the fraction of holes and protrusions are rather similar, around 50%.

In order to estimate thicknesses of studied films, their step edges were measured by AFM. 3D AFM topographic images of the step edges are depicted in Fig. 2(a1-d1). The films are brighter and the substrates are dark in the images, while the step edges are clearly resolved. Based on the AFM images, height distributions were calculated and presented in Fig. 2 (a2-d2). In all histograms, there are two characteristic peaks: a lower one corresponds to the substrate, while a higher one corresponds to the film. Therefore, the film height can be then approximately calculated as a difference between these two peaks. Estimated film thicknesses are given in Fig. 2 (a2-d2). The best resolved height peaks were found on CdTe 1 in Fig. 2 (a2) due to a smooth sample surface as can be seen in Fig. 2 (a1).

3.2. XRD

Structures of four synthesized CdTe thin films with different thicknesses were identified by XRD pattern as shown in Fig. 3. The diffractograms confirm that all samples are monophased, and that they crystallized in sphalerite type structure in 216. space group, $F\bar{4}3m$. All of the observed diffraction peaks are indexed according to this space group. Therefore, in our thin film samples there is no other structures other than CdTe. In this structural type, Cd ions occupy *4a* Wyckoff positions, [[0, 0, 0]] with local symmetry $\bar{4}3m$, while Te ions occupy *4c* Wyckoff positions [[1/4, 1/4, 1/4]] with the same local symmetry. Cd ions are in tetrahedral surrounding of Te ions (and vice versa). The tetrahedrons are regular and share common vertices. Crystallite size (R) is determined and presented in Fig. 2 and Table 1.

3.3. Raman spectroscopy

The cubic face-centered structure of balk crystal CdTe is characterized by the 216. space group $F\bar{4}3m$ and contains four formula units, while the primitive cell is one fourth as many. Optical modes consist of one three fold –degenerated mode F_2 which is active in IR and Raman spectra. The dipole mode F_2 is split into the transverse (TO) and longitudinal (LO) modes in the vibrational spectra. It is very well known that reduction of the particle dimensions to nanoscale results in a breakdown of phonon selection rules and allows phonons with $l \neq 0$ to contribute to Raman scattering [27–31]. Consequently, some new forbidden vibration modes (low frequency region, acoustic modes, and high frequency region, surface optical modes) occur due to imperfections, impurity, valence band mixing and/or nonspherical geometry of the nanostructures [14].

TO (142 cm^{-1}) and LO (170.5 cm^{-1}) modes for the CdTe bulk crystal are both active in the Raman spectra. Also, the modes in band near 120 cm^{-1} correspond to phonons of Te on the CdTe surface and can be seen in the Raman spectra [32].

Raman spectra of CdTe thin films of different thickness at room temperature are presented in Fig. 4.

For analyzing obtained spectra Lorentz profiles were used. Solid lines are their sums. In the top right corner Raman spectra of bulk CdTe crystal for ambient conditions is presented [32]. The observed Raman spectra for all samples among characteristic CdTe TO mode at 142 cm^{-1} and phonon of Te of the CdTe surface (127 cm^{-1}), show the LO phonon like frequency shift from 170.5 cm^{-1} to 164 cm^{-1}. That can be attributed to the surface optical phonon (SOP) mode effect [33–38]. It is clear that SOP phonon is wider compared to LO phonon of bulk crystal, as well as when it's compared to phonon of nanodimensional film. This effect is associated with interaction between SOP and plasmon, which will be mentioned later on.

In order to analyze the surface optical phonon we have to take into account that a part of crystallites are surrounded by air. We will analyze the dependence of the SOP mode position on filling factor (*f*) of the mixed material.

Surface phonon modes can be detected in systems where particle size is much smaller when compared to wavelength of exciting light source [39]. These modes can be obtained for in the case of polar crystals [40], so we consider expression for dielectric function which describes optical properties of polar semi – insulating semiconductor in

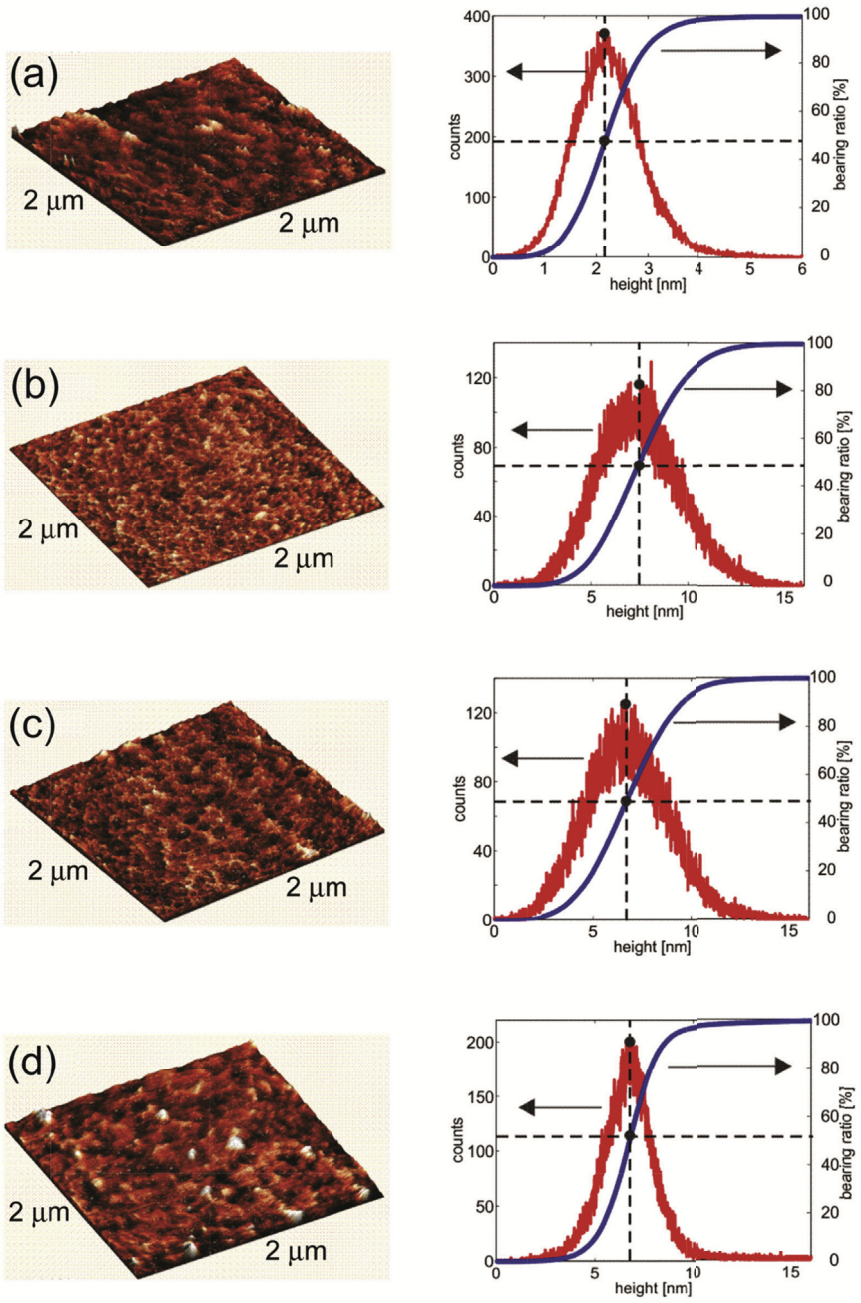

Fig. 1. Three-dimensional topographic image (left) and corresponding histogram and bearing ratio (right) for (a) CdTe 1, (b) CdTe 2, (c) CdTe 3, and (d) CdTe 4. Scan size is 2 μm.

IR region [24]:

$$\varepsilon_2(\omega) = \varepsilon_\infty\left(1 + \sum_{k=1}^{n} \frac{\omega_{LOk}^2 - \omega_{TOk}^2}{\omega_{TOk}^2 - \omega^2 - i\gamma_{TOk}\omega} - \frac{\omega_P^2}{\omega(\omega + i\Gamma)}\right) \quad (1)$$

ωTO and ωLO represent transverse and longitudinal optical bulk phonons, respectively; ε∞ is the dielectric constant at high frequencies, ωP is plasma frequency and γ and Γ are the damping constants. Surface phonons can be considered similarly to phonons in infinite crystals, but with adapted wave functions to the geometry of the small particle.

Here, we will apply effective medium theory: Because the size of semiconducting nanoparticles, L, (with dielectric function ε_2, and are distributed in a medium with dielectric constant ε_1) is considerably smaller than the interacting wavelength of visible light, λ (λ ≫ *L*), we treat the heterogeneous composite as a homogeneous medium.

Even though there are numerous models for the effective dielectric permittivity for these kinds of mixtures [41], we decided to use Maxwell – Garnet model, because all our samples are thin films with well defined and separated nanosized grains. According to the Maxwell – Garnet mixing rule [42,43], effective permittivity of mixture, including spherical geometry of particles is given with:

$$\varepsilon_{eff} = \varepsilon_1 + 3f\varepsilon_1\frac{\varepsilon_2 - \varepsilon_1}{\varepsilon_2 + 2\varepsilon_1 - f(\varepsilon_1 - \varepsilon_2)} \quad (2)$$

In this case, nanoparticles are spheres with permittivity ε_2 and are randomly distributed in homogeneous environment, with permittivity

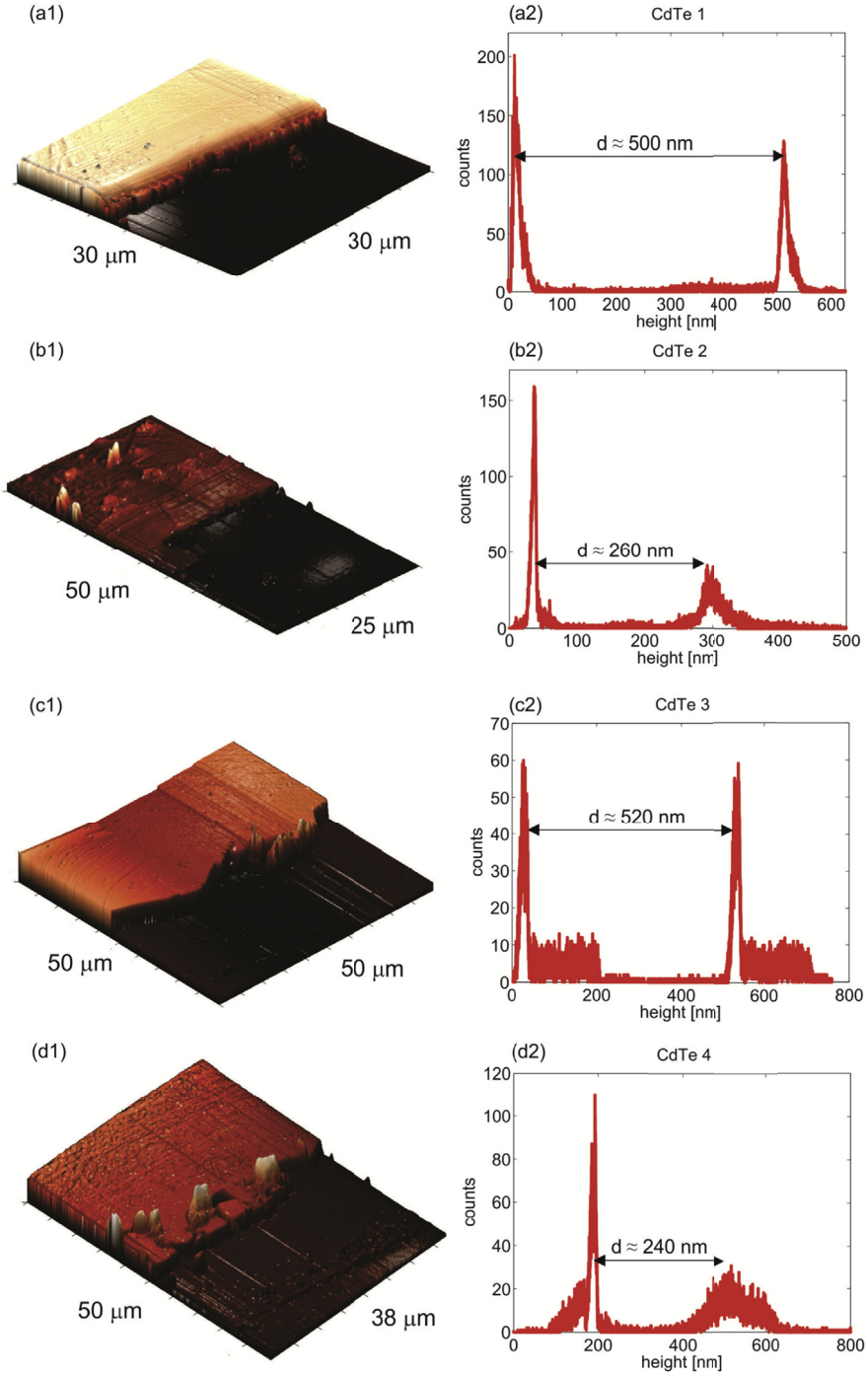

Fig. 2. (a1-d1) 3D AFM topographic images of step edges of studied films, and (a2-d2) corresponding height histograms. Average films thicknesses are denoted in the histograms.

ε_1 and occupy a volume fraction f.

Position surface optical phonon (SOP) mode frequencies are obtained from Ref. [44]:

$$\omega_{SOP} = max\left(I_m\left(-\frac{1}{\varepsilon_{eff}}\right)\right) \tag{3}$$

The result is shown in Fig. 5. The practical liner dependence of the position of the SOP mode on the filing factor f has been obtained. For the frequency of the SOP mode determined in Fig. 4 we have $f = 0.53$. This result is in accordance with the one obtained from the AFM measurements.

3.4. Far-infrared spectroscopy

Thicknesses of our films, as we will see, are in a range from ~0.39 μm to ~0.72 μm, so reflectivity spectra contain information about CdTe films together with information about substrate. Representative scheme of our layered structure can be presented in Fig. 6 [45]. Medium 1 is air, medium 2 is thin bulk CdTe crystal layer and medium 3 is substrate glass, with dielectric functions ε_1 ($\varepsilon_1 = 1$), ε_2 and ε_3, respectively. We can now write [46]:

$$R_A = \frac{A_r}{A_i} = \frac{r_{12}e^{-i\alpha} + r_{23}e^{i\alpha}}{e^{-i\alpha} + r_{12}r_{23}e^{i\alpha}} \tag{4}$$

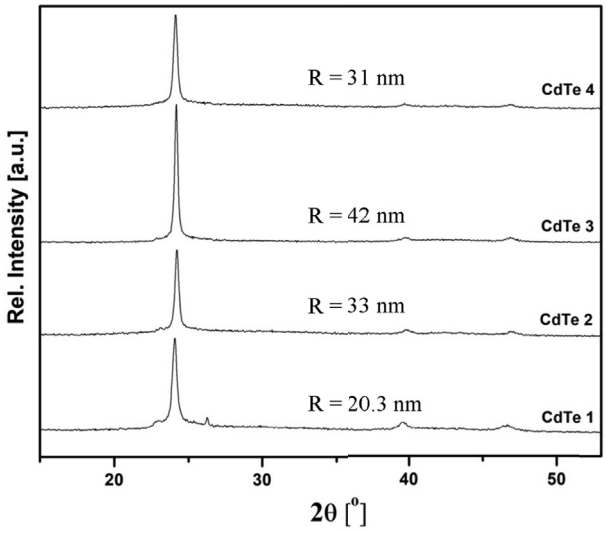

Fig. 3. XRD analysis of CdTe thin films of different thickness. Obtained crystallite sizes (R) are presented too.

Table 1
Parameters obtained from XRD measurements and FIR reflection spectroscopy. Thin films thickness - d, Crystallite size – R.

Name	d [μm]	R [nm]	ω_{l1} (ω_+) [cm^{-1}]	ω_{l2} (ω_-) [cm^{-1}]	ω_P [cm^{-1}]	ω_t [cm^{-1}]	f
CdTe 4	0.39	31.0	187	103	137.5	140.0	0.53
CdTe 2	0.43	33.0	174	78	96.6	140.5	0.53
CdTe 3	0.71	42.0	170	65	79.5	139	0.53
CdTe 1	0.72	20.3	165	30	35.2	140.5	0.53

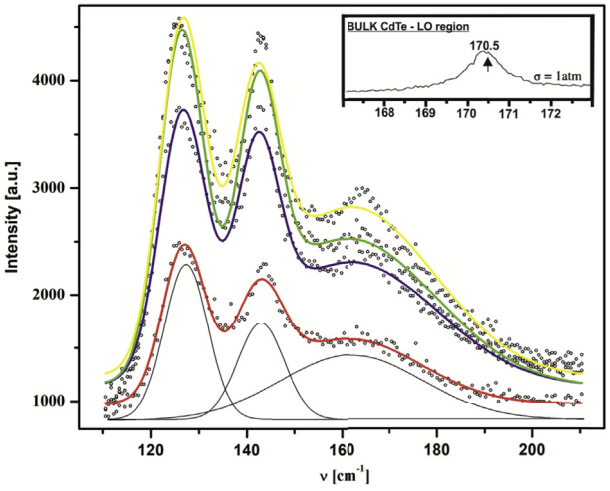

Fig. 4. Raman spectra of CdTe thin films of different thickness. Experimental spectra are shown by open dots. Solid lines are sums of three Lorentz profiles as it shown for spectrum of CdTe 1. In the top right corner LO region of bulk CdTe is presented, taken from the literature [32].

$r_{ij} = (n_i - n_j)/(n_i + n_j) = (\sqrt{\varepsilon_i} - \sqrt{\varepsilon_j})(\sqrt{\varepsilon_i} + \sqrt{\varepsilon_j})$ describe Fresnel coefficients, A_i and A_r represent amplitudes of incident and reflection beams, n is complex index of refraction, ε is the dielectric constant and $\alpha = 2\pi\omega d(\varepsilon_2)^{1/2}$ is the complex phase change related to the absorption in the crystal layer with the thickness d.

Reflectance, R, is given with:

$$R = |R_A|^2 \tag{5}$$

In this case we decided to use dielectric function which takes into consideration the existence of plasmon – phonon interaction in advance.

The dielectric function of the CdTe crystal layer is:

$$\varepsilon_2(\omega) = \varepsilon_{\infty CdTe} \prod_{j=1}^{2} \frac{\omega^2 + i\gamma_{lj}\omega - \omega_{lj}^2}{\omega(\omega + i\Gamma_p)(\omega^2 + i\gamma_t\omega - \omega_t^2)} \tag{6}$$

The ω_{lj} and γ_{lj} ($j = 1, 2$), parameters of the first numerator are the eigenfrequencies and damping coefficients of the longitudinal plasmon-phonon (LP + LO) waves, that arise as a result of the interaction of the initial phonon ($\omega_{LO,CdTe} = 170.5\ cm^{-1}$) and plasmons ($\omega_P$) modes. The parameters of the denominator correspond to the similar characteristics of the transverse vibrations (ω_t, γ_t) and plasmon damping Γ_P. As a result of the best fit, we obtain coupled mode frequencies (ω_{l1} and ω_{l2}).

The dielectric function of the glass substrate is:

$$\varepsilon_s(\omega) = \varepsilon_{\infty\ sup} \prod_{k=1}^{n} \frac{\omega_{LOk}^2 - \omega^2 + i\gamma_{LOk}\omega}{\omega_{TOk}^2 - \omega^2 + i\gamma_{TOk}\omega} \tag{7}$$

where ω_{TO} and ω_{LO} are the transversal and longitudinal optical vibrations, and γ_{TO} and γ_{LO} are damping parameters, respectively.

In our case, layer 2 consists of a CdTe crystals and air (see Fig. 6). The size of the crystallites (R) is given in Fig. 2 and Table 1. These crystallites are described by a dielectric function given in Eq. (1) or Eq. (6) and located randomly in homogeneous environment ε_1 (air) and occupy a volume fraction f, so we can use effective medium theory and Maxwell - Garnet mixing rule, given with Eq. (2).

The far – infrared reflectivity spectrum of the glass substrate is shown in Fig. 7(e). The calculated spectrum, presented by solid line, was obtained using the dielectric function given by equation (7). As a result of the best fit we obtained three modes, whose characteristic frequency are $\omega_{TO1} = 60\ cm^{-1}$, $\omega_{LO1} = 140\ cm^{-1}$, $\omega_{TO2} = 441\ cm^{-1}$, $\omega_{LO1} = 443\ cm^{-1}$ and $\omega_{TO3} = 471\ cm^{-1}$, $\omega_{LO3} = 522\ cm^{-1}$. Frequency values of these modes have remained the same during the fitting procedure for all CdTe thin film samples.

The parameters obtained by the best fit between the experimental results and the models for CdTe film described earlier are also given in Table 1. The far-infrared spectra of CdTe thin films, in the spectral range of 80–600 cm^{-1}, at room temperature, are presented in Fig. 7. Experimental data are presented by circles, while the solid lines are calculated spectra obtained by a fitting procedure based on the previously presented model. Experimental and theoretical spectra show an excellent match.

The thicknesses of our films obtained by Far – infrared spectroscopy are 20% greater, which is within the limits of error for both techniques. When using Far – infrared spectroscopy for calculating thickness of layered structured, we bring errors in absolute measurements, because we calculate effective thickness. The important thing is, the trend is the same, the films does not differ in the relative thickness, i.e. thickness ratios between films are the same.

We note that the thickness (d) of the film changes in the range of ~0.39–~0.7 μm. While the thickness of the film is in the 0.40 μm region, the crystallite size is about 32 nm, and for a film thickness of about 0.72 μm, we have two sizes of crystallites different for a factor of 2. In addition, from Table 1, we have for thicker films CdTe 1 and CdTe 3, that the position of the coupled plasmon-phonon mode ω_{l1} is below the values of $\omega_{LO,CdTe} = 170.5\ cm^{-1}$. On the other hand, these values are above $\omega_{LO,CdTe}$ for thin films CdTe 2 and CdTe 4. In both cases plasmon damping (Γ_p) is relatively low. The obtained eigenfrequencies of the plasmon – phonon coupled modes for CdTe thin films are presented in Fig. 8. As a result of the best fit from Fig. 7, we obtained the frequencies of coupled modes (ω_{l1} and ω_{l2}) marked by open circles and transverse mode frequencies which are denoted by - x. Value of ω_P are calculated by Refs. [16–18]:

$$\omega_P = \frac{\omega_{l1}\omega_{l2}}{\omega_t} \tag{8}$$

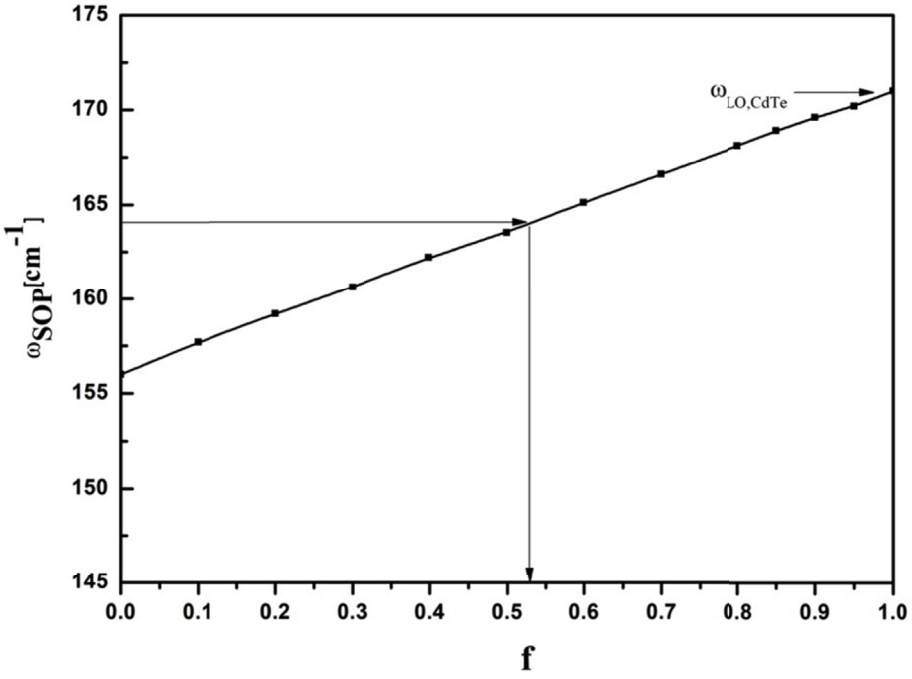

Fig. 5. Surface optical phonon (SOP) mode position vs. filing factor.

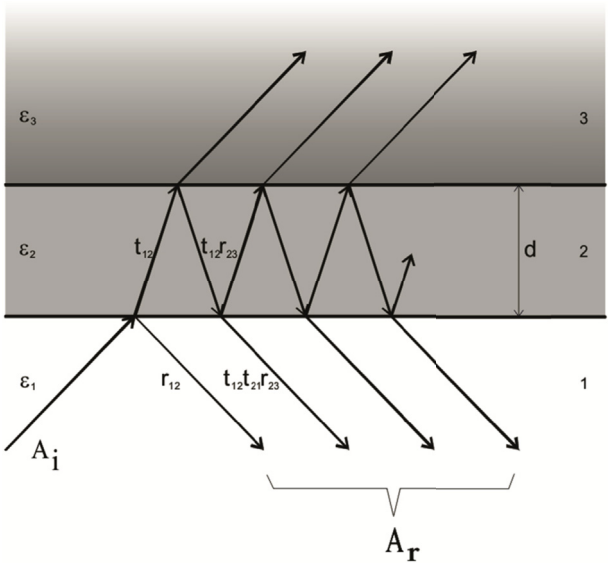

Fig. 6. Schematic presentation of a three layer structure [46].

The calculated lines at Fig. 7 are solution of a real part of uncoupled dielectric function (Eq. (1)). However, for plasma-phonon modes positions are obtained:

$$\omega_{\pm} = \frac{\omega_P^2 + \omega_{LO}^2}{2} \pm \sqrt{\frac{(\omega_P^2 + \omega_{LO}^2)^2 - \omega_P \omega_{TO}}{4}} \quad (9)$$

The full lines in Fig. 7 were obtained for the case $\omega_{LO,CdTe} = 170.5\,cm^{-1}$. It is clear that all values of ω_{l1} and ω_{l2} are out of this theoretical model. Best fit, dashed lines in Fig. 7, was obtained for $\omega_{SOP} = 164\,cm^{-1}$ which in Eq. (9) plays a role ω_{LO}. Shift of about $7\,cm^{-1}$ is registered in relation to $\omega_{LO,CdTe}$, just like in the case of Raman spectra. As we said earlier, the LO phonon shift of CdTe crystal is attributed to the surface optical phonon (SOP) mode effect.

Based on these results, it is clear that in the case of CdTe thin films, prepared by using thermal evaporation technique, the filing factor is constant and does not depend on film thickness, crystallite size and

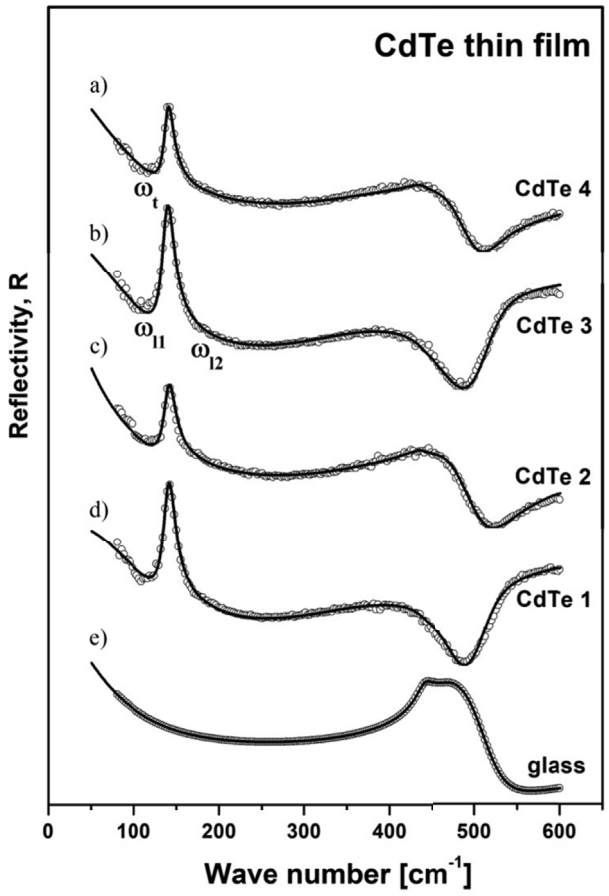

Fig. 7. Far – infrared reflection spectra of: CdTe thin films with thickness of (a) 0.39 μm, (b) 0.71 μm, (c) 0.43 μm, (d) 0.72 μm, and glass substrate (e). Experimental spectra are presented by circles while solid lines are calculated spectra obtained by a fitting procedure based on the model given by Eqs. (2) and (4)–(7).

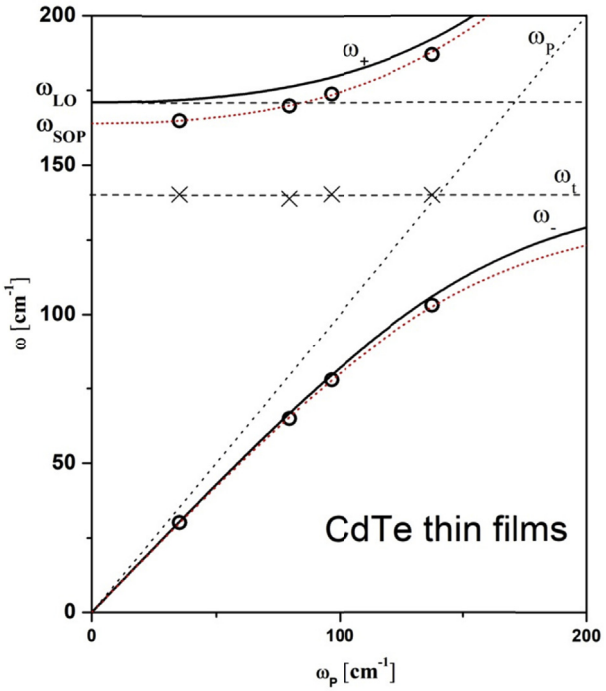

Fig. 8. The eigenfrequencies of the plasmon–phonon modes for CdTe thin films. The lines are calculated spectra [Re{ε_2} = 0; ε_2 is given by Eq. (1)]: solid line with $\omega_{LO,CdTe}$ = 170.5 cm^{-1}; dashed line with ω_{SOP} = 164 cm^{-1}; ○ - ω_{l1}, ω_{l2}; x – ω_t.

concentration of free carriers. On the other hand, the reflection spectra depend on the thickness of the film and the concentration of free carriers in the film, which is expected. In general, thin films have a higher concentration of free carriers ($\sim\omega_p$) (see Table 1). The linear dependence of the position of the SOP mode on the filing factor causes the existence of a modified plasmon – phonon interaction, where the SOP has the role of the LO phonon.

Of course, there are many models that can describe the registered frequency shift of the LO phonon in CdTe e.g. a continuum model of the optical phonon confinement [47,48] would also give a shift of 7 cm^{-1}, but for spherical nanoparticles of about 5 nm, which is far from our case.

4. Conclusion

In this paper, we present results of investigation of CdTe thin films prepared with thermal evaporation technique, with different thicknesses. Sample's surfaces are rather flat, but still they are characterized with bright protrusions and dark holes (air) resulting in a small surface roughness of several nanometers. We showed that, when using thermal evaporation technique we get high quality thin films, especially for thicker films with greater crystallite size. We conclude that the filling factor of our thin films is constant and does not depend on film thickness, crystallite size or concentration of free carriers, but yet has linear dependence on SOP position. This kind of morphology, with filling factor of ~50% causes existence of surface optical phonon and its interaction with plasmon, because of the free surface around nanoparticles. A numerical model for calculating the reflectivity coefficient for complex system, which includes films and substrate, has been applied, and CdTe thin film were treated as a mixture of homogenous spherical inclusion in air modeled by Maxwell – Garnet formula.

Acknowledgements

This research was financially supported by the Serbian Ministry of Education and Science (Project 45003) and in Poland by National Science Center granted under decision No. DEC-2011/01/B/ST5/06602. The authors would like to express their gratitude to King Khalid University, Saudi Arabia for providing administrative and technical support.

References

[1] S. Chandra Ray, K. Mallick, Int. J. Chem. Eng. Appl. 4 (2013) 183–186.
[2] C.S. Ferekides, U. Balasubramanian, R. Mamazza, V. Viswanathan, H. Zhao, D.L. Morel, Sol. Energy 77 (2004) 823–830.
[3] R. Kulkarni, et al., Energy Procedia 110 (2017) 188–195.
[4] A. Arnoult, J. Cibert, Appl. Phys. Lett. 66 (1995) 2397–2399.
[5] P. Bhattacharya, D.N. Bose, Semicond. Sci. Technol. 6 (1991) 384–387.
[6] A.U. Ubale, D.K. Kulkarni, Indian J. Pure Appl. Phys. 44 (2006) 254–259.
[7] T.L. Chu, S.S. Chu, C. Ferekides, J. Britt, C.Q. Wu, J. Appl. Phys. 71 (1992) 3870.
[8] A. Nakano, et al., Sol. Cell. 17 (1986) 233.
[9] K.S. Rahman, F. Haque, 3rd International Conference on the Developments in Renewable Energy Technology (ICDRET), 2014, pp. 29–31.
[10] S. Lalitha, S. Zh Karazhanov, P. Ravindran, S. Senthilarasu, R. Sathyamoorthy, J. Janabergenov, Physica B 387 (2007) 227–238.
[11] S. Singh, et al., Thin Solid Films 519 (2010) 1078–1081.
[12] D.S. Chuu, C.M. Dai, W.F. Hsieh, C.T. Tsai, J. Appl. Phys. 69 (1991) 12.
[13] A. Singha, B. Satpati, P.V. Satyam, A. Roy, J. Phys. Condens. Mater. 17 (2005) 5708–5967.
[14] M. Gilić, J. Trajić, N. Romčević, M. Romčević, D.V. Timotijević, G. Stanišić, I.S. Yahia, Opt. Mater. 35 (2013) 1112–1117.
[15] M. Cardona (Ed.), Top. Appl. Phys, vol. 8, Springer, Berlin, 1975.
[16] N. Romčević, M. Romčević, A. Golubović, Le Van Khoi, A. Mycielski, Đ. Jovanović, D. Stojanović, S. Nikolić, S. Đurić, J. Alloy. Compd. 397 (2005) 52–57.
[17] M. Romčević, N. Romčević, V.N. Nikiforov, Infrared Phys. Technol. 42 (2001) 541–545.
[18] N. Romčević, M. Romčević, A. Milutinović, S. Kostić, J. Alloy. Compd. 478 (2009) 41–44.
[19] J. Trajić, M. Romčević, N. Romčević, B. Babić, B. Matović, P. Balaž, Opt. Mater. 57 (2016) 225–230.
[20] N. Romčević, M. Romčević, W.D. Dobrowolski, L. Kilanski, M. Petrović, J. Trajić, B. Hadzić, Z. Lazarević, M. Gilić, J.L. Ristic-Djurović, N. Paunović, A. Reszka, B.J. Kowalski, I.V. Fedorchenko, S.F. Marenkin, J. Alloy. Compd. 649 (2015) 375–379.
[21] J. Trajić, N. Romčević, M. Romčević, V.N. Nikiforov, Mater. Res. Bull. 42 (2007) 2192–2201.
[22] M. Romčević, N. Romčević, W. Dobrowolski, L. Kalinski, J. Trajić, D.V. Timotijević, E. Dynowska, I.V. Fedorchenko, S.F. Marenkin, J. Alloy. Compd. 548 (2013) 33–37.
[23] N. Romčević, J. Trajić, T.A. Kuznetsova, M. Romčević, B. Hadžić, D.R. Khokhlov, J. Alloy. Compd. 442 (2007) 324–327.
[24] J. Trajić, N. Romčević, M. Romčević, D. Stojanović, R. Rudolf, T.A. Kuznetsova, D.R. Khokhlov, J. Alloy. Compd. 493 (2010) 41–46.
[25] J. Trajić, N. Romčević, M. Romčević, D. Stojanović, L.I. Ryabova, D.R. Khokhlov, J. Alloy. Compd. 602 (2014) 300–305.
[26] R.W. Cheary, A. Coelho, J. Appl. Crystallogr. 25 (1992) 109–121.
[27] R. Triboulet & P. Siffert, first ed., Elsevier, 2010.
[28] H. Zeng, W. Cai, B. Cao, J. Hu, Y. Li, P.S. Liu, Appl. Phys. Lett. 88 (2006) 181905.
[29] A. Ghosh, R.N.P. Chodhary, J. Phys. D Appl. Phys. 42 (2009) 075416.
[30] F. Friedrich, N.H. Nickel, Appl. Phys. Lett. 91 (2007) 111903.
[31] J. Xu, W. Ji, X.B. Wang, H. Shu, Z.X. Shen, S.H. Tang, J. Raman Spectrosc. 29 (1998) 613.
[32] V.C. Stergiou, Y.S. Raptis, E. Anastassakis, N. Pelekaneos, A. Nahmani, J. Cibert, Phys. Status Solidi 223 (2001) 237.
[33] J.F. Scott, T.C. Damem, Optic Commun. 5 (1972) 410.
[34] R. Rossetti, S. Nakahara, L.E. Bru, J. Chem. Phys. 79 (1983) 1086.
[35] B.F. Variano, N.E. Schlotter, D.M. Hwangand, C.J. Sandroff, J. Chem. Phys. 88 (1988) 2848.
[36] A.V. Baranov, Y.S. Bobovich, N.I. Grebenshchikova, V.I. Petrov, M.Y. Tsenter, Optic Spectrosc. 60 (1986) 685.
[37] H. Jerominek, M. Pigeon, S. Patela, Z. Jakubczk, C. Delisle, R.J. Tremblay, Appl. Phys. 63 (1986) 957.
[38] E.F. Hilinski, P.A. Lucas, J. Chem. Phys. 89 (1988) 3435.
[39] J. Trajić, M. Gilić, N. Romčević, M. Romčević, G. Stanišić, B. Hadžić, M. Petrović, Y.S. Yahia, Sci. Sinter. 47 (2015) 145–152.
[40] G. Irmer, J. Raman Spectrosc. 38 (2007) 634.
[41] K. Karkkainen, A. Saviola, K. Nikoskinen, IEEE Trans. Geosci. Rem. Sens. 39 (5) (2001) 1013.
[42] J.C.M. Garnett, Trans. Roy. Soc. Can. CIII (1904) 385420.
[43] A. Saviola, I. Lindell, A. Priou (Ed.), Dielectric Properties of Heterogeneous Materials PIER 6 Progres in Electromagnetic Research, Elsevier, Amsterdam, 1992, pp. 101–115 1.
[44] B. Hadzić, N. Romcević, M. Romcević, I. Kuryliszyn-Kudelska, W. Dobrowolski, J. Trajić, D.V. Timotijević, U. Narkiewicz, D. Sibera, J. Alloy. Compd. 540 (2012) 49–56.
[45] M. Gilić, et al., Infrared Phys. Technol. 76 (2016) 276–284.
[46] J. Trajić, M. Gilić, N. Romčević, M. Romčević, G. Stanišić, Z. Lazarević, D. Joksimović, I.S. Yahia, Phys. Scr., T 162 (2014) 014031.
[47] R. Roca, C. Trallero-Giner, M. Cardona, Phys. Rev. B 49 (1994) 13704.
[48] M.P. Chamberlain, C. Trallero-Giner, M. Cardona, Phys. Rev. B 51 (1995) 1680.

Received: 23 May 2019 | Revised: 22 July 2019 | Accepted: 23 July 2019

DOI: 10.1002/jrs.5718

RESEARCH ARTICLE

WILEY Journal of RAMAN SPECTROSCOPY

Raman spectroscopy of zinc oxide nanoplatelets modified with ruthenium (II) complexes

Jasna L. Ristić-Djurović[1] | Leunam Fernández-Izquierdo[2,3] | Branka Hadžić[1] | Linnavel Jiménez-Hernández[4] | Alicia M. Díaz-García[3] | Jelena Mitrić[1] | Biljana Babić[1] | Maja Romčević[1] | Saša Ćirković[1] | Nebojša Romčević[1]

[1] Institute of Physics, University of Belgrade, Belgrade, Serbia

[2] Faculty of Chemistry, Pontifical Catholic University of Chile, Santiago, Chile

[3] Bioinorganic Laboratory (LBI), Department of Inorganic and General Chemistry, University of Havana, Havana, Cuba

[4] Institute of Material Science and Technology (IMRE), University of Havana, Havana, Cuba

Correspondence
Jasna L. Ristić-Djurović, Institute of Physics, University of Belgrade, Pregrevica 118, Belgrade, Serbia.
Email: jasna@stanfordalumni.org

Funding information
Serbian Ministry of Education, Science, and Technological Development, Grant/Award Number: III-45003

Abstract

We analyzed and compared the unmodified and three modified zinc oxide nanoplatelet materials. The three components used in zinc oxide modification were the 4,4′-bipyridine and two ruthenium (II) complexes, namely, the *trans*-$[Ru(bpy)(bpyCOO)Cl_2]^{2-}$ and *cis*-$[Ru(bpy)(bpyCOO)Cl_2]^{2-}$. The obtained results revealed that after modification, ZnO nanoplatelets became smaller and embedded in the materials used for the modification. When ZnO was modified with either of the two ruthenium (II) complexes, the interaction between them led to a higher activity of ZnO. The metal-to-ligand charge transfer that was also detected in the two cases of ZnO nanoplatelets modified with the ruthenium (II) complexes caused significant alteration of the Raman spectrum and consequent changes of the optical properties. Various forms of ruthenium (II) complexes were used in several published studies related to dye-sensitized solar cells and biomedicine. The biomedical applications include, for example, the ATP (adenosine-5′-triphosphate) detection, interaction with human serum albumin, DNA analysis, and cancer detection and treatment. The properties of the ZnO nanoplatelets modified with the two ruthenium (II) complexes presented here indicate that it may be worth exploring if the studied materials are applicable in the dye sensitized solar cells and biomedicine. Possible advantage of our results is that they were obtained at room temperature.

KEYWORDS

nanocomposite, semiconductor, spectroscopy

1 | INTRODUCTION

The ruthenium complexes have been often used in research areas related to biomedical applications[1–7] and have emerged as potential candidates for use in dye-sensitized solar cells (DSSCs).[8–13] Compared with conventional inorganic crystals, donor–acceptor substituted organic molecules with nonlinear optical properties have advantages such as the optical damage threshold, lower dielectric constant, fast response time, tunability of optical properties by chemical modification, and low production cost.[14,15] Zinc oxide and TiO_2 are the most commonly used semiconductors in dye-sensitized solar cells. They both have the same electron affinities and almost the same band gap energies; however, ZnO has much higher electron diffusivity, high electron mobility, and large excitation binding energy; it is stable against photo-corrosion and is available at low-cost.[16] Also, ZnO has probably

the richest variety of nanostructures due to a very broad range of synthesis methods.[17] An excellent review of ZnO-based dye-sensitized solar cells is given by Anta et al. as well as by Vittal and Ho.[16,17] Various nanostructures such as nanoparticles, hierarchical aggregates, porous films, nanosheets, nanowires, and tetrapods are most often combined with the ruthenium-based dyes and the iodide/triiodide redox couple. The highest power conversion rate of DSSC with ZnO of 7.5%[18] is lower than the long-standing record of 11.1%[19] and the highest reported so far of 12.3%.[20] In addition to the most commonly investigated use in the solar cells, emerge applications of ruthenium based dyes in other scientific fields, for example, in biomedicine.[1–7] Ruthenium (II) complexes were shown to bind to DNA defects[7] as well as to be a quantitative DNA detectors.[3] Recently, a number of studies have suggested them as a potential photodynamic agents in the cancer therapy,[4–6] live-cell imaging,[21,22] ATP (adenosine-5′-triphosphate) detection,[1] interaction with HSA (human serum albumin),[2] and theranostic applications.[23]

In addition to the DSSC and biomedicine, other fields of application emerge as well. Ruthenium dyes have been successfully used to generate electrostatically stabilized gold colloides,[24] whereas Ru/TiO_2 has been employed as a catalyst in the selective methanation of CO.[25] A number of recent studies are devoted to the materials that incorporate ruthenium, for example, the ruthenium doped ZnO nanorods,[26] amorphous silicon ruthenium thin films embedded with nanocrystals,[27] Ru-doped ZnS quantum dots,[28] ruthenium complexes bound to CdSe nanoparticles,[29] hybrid materials including the Zn (II)-Ru (II) complexes,[30] trinuclear ruthenium complex, Ru-red,[31] and isolated and agglomerated gold nanoparticles functionalized with a ruthenium dye.[24]

The Raman scattering, a sensitive, nondestructive characterization tool, has been used to obtain information about sample quality as well as to analyze specific aspects of lattice dynamics, namely, the isotopic effects, phonon lifetimes, position of doping ions in a host lattice, and presence of impurities that are undetectable by the X-ray analysis.[32,33] In particular, the vibrational properties of ZnO in the form of nanostructured samples and thin films, as well as of the bulk ZnO, were investigated in a number of studies using Raman spectroscopy. The variety of studied ZnO properties include the multiphonon processes, electron–phonon coupling, dopant incorporation, local atomic arrangement, changes in samples with annealing process, and temperature dependence of Raman modes.[34–39]

The aim of the work presented here is to characterize the ZnO nanoplatelets (NPs) modified with the *trans*-[Ru (bpy)(bpyCOO)Cl_2]$^{2-}$ and *cis*-[Ru (bpy)(bpyCOO)Cl_2]$^{2-}$ in order to establish if further investigation of their possible use in the fields of dye-sensitized solar cells and biomedicine is worthwhile. The NPs of ZnO, its combination with 4,4′-bipyridine (4,4′-bpy) as well as with two ruthenium (II) complexes, are characterized using X-ray diffraction (XRD), photoluminescence, and Raman spectroscopy.

2 | MATERIALS AND METHODS

The synthesis of modified ZnO NPs was undertaken by the precipitation method and the 4,4′-bpy as a surfactant. The 4,4′-bpy was used as a bridge in the synthesis of ruthenium (II) complexes, as well. The ruthenium (II) complexes *trans*-[Ru (bpy)(bpyCOO)Cl_2]$^{2-}$and *cis*-[Ru (bpy)(bpyCOO)Cl_2]$^{2-}$ with 2,2′-bipyridine and 2,2′-bipyridine 4,4′-dicarboxilic acid as ligands were obtained as depicted in Fig. 1 and were further adhered to ZnO NPs. The *trans*- and *cis*- ruthenium (II) complexes are abbreviated as SAh and SA, respectively. Consequently, the four studied nanomaterials are ZnO NPs, ZnO NPs–4,4′-bpy, ZnO NPs–SA, and ZnO NPs–SAh. The additions to ZnO NPs, namely, the 4,4′-bpy, SA, and SAh, are shown in Fig. 2.

Scanning electron microscopy (SEM) images of the samples were obtained with the high-resolution electron microscope MIRA3 FEG-SEM, Tescan, using accelerating voltages lower than 20 kV. The samples were prepared for SEM imaging by coating them with an ultrathin gold layer in the SC7620 Mini Sputter Coater, Quorum Technologies.

Structural characteristics of all samples were obtained using the XRD powder technique. Philips PW 1050 diffractometer equipped with a PW 1730 generator was used. All samples were examined under the same conditions, namely, 40 kV × 20 mA, using Ni filtered Co Kα radiation of 0.1778897 nm at room temperature. Measurements were carried out in the 2-hr range of 10–80^{o} with the scanning step of 0.05^{o} and 10 s scanning time per

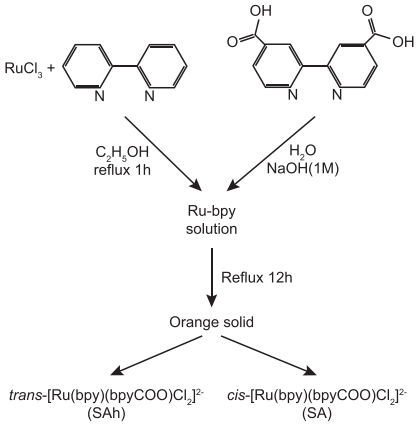

FIGURE 1 Synthesis of ruthenium complexes

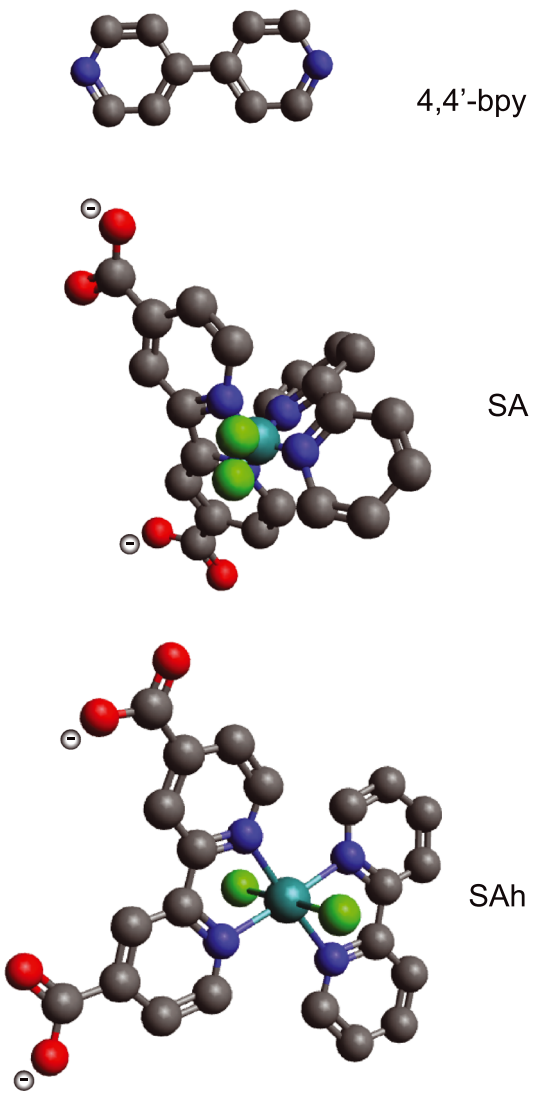

FIGURE 2 Compounds used to modify zinc oxide nanoplatelets. The ZnO nanoplatelets were modified using the 4,4′-bipyridine, as well as ruthenium (II) complexes *cis*-[Ru (bpy)(bpyCOO)Cl_2]$^{2-}$ and *trans*-[Ru (bpy)(bpyCOO)Cl_2]$^{2-}$, further referred to as the 4,4′-bpy, SA, and SAh, respectively [Colour figure can be viewed at wileyonlinelibrary.com]

step. Crystallite size was determined with the XFIT computing program, which is based on the fundamental parameter convolution approach.[40]

The photoluminescence spectrum excited by argon laser line at 514.5 nm was measured at room temperature using the Jobin Yvon model U-1000 monochromator with a conventional photocounting system.

The micro-Raman spectra were taken in the backscattering configuration with the Jobin Yvon T64000 spectrometer, equipped with nitrogen cooled charge-coupled-device detector. As was the case with the photoluminescence spectrum, the 514.5-nm line of an Ar-ion laser was used as the excitation source. The measurements were performed at room temperature using the laser power of 20 mW. All samples were investigated in the spectral range between 100 and 1,700 cm^{-1}.

3 | RESULTS AND DISCUSSION

3.1 | SEM measurements

The representative SEM images of the four studied materials are given in Fig. 3, whereas the sets of images with three values of magnification are provided in Fig. S1 in the Supporting Information. The unmodified ZnO particles can be classified as NPs because their thickness is of the order of 50 nm. This is confirmed by the four examples of NPs whose thickness is equal or smaller than 40 nm, given in the image corresponding to ZnO NPs in Fig. 3. Note that the thickness of 40 nm is somewhat smaller than 50 nm, which is the step size of the scale. The modified ZnO NPs, namely, the ZnO NPs–4,4′-bpy, ZnO NPs–SA, and ZnO NPs–SAh appear to be coated with the material used in the modification, that is, with 4,4′-bpy, SA, and SAh. Further, SA and SAh seem to have caused clustering and agglomeration, which is more pronounced for ZnO NPs–SAh.

3.2 | XRD measurements

The structure of prepared samples was identified using the XRD patterns shown in Fig 4. The diffractograms show intense peaks of ZnO originating from (110), (002), (101), (102), (110), (103), and (112) and confirm that the structures crystallized in the hexagonal wurtzite, P63mc, structure shown in the insert in the top right corner of Fig 4. All the marked peaks are in good agreement with the JCPDS card 36-145. All the other peaks originate from the modifiers. Because 4,4′-bpy was used as a surfactant, ZnO NP sample shows not only the peaks of pure ZnO but the peaks of 4,4′-bpy as well. That is why this diffractogram is very similar to the one that corresponds to ZnO NPs–4,4′-bpy. However, the peaks that correspond to 4,4′-bpy are more intense in the diffractogram of ZnO NPs–4,4′-bpy because in this case 4,4′-bpy was used not only as a surfactant in the synthesis of ZnO but as a capping agent, as well. The ZnO crystallite size is calculated for all the samples and is found to be 35.8, 19.2, 10.6, and 7.5 nm for ZnO NPs, ZnO NPs–4,4′-bpy, ZnO NPs–SA, and ZnO NPs–SAh, respectively. Consequently, the ZnO crystallite size is significantly smaller in the modified material, that is, in the presence of the capping agent. Note that for unmodified ZnO NPs, the particle sizes calculated from the XRD patterns of 35.8 nm agree well with the NP thicknesses found from the SEM images to be of the order of 40 nm. In the case of the modified ZnO

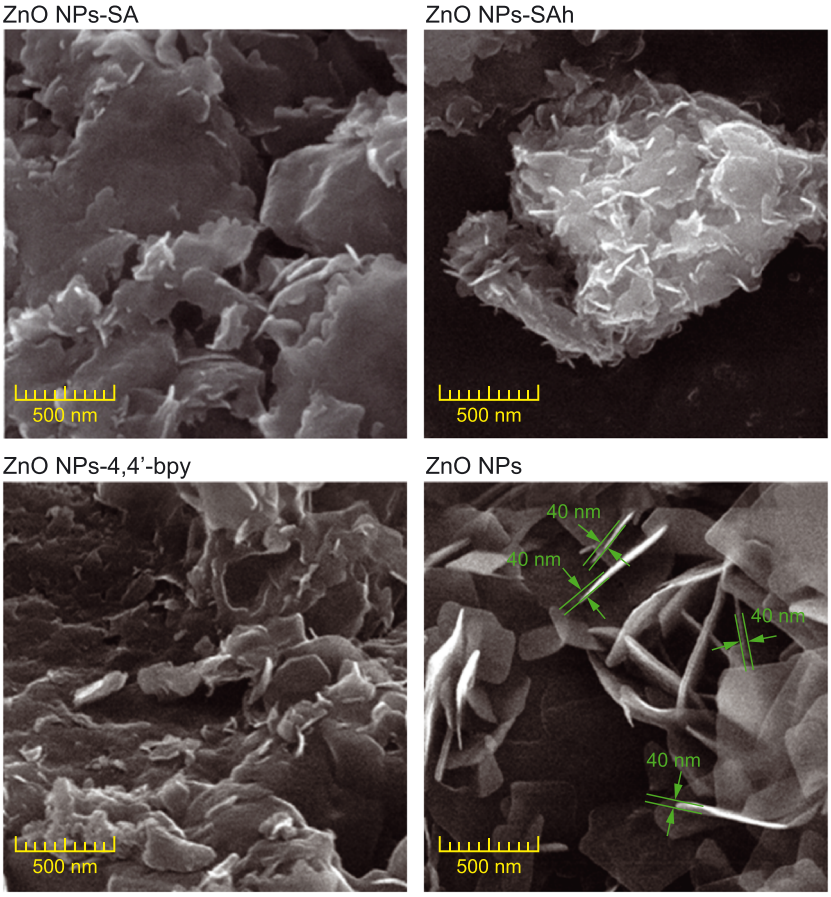

FIGURE 3 Scanning electron microscopy images. The micrographs of the four studied materials are given here with the magnification of 133,000, whereas Fig. S1 contains the micrographs with the magnification values of 55,700 and 267,000, as well. Nanoplatelets of ZnO are about 40 nm thick. In the modified material ZnO NPs are coated with the modifier and are clustered [Colour figure can be viewed at wileyonlinelibrary.com]

NPs, the particle sizes obtained from SEM images are bigger than those calculated by the XRD patterns, which suggests particle aggregation.

3.3 | Photoluminescence measurements

The luminescence spectrum of the four studied samples is given in Fig. 5. Given that our excitation wavelength was 514.5 nm, our study is limited to the broad long-wavelength part of the spectrum. Photoluminescence spectra are often analyzed using the convolution of the Lorentzian functions that are given with

$$I(\omega) = \frac{2A}{\pi} \frac{W}{4(\omega - \omega_c)^2 + W^2}, \quad (1)$$

where I, ω_c, W, and A are the line intensity, position of the maximum, half-width of the peak, and parameter that depends on W, respectively. The measured data depicted with circles in Fig. 5 is approximated with the calculated red curve, which represents the sum of the components each defined with Equation (1) and shown with green lines.

The spectra of ZnO NPs and those modified with 4,4′-bpy can be decomposed into four components positioned at ω_c values of approximately 553, 605, 634, and 678 nm. Various forms of ZnO exhibit two luminescence bands, namely, a short-wavelength band, which is located near the absorption edge, and a broad long-wavelength band, the maximum of which is in the green spectral range.[41] Impurities, zinc vacancies, oxygen vacancies, interstitial zinc ions, oxygen antisites, and transitions from interstitial zinc ions to zinc vacancies as well as a combination of various centers were assumed to be responsible for the green luminescence.[41] In our case, these are described with the Lorentzians positioned at the ω_c values of 605, 634, and 678 nm.

Modification with 4,4′-bpy caused significant enhancement of the relative contribution of the peak at 553 nm, which can be attributed to 4,4′-bpy. This peak is visible in the spectrum of unmodified ZnO NPs because 4,4′-bpy was used as a surfactant in ZnO NPs synthesis.

However, in the spectra of ZnO NPs modified with the ruthenium (II) complexes, ZnO NPs–SA, and ZnO NPs–SAh, the component at 553 nm is not present. Instead, the peak at 678 nm became much stronger and metal-to-ligand charge transfer introduced the component at 737 nm.[42] Consequently, it seems that ZnO in ZnO NPs–SA and ZnO NPs–SAh became more active due to the interaction between ZnO and ruthenium (II) complex. In the spectrum corresponding to ZnO NPs–SAh relative intensity of the peak at 637 nm became larger than

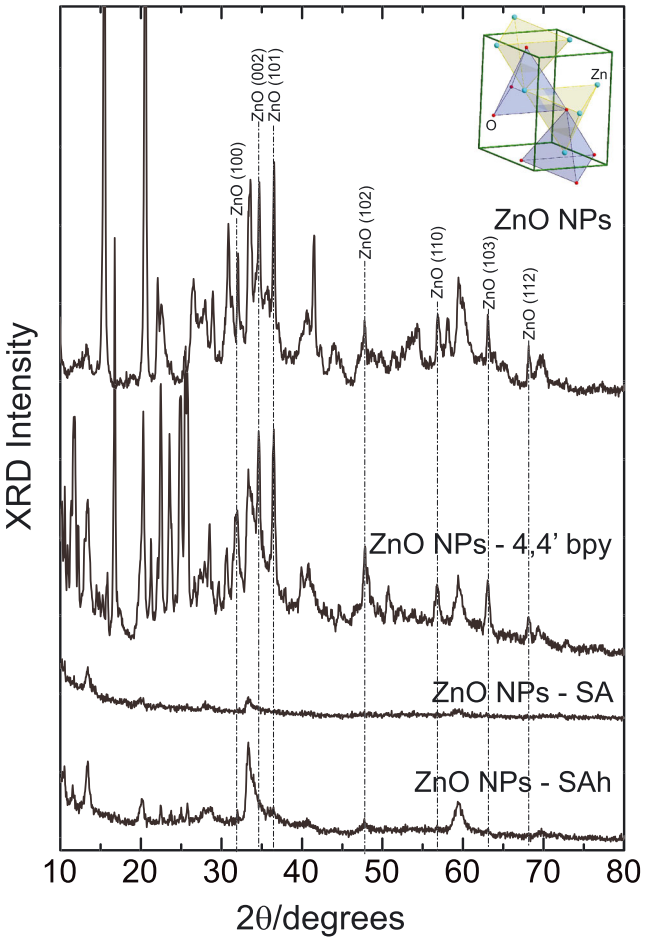

FIGURE 4 X-ray diffraction patterns. The insert shows the structure of the ZnO crystallite, that is, the hexagonal wurtzite, P63mc [Colour figure can be viewed at wileyonlinelibrary.com]

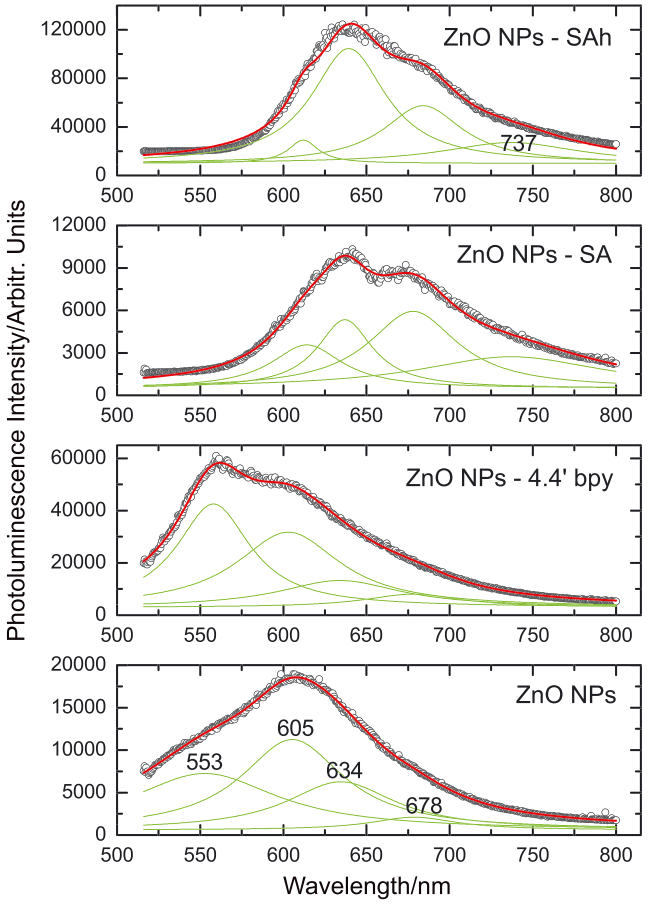

FIGURE 5 Photoluminescence. The photoluminescence spectra of the four analyzed samples were measured at room temperature with the excitation source of 514.5 nm. The measured data depicted with circles are approximated with the calculated thick red line that represents the sum of the Lorentzian components given as the thin green lines. The parameters of each Lorentzian component are given in Table S1 [Colour figure can be viewed at wileyonlinelibrary.com]

was the case in the ZnO NPs–SA spectrum. The fluorescence emission spectra of Ru $(bpy)_3^{2+}$ incorporated in silica gel film studied by Innocenzi et al. seem to have similar structure as our result corresponding to ZnO NPs modified with 4,4'-bpy; however, their structure is centered at 603 nm, whereas ours is located at approximately 554 nm.[42] Table S1 in the Supporting Information gives the parameters of spectral components obtained by decomposing our spectra.

For the five Ru (II) complexes studied by Ji et al. the wavelengths of 594, 626, 626/667/726, 631, and 620 nm were obtained.[43] Note that their third complex has centers located at similar positions as our samples with SA and SAh. With the increase of external hydrostatic pressure, the spectra of two complexes considered by Pannwitz et al. seem to develop similarities with our spectra; however, their peaks are at somewhat larger wavelengths.[44] To the contrary, the spectra of Ru (II) complexes given by Oner et al. in the region above 500 nm exhibit structures centered at somewhat smaller wavelength than is the case with our spectra.[45] The spectra corresponding to all the modified samples are similar to those considered by McConnell et al. with respect to detecting DNA defects.[7] However, in order to obtain peaks, their spectra had to be recorded at 77 K, whereas our spectra were measured at room temperature.

3.4 | Raman spectroscopy

The Raman spectra and peak assignments of the four studied nanomaterials are given in Fig. 6 and Table 1, respectively. In the Raman spectrum of unmodified ZnO NPs the peaks were recorded at 290, 319, 404, 440, 679, 937, 1,048, 1,353, 1,435, and 1,589 cm^{-1}. The peaks at 404 and 440 cm^{-1} are the well-known peaks that are characteristic to ZnO, and they correspond to E_1 (TO) and E_2^{high}, respectively. The peak E_2^{high} is less intense than usually due to a high luminescence of the sample. All

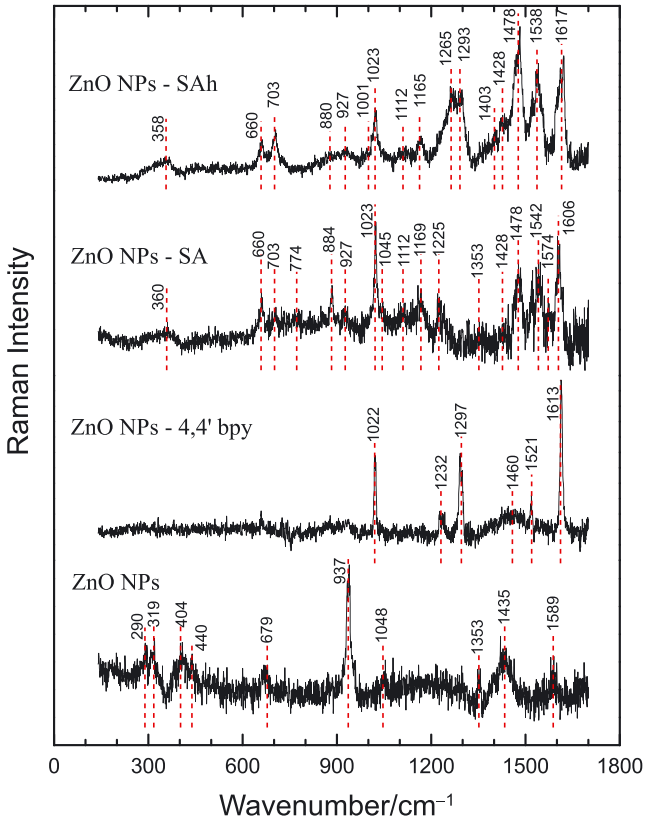

FIGURE 6 Raman spectra. The Raman spectra of the four samples were obtained at room temperature with 514.5-nm excitation source [Colour figure can be viewed at wileyonlinelibrary.com]

the other peaks are the multiphonon peaks or the second harmonics (second order Raman peaks). The obtained results are in good agreement with previously reported results for pure ZnO.[32] The Raman spectra of ZnO are usually taken in the spectral range between 99 and 1,160 cm^{-1} because it is only the multiphonon peaks and second harmonics that exist above 618 cm^{-1}. In our study, the Raman spectra were taken in the wider range due to the peaks expected to correspond to the 4,4′-bpy, SA, and SAh used in the three remaining samples.

When ZnO NPs were modified with 4,4′-bpy, the Raman spectrum changed significantly. Most of the ZnO peaks disappeared and the peaks that correspond to 4,4′-bpy became dominant. The part of our Raman spectrum that can be related to the 4,4′-bpy contains the peaks located at 1,022, 1,232, 1,297, 1,521, and 1,613 cm^{-1} as well as the wide structure centered at approximately 1,460 cm^{-1}. The peak at 1,297 cm^{-1} is the inter-ring stretch (Ω), whereas the peak at 1,613 cm^{-1} is the ring stretch (8a). The peak that represent the ring in-plane deformation (12) is located at 1,022 cm^{-1} in our spectrum; however, in the works of Castellà-Ventura and E. Kassab[46] and Ould-Moussa et al.[47] this peak is positioned at 1,000 and 1,038 cm^{-1}. For our peak at 1,232 cm^{-1} that represent the CH in-plane bend (9a) Castellà-Ventura and E. Kassab[46] reported the experimental peak position at 1,218 cm^{-1} and scaled calculated position of 1,227 and 1,235 cm^{-1}. The peak at 1,521 cm^{-1} representing the CH in-plane bend and ring stretch (19a) is in Castellà-Ventura and E. Kassab[46] given by the experimental value of 1,511 cm^{-1} and scaled calculated value of 1,523 cm^{-1}. The wide structure centered at approximately 1,460 cm^{-1} is a consequence of the three peaks that represent the CH in-plane bend and ring stretch at 1,406 (19b), 1,424 (19b), and 1,487 cm^{-1} (19a).[46] In Castellà-Ventura and E. Kassab[46] and Ould-Moussa et al.[47] there is no information regarding the laser used as an excitation source. Consequently, the discrepancy between their reported peak positions and our measurements may be caused by different excitation sources. In Moissette et al.[48] the infrared laser light of 1,064 nm was used to detect the 4,4′-bpy peaks at 999, 1,075, 1,227, 1,294, 1,508, 1,597, and 1,616 cm^{-1}, which is in good agreement with our peaks. On the other hand, using the laser light of 532 nm, Pérez León et al.[49] reported the 4,4′-bpy peaks at 1,024, 1,273, 1,490, 1,537, and 1,630 cm^{-1} and characterization of the peak at 1,024 cm^{-1} as the ring breathing band. The blue laser light of 488 nm was employed by Rzeźnicka et al.[50] to obtain the 4,4′-bpy peaks at 1,016, 1,337, 1,533, and 1,630 cm^{-1}. With all this in mind it can be concluded that our results corresponding to ZnO NPs–4,4′-bpy show a fairly good agreement with the data found in the literature.

In the Raman spectra of ZnO NPs–SA the existence of peaks that belong to the both phases is evident. In addition to the wide structure at approximately 360 cm^{-1}, there are peaks at 660, 703, 774, 884, 927, 1,023, 1,045, 1,112, 1,169, 1,225, 1,353, 1,428, 1,478, 1,542, 1,574, and 1,606 cm^{-1}. Both phases have several peaks at the very similar positions, causing the peaks at those positions to be wider and asymmetric as well as making the spectral analysis more complex. Note the wide structure whose center is approximately at 360 cm^{-1}. In Hureau et al.[51] the peak at 360 cm^{-1} is reported to correspond to SA. However, ZnO has a multiphonon peak at 333 cm^{-1} and A_1 (TO) peak at 378 cm^{-1}.[32] The asymmetry of our peak at 660 cm^{-1} is a consequence of coexistence of the ZnO multiphonon peak at 660 cm^{-1} as well as the SA peak at 657 cm^{-1}. The peak at 703 cm^{-1} is the multiphonon ZnO peak. The peak at 774 cm^{-1} combines the ZnO multiphonon peak at 773 cm^{-1} and the SA peak at 781 cm^{-1}. The peaks at 884, 927, and 1,023 cm^{-1} are the SA peaks. The peak at 1,045 cm^{-1} consists of the SA peak at 1,031 cm^{-1} and the ZnO multiphonon peak at 1,044 cm^{-1}. The peak at 1,112 cm^{-1} is composed of the ZnO multiphonon peak at 1,105 cm^{-1} and SA peak at 1,114 cm^{-1}, whereas the peak at 1,169 cm^{-1} is a mixture of ZnO multiphonon peak at 1,158 cm^{-1} and SA peak at

TABLE 1 Raman peak assignments

Raman wavenumber/cm^{-1}						
Experimental results						
ZnO NPs	ZnO NPs–4,4′-bpy	ZnO NPs–SA	ZnO NPs–SAh	Reference	Phase	Assignment
290				284[32]	ZnO	B_1^{high}-B_1^{low}
319				333[32]	ZnO	E_1^{high}-E_1^{low}
		360	358	333[32] 306[24], 376[31] 378[32]	ZnO SA/SAh ZnO	E_1^{high}-E_1^{low} Ru–N stretch A_1 (TO)
401				410[32]	ZnO	E_1 (TO)
440				438[32]	ZnO	E_2^{high}
		660	660	657[51] 657[32], 666[32]	SA/SAh ZnO	 TA+LO
679				666[32]	ZnO	TA+LO
		703	703	692[51] 700[32]	SA/SAh ZnO	 LA+TO
		774		773[32] 778[31]	ZnO SA	LA+TO Ru–O
		884	880	896[51]	SA/SAh	
		927	927	934 812[32], 980[32]	SA/SAh ZnO	 LA+LO, 2TO
937				812[32], 980[32]	ZnO	LA+LO, 2TO
			1,001	999[48], 1,000[51]	SAh	
	1,022	1,023	1,023	1,016[50], 1,024[49,51], 1,029[24]	4,4′-bpy/SA/SAh	in-plane def. (12), ring breath
1,048		1,045		1,029[24], 1,031, 1,038[47] 1,044[32]	SA ZnO	ring breath TO+LO
		1,112	1,112	1,105[32] 1,114[51], 1,119[25]	ZnO SA/SAh	2LO C–O–C
		1,169	1,169	1,158[32] 1,169[51]	ZnO SA/SAh	$2A_1$(LO), $2E_1$(LO), 2LO
	1,232	1,225		1,227[48], 1,235[46]	4,4′-bpy/SA	CH in-plane bend (9a)
			1,265	1,264[24], 1,273[51]	SAh	CN stretch
	1,297		1,293	1,290[51], 1,294[48], 1,300[24]	4,4′-bpy/SAh	Inter-ring stretch (Ω), COO stretch
1,353		1,353			ZnO SA	multi-phonon, second order
			1,403	1,401[51]	SAh	
		1,428	1,428	1,424[47]	SA/SAh	CH in-plane bend, ring stretch (19b)
1,435					ZnO	multiphonon, second order
	1,460			1,406[47] 1,424[47]	4,4′-bpy 4,4′-bpy	CH in-plane bend, ring stretch (19b) CH in-plane bend, ring stretch (19b)

(Continues)

TABLE 1 (Continued)

Raman wavenumber/cm^{-1}						
Experimental results						
ZnO NPs	ZnO NPs–4,4′-bpy	ZnO NPs–SA	ZnO NPs–SAh	Reference	Phase	Assignment
				1,487[47]	4,4′-bpy	CH in-plane bend, ring stretch (19a)
		1,478	1,478	1,456[51], 1,477[24], 1,484[51]	SA/SAh	asymmetric CC+CN stretch
	1,521			1,511[47], 1,523[46], 1,531[47]	4,4′-bpy	CH in-plane bend, ring stretch (19a)
		1,542	1,538	1,545[24]	SA/SAh	asymmetric CC+CN stretch
1,589					ZnO	multiphonon, second order
		1,574			SA	
		1,606			SA	
	1,613		1,617	1,614[24], 1,615[51]	SAh	symmetric CC+CN stretch

Abbreviations: 4,4′-bpy: 4,4′-bipyridine; NPs: nanoplatelets.

1,169 cm^{-1}. The peaks at 1,225, 1,353, 1,478, 1,574, and 1,606 cm^{-1} belong to the SA phase. The differences in SA peak positions in our measurements and those reported in Hureau et al.[51] are due to different laser lights used in the two experiments. An excitation sources in Hureau et al.[51] were red and infrared lasers at 632 and 1,064 nm, respectively, compared with 514-nm laser light used in our experiment. The excitation source wavelength may be the reason for the two peaks in our spectra that can be attributed to SA, the very intense peak at 1,542 cm^{-1} and less intense peak at 1,428 cm^{-1}. The peak at 1,542 cm^{-1} is too strong to be the second harmonic of the peak at 774 cm^{-1}.

When compared with the Raman spectrum of ZnO NPs–SA, the spectrum of ZnO NPs–SAh has better signal-to-noise ratio as well as more symmetric peaks. From our experience with other coated nanoparticles, this can be a consequence of the difference in the coating layer thickness. The spectrum has two wide asymmetric structures centered at approximately 358 and 927 cm^{-1} and the peaks at 660, 703, 880, 1,001, 1,023, 1,112, 1,165, 1,265, 1,293, 1,403, 1,428, 1,478, 1,538, and 1,617 cm^{-1}. The wide structures are composed of peaks that belong to both phases, ZnO and SAh. The ZnO peaks at 333 and 378 cm^{-1} and the SAh peak at 360 cm^{-1} form the wide structure centered at approximately 358 cm^{-1}, whereas the wide structure centered at approximately 927 cm^{-1} is composed of the SAh peak at 934 cm^{-1} and the ZnO peak at 980 cm^{-1}. The ZnO peaks at 333 and 980 cm^{-1} are the multiphonon peaks, whereas the peak at 378 cm^{-1} is of the type A_1 (TO). All other peaks in our spectrum belong to the SAh phase and show good agreement with peaks reported in Hureau et al.,[51] namely, the peaks at 657, 692, 896, 1,000, 1,024, 1,114, 1,169, 1,273, 1,290, 1,401, 1,456, 1,484, and 1,615 cm^{-1}. Small differences in peak position are due to different laser lights used as an excitation source. This may also cause the existence of the peaks at 1,428 and 1,538 cm^{-1} in our spectra, whereas in Hureau et al.[51] the existence of peak at 1,456 cm^{-1} is reported.

The fluorescence spectra showed that the excitation wavelength is in the visible light range; therefore, the ZnO NPs modified with the two considered ruthenium (II) complexes can be regarded as prospective candidates for use in energy conversion. Future studies can develop towards applying these materials in DNA analysis. For example, it can be investigated if use of our modified ZnO NPs in altering an electrode of a cell for electrochemiluminescence spectra measurement will prove efficient as was the case with the pristine carbon nanotube that was used by Tang et al.[3] Application of the analyzed materials in detecting DNA defects seems promising because our photoluminescence spectra were recorded at room temperature, whereas those employed for this purpose by McConnell et al.[7] were measured at 77 K.

4 | CONCLUSION

The unmodified zinc oxide nanoplatelets (ZnO NPs) and three modifications of these ZnO NPs were analyzed. The three materials used for the modification were the 4,4′-bpy and the two ruthenium (II) complexes of equal composition but with two different geometries, namely, the *cis* and *trans* geometry. The three modified materials were denoted as ZnO NPs–4,4′-bpy, ZnO NPs–SA (for *cis* geometry), and ZnO NPs–SAh (for *trans* geometry). It was found that in the modified ZnO, the ZnO NPs are smaller and coated with the material used for the modification. The metal-to-ligand charge transfer was detected in the ZnO modified with the SA and SAh ruthenium (II) complexes, which caused significant changes of the Raman spectrum and consequent alteration of the optical properties. Because 4,4′-bpy was used as a surfactant in the synthesis of ZnO NPs as well as in further modification of one of the three studied modified ZnO NPs, the spectral component at 553 nm that corresponds to 4,4′-bpy was detected in the luminescence spectrum of ZnO NPs as well as of ZnO NPs–4,4′-bpy. As expected, this peak is stronger in the spectrum of ZnO NPs–4,4′-bpy, namely, in the case when 4,4′-bpy was used as a modifier as well as a surfactant. In the spectra of ZnO NPs modified with the ruthenium (II) complexes SA and SAh three important changes were detected. Namely, the 4,4′-bpy-related peak at 553 nm disappeared, the peak that corresponds to the metal-to-ligand charge transfer appeared at 737 nm, and the peak at 678 nm that is a characteristics of ZnO became much stronger. Consequently, it seems that the interaction between ZnO and ruthenium (II) caused ZnO to be more active. The obtained results indicate that it can be beneficial to pursue investigation towards the application of the studied materials in the DSSC and DNA analysis.

ACKNOWLEDGEMENTS

This work is financially supported by the Serbian Ministry of Education, Science, and Technological Development (III-45003). The authors thank M. Mitrić and B. Jokić for their help with XRD and SEM measurements.

ORCID

Jasna L. Ristić-Djurović https://orcid.org/0000-0002-5344-1892
Branka Hadžić https://orcid.org/0000-0001-5459-7461
Jelena Mitrić https://orcid.org/0000-0002-1526-3976
Maja Romčević https://orcid.org/0000-0002-5064-175X

REFERENCES

[1] E. Babu, P. Muthu Mareeswaran, A. Ramdass, P. Ramesh, S. Rajagopal, *J. Lumin.* **2016**, *175*, 267.

[2] N. Cacita, S. Nikolaou, *J. Lumin.* **2016**, *169*, 115.

[3] X. Tang, D. Zhao, J. He, F. Li, J. Peng, M. Zhang, *Anal.Chem.* **2013**, *85*, 1711.

[4] S. M. Cloonan, R. B. P. Elmes, M. Erby, S. A. Bright, F. E. Poynton, D. E. Nolan, S. J. Quinn, T. Gunnlaugsson, D. C. Williams, *J. Med. Chem.* **2015**, *58*, 4494.

[5] L. Zeng, P. Gupta, Y. Chen, E. Wang, L. Ji, H. Chao, Z. -S. Chen, *Chem. Soc. Rev.* **2017**, *46*, 5771.

[6] J. Zhang, K. -L. Wong, W. -K. Wong, N. -K. Mak, D. W. J. Kwong, H. -L. Tam, *Org. Biomol. Chem.* **2011**, *9*, 6004.

[7] A. J. McConnell, M. H. Lim, E. D. Olmon, H. Song, E. E. Dervan, J. K. Barton, *Inorg. Chem.* **2012**, *51*, 12511.

[8] S. Shah, I. M. Noor, J. Pitawala, I. Albinson, T. M. W. J. Bandara, B. -E. Mellander, A. K. Arof, *Opt. Mater. Express* **2017**, *7*, 2069.

[9] C. -Y. Huang, C. -F. You, C. -E. Cheng, B. -C. Lei, J. -C. Jhang, F. -C. Yu, C. -S. Chang, F. S. -S. Chien, *Opt. Mater. Express* **2016**, *6*, 1024.

[10] M. A. Gaikwad, M. P. Suryawanshi, P. S. Maldar, T. D. Dongale, A. V. Moholkar, *Opt. Mater.* **2018**, *78*, 325.

[11] S. Kushwaha, L. Bahadur, *J. Lumin.* **2015**, *161*, 426.

[12] O. Wiranwetchayan, W. Promnopas, K. Hongsith, S. Choopun, P. Singjai, S. Thongtem, *Res. Chem. Intermed.* **2016**, *42*, 3655.

[13] K. Sim, S. -J. Sung, S. -N. Park, D. -H. Kim, J. -K. Kang, *Opt. Mater. Express* **2013**, *3*, 739.

[14] J. M. Hales, J. Matichak, S. Barlow, S. Ohira, K. Yesudas, J. L. Bradas, J. W. Perry, S. R. Marder, *Science* **2010**, *19*, 1466.

[15] Y. Li, J. Li, R. Su, J. Cui, *Opt. Mater.* **2013**, *36*, 437.

[16] R. Vittal, K. -C. Ho, *Renewable and Sustainable Energy Reviews* **2017**, *70*, 920.

[17] J. A. Anta, E. Guillén, R. Tena-Zaera, *J. Phys. Chem.* **2017**, *C116*, 11413.

[18] N. Memarian, I. Concina, A. Braga, S. M. Rozati, A. Vomiero, G. Sberveglieri, *Angew. Chem., Int. Ed.* **2011**, *50*, 12321.

[19] Y. Chiba, A. Islam, Y. Watanabe, R. Komiya, N. Koide, L. Han, *Jpn. J. Appl. Phys.* **2006**, *45*, L638.

[20] A. Yella, H. -W. Lee, H. N. Tsao, C. Yi, A. K. Chandiran, M. K. Nazeeruddin, E. W. -G. Diau, C. -Y. Yeh, S. M. Zakeeruddin, M. Grätzel, *Science* **2011**, *334*, 629.

[21] W. -K. Tsui, L. -H. Chung, M. M. -K. Wong, W. -H. Tsang, H. -S. Lo, Y. Liu, C. -H. Leung, D. -L. Ma, S. -K. Chiu, C. -Y. Wong, *Sci. Rep. –UK* **2014**, 09070.

[22] N. Karaoun, A. K. Renfrew, *Chem. Commun.* **2015**, *51*, 14038.

[23] C. R. Cardoso, M. V. S. Lima, J. Cheleski, E. J. Peterson, T. Venâcio, N. P. Farrell, R. M. Carlos, *J. Med. Chem.* **2014**, *57*, 4906.

[24] D. Grasseschi, A. L. A. Parussulo, V. M. Zamarion, R. R. Guimarães, K. Araki, H. E. Toma, *J. Raman Spectrosc.* **2014**, *45*, 758.

[25] L. M. Martínez Tejada, A. Muñoz, M. A. Centeno, J. A. Odriozola, *J. Raman Spectrosc.* **2016**, *47*, 189.

[26] S. Kumar, P. Kaur, C. L. Chen, R. Thangavel, C. L. Dong, Y. K. Ho, J. F. Lee, T. S. Chan, T. K. Chen, B. H. Mok, S. M. Rao, M. K. Wu, *J. Alloy. Compd.* **2014**, *588*, 705.

[27] A. Guo, W. Li, X. Jiang, C. Wang, Y. Jiang, *J. Raman Spectrosc.* **2015**, *46*, 619.

[28] R. Sahraei, F. Mohammadi, E. Soheyli, M. Roushani, *J. Lumin.* **2017**, *187*, 421.

[29] N. Bair, J. M. Hancock, C. J. Simonson, S. W. Thalman, J. S. Colton, M. C. Asplund, R. G. Harrison, *J. Lumin.* **2015**, *158*, 501.

[30] S. S. Chavan, S. B. Pawal, S. R. Lolage, *J. Lumin.* **2017**, *181*, 261.

[31] K. S. Joya, H. J. M. de Groot, *J. Raman Spectrosc.* **2013**, *44*, 1195.

[32] R. Cuscó, E. Alarcón-Lladó, J. Ibáñez, L. Artús, J. Jiménez, B. Wang, M. J. Callahan, *Phys. Rev. B* **2007**, *75*, 165202.

[33] Y. Liu, J. L. MacManus-Driscoll, *Appl. Phys. Letters* **2009**, *94*, 022503.

[34] J. Xu, W. Ji, X. B. Wang, H. Shu, Z. X. Shen, S. H. Tang, *J. Raman Spectrosc.* **1998**, *29*, 613.

[35] H. Zeng, W. Cai, B. Cao, J. Hu, Y. Li, P. Liu, *Appl. Phys. Lett.* **2006**, *88*, 181905.

[36] N. Romčević, R. Kostić, B. Hadžić, M. Romčević, I. Kuryliszin-Kudelska, W. Dobrowolski, U. Narkievicz, D. Sibera, *J. Alloy. Compd.* **2010**, *507*, 386.

[37] M. Millot, J. Gonzalez, I. Molina, B. Salas, Z. Golacki, J. M. Broto, H. Rakoto, M. Gorian, *J. Alloy. Compd.* **2006**, *423*, 224.

[38] R. P. Wang, G. Xu, P. Jin, *Phys. Rev. B* **2004**, *69*, 113303.

[39] R. Y. Sato-Berrú, A. Vázquez-Olmos, A. L. Fernández-Osorio, S. Sotres-Martínez, *J. Raman Spectrosc.* **2007**, *38*, 1073.

[40] R. W. Cheary, A. Coelho, *J. Appl. Cryst.* **1992**, *25*, 109.

[41] P. A. Rodnyi, I. V. Khodyuk, *Opt. Spectrosc.* **2011**, *111*, 776.

[42] P. Innocenzi, H. Kozuka, T. Yoko, *J. Phys. Chem. B* **1997**, *101*, 2285.

[43] S. Ji, W. Wu, W. Wu, P. Song, K. Han, Z. Wang, S. Liu, H. Guo, J. Zhao, *J. Mater. Chem.* **2010**, *20*, 1953.

[44] A. Pannwitz, S. Poirier, N. Blanger-Desmarais, A. Prescimone, O. S. Wenger, C. Reber, *Chem. Eur. J.* **2018**, *24*, 7830.

[45] I. Oner, C. Sahin, C. Varlikli, *Dyes Pigments* **2012**, *92*, 23.

[46] M. Castellà-Ventura, E. Kassab, *J. Raman Spectrosc.* **1998**, *29*, 511.

[47] L. Ould-Moussa, O. Poizat, M. Castellà-Ventura, G. Buntinx, E. Kassab, *J. Phys. Chem.* **1996**, *100*, 2072.

[48] A. Moissette, Y. Batonneau, C. Brémard, *J. Am. Chem. Soc.* **2001**, *123*, 1232.

[49] C. Pérez León, L. Kador, B. Peng, M. Thelakkat, *J. Phys. Chem. B* **2006**, *110*, 8723.

[50] I. I. Rzeźnicka, H. Horino, N. Kikkawa, S. Sakaguchi, A. Morita, S. Takahashi, T. Komeda, H. Fukumura, T. Yamada, M. Kawai, *Surf. Sci.* **2013**, *617*, 1.

[51] M. Hureau, K. S. Smirnov, A. Moissette, H. Jobic, *Phys. Chem. Chem. Phys.* **2014**, *16*, 7562.

SUPPORTING INFORMATION

Additional supporting information may be found online in the Supporting Information section at the end of the article.

How to cite this article: Ristic-Djurovic JL, Fernández-Izquierdo L, Hadzic B, et al. Raman spectroscopy of zinc oxide nanoplatelets modified with ruthenium (II) complexes. *J Raman Spectrosc*. 2019;1–10. https://doi.org/10.1002/jrs.5718

Infrared Physics and Technology 108 (2020) 103345

Contents lists available at ScienceDirect

Infrared Physics & Technology

journal homepage: www.elsevier.com/locate/infrared

Plasmon – Phonon interaction in $ZnSnSb_2$ + Mn semiconductors

Maja Romcevic[a,*], Novica Paunovic[a], Uros Ralevic[a], Jelena Pesic[a], Jelena Mitric[a], Jelena Trajic[a], Lukasz Kilanski[b], Witold Dobrowolski[b], Irina Valentinovna Fedorchenko[c,d], Sergey Fedorovich Marenkin[c,d], Nebojsa Romcevic[a]

[a] Institute of Physics, University of Belgrade, Belgrade, Serbia
[b] Institute of Physics, Polish Academy of Sciences, Warsaw, Poland
[c] Kurnakov Institute of General and Inorganic Chemistry, Russian Academy of Science, Moscow, Russian Federation
[d] College of New Materials and Nanotechnologies, National University of Science and Technology, Moscow, Russian Federation

ARTICLE INFO

Keywords:
Semiconductors
Lattice defects
Optical properties
Phonon properties
Plasmon - phonon interaction

ABSTRACT

Semiconductors of II-IV-V_2 type with chalcopyrite structure have been studied for several decades. Due to advances in materials synthesis technologies, and doping with various elements, the possibilities of their application have expanded. In this paper, polycrystalline $ZnSnSb_2$ + Mn was examined with the aim to explain the connection of its high free carrier concentration with the material structure and influence on optical properties. Two samples of $Zn_{1-x}Mn_xSnSb_2$ with different compositions (x = 0.027 and x = 0.076) and significant difference in carrier concentrations were analyzed. Their structural properties were examined by x-ray diffraction, optical microscopy, and AFM. The existence of several different phases - $ZnSnSb_2$, ZnSb, SnSb, and small amounts of Sn and MnSb, as well as very complex microstructures, were registered. It was found that the high free carrier concentrations are caused by a large number of defects, especially zinc vacancies. Optical properties were analyzed using IR spectroscopy at room temperature. Based on the analysis of IR reflection spectra, the presence of plasmon - phonons interaction was registered. It was determined that three $ZnSnSb_2$ phonons of B_2 symmetry interact with plasma, which then leads to the change of their positions. A detailed analysis of this interaction provides insight into the behavior of some other material parameters. Also, vibration modes of ZnSb and SnSb phases were registered on the spectra. Knowledge of phonon behavior and their interaction with plasma is important for possible applications, especially as a thermoelectric material.

1. Introduction

Semiconductors have been widely used thanks to the ability to adapt to different requirements. The II-IV-V_2 chalcopyrite semiconductors have been intensively studied in recent decades [1]. The fields of their application are considerably expanded by doping with various impurities. A significant breakthrough was achieved by the addition of magnetic impurities, whereby ferromagnetism at room temperature was achieved [2,3]. The synthesis technology of this class of compounds has been developed, but it is still adapting to new requirements [4]. Zn-Sn-Sb based alloys have required thermoelectric properties and find application as low-toxic thermoelectric materials [5,6,7]. The engineering of structural, transport, electrical, optical, magnetic properties as well as other material parameters, goes along with the increasing application of this class of semiconductors.

$ZnSnSb_2$ is II-IV-V_2 type material with the tetragonal chalcopyrite structure, narrow gap of 0.7 eV at room temperature, high concentration of free carriers (10^{21}–10^{22} cm^{-3}) and inhomogeneous structure [8,9]. In this paper we analyzed ferromagnetic semiconductor $ZnSnSb_2$ + Mn, which has interesting magnetic properties, such as paramagnet-ferromagnet transition with the Curie temperature about 522 K and the cluster-glass behavior with the transition temperature about 465 K, caused by the formation of MnSb clusters in the material [10]. The $Zn_{1-x}Mn_xSnSb_2$ samples were obtained using direct fusion method, and characterization of their structural, magnetic, optical and phonon properties were done [9]. We chose two samples with different chemical contents, x = 0.027 and x = 0.076, which we labeled as samples A and B respectively, with the aim to examine their properties in more detail. Main reason was a ten times difference in their free-carrier concentrations (p_A = 13 × 10^{21} cm^{-3} and p_B = 1.2 × 10^{21} cm^{-3}). We wanted to determine what the cause of this difference in concentration is, and whether there is a reaction between the free carriers and the crystal lattice. The question of plasmon-phonon interaction is particularly interesting in the study of thermoelectric

* Corresponding author.
E-mail address: romcevic@ipb.ac.rs (M. Romcevic).

https://doi.org/10.1016/j.infrared.2020.103345
Received 3 February 2020; Received in revised form 23 April 2020; Accepted 25 April 2020
Available online 28 April 2020
1350-4495/

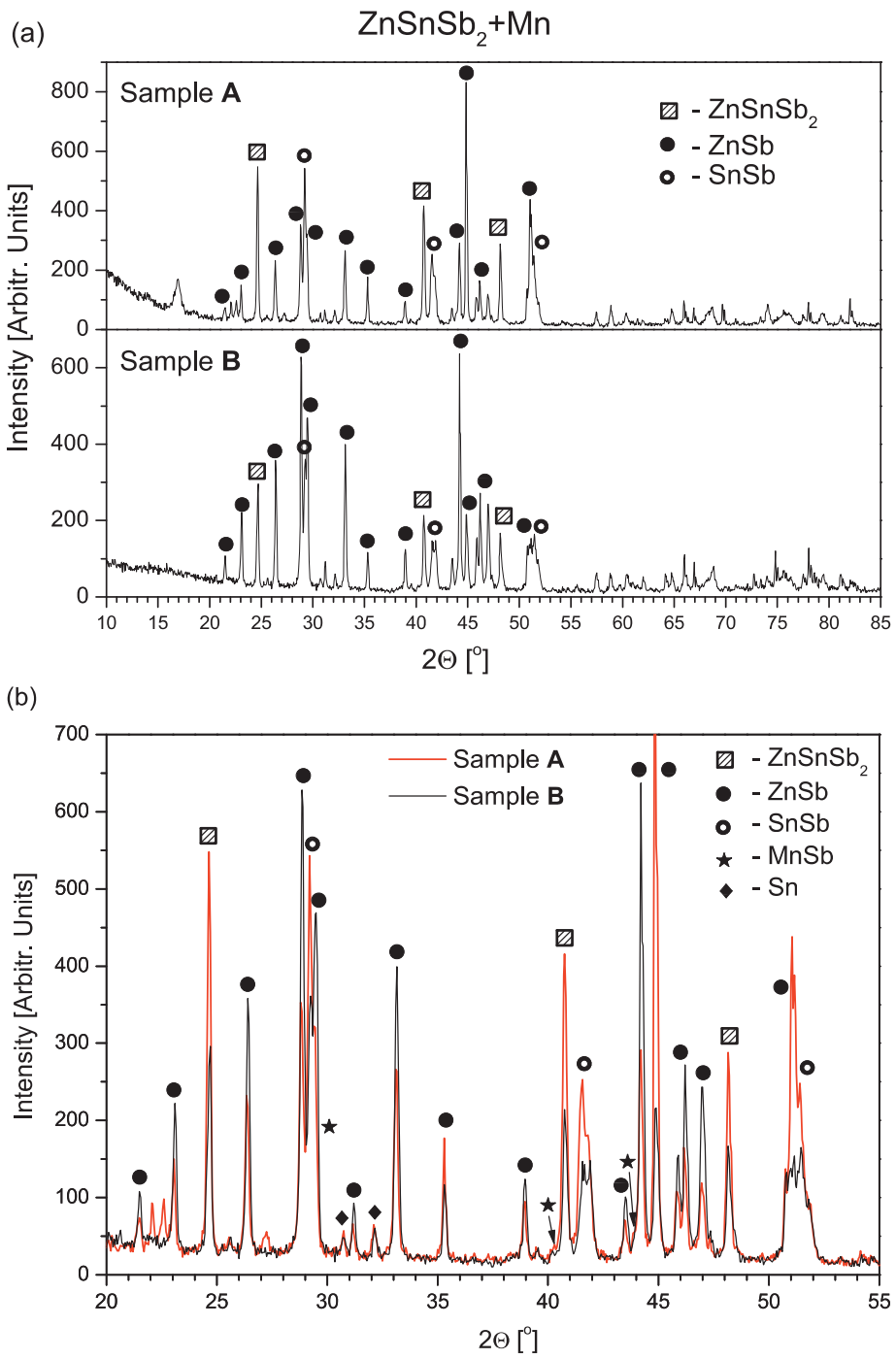

Fig. 1. (a) X-ray diffraction pattern for $ZnSnSb_2$ + Mn samples which contain different amounts of Mn. The registered crystal phases are marked; (b) The two spectra are overlapped to compare their relative intensities.

materials, as well as their electrical and thermal conductivity, and their interdependence.

$ZnSnSb_2$ is not a homogeneous material, and the consequence is that even two samples from the same crystal can have significantly different properties. This is not surprising given the complicated $ZnSnSb_2$ microstructure. Our goal was to analyze the relationship between microstructures, their phonons and free carriers, their conditionality and interactions. For this purpose we used x-ray diffraction, optical microscopy, AFM and IR spectroscopy measurements. Obtained results were analyzed by applying the model for plasmon-phonon interaction.

2. Samples and characterization

$ZnSnSb_2$ semiconductor has a chalcopyrite structure, spatial group I42d, with lattice parameters $a \approx 6.275$ Å and $c \approx 12.55$ Å and ratio c/a close to 2. $ZnSnSb_2$ melts by a peritectic reaction at $T = 362$ °C with a possible phase transformation of the cubic modification into a tetragonal one at $T = 348$ °C [11,12]. The $ZnSnSb_2$ + Mn ferromagnetic semiconductors were synthesized using the method that makes it possible to obtain single crystals at temperatures below the temperature of the peritectic reaction.

The analyzed samples of $Zn_{1-x}Mn_xSnSb_2$ were synthesized by the direct fusion method. High purity components were used for the

synthesis: zinc single crystals (99.999%), shots of tin (99.999%), antimony single crystals (99.999%), and manganese powder (99.999%). They were mixed in stoichiometric ratios.

The reaction mixture was put into a quartz glass tube and heated up to 631 °C. After that, ampoules were quenched to 355 °C and then annealed at 355 °C. This is described in more detail in the papers [12,13]. The synthesized crystals were cut into slices of about 1.5 mm thickness.

The chemical composition of the samples (x) was determined using the energy dispersive x-ray fluorescence method (EDXRF) [10]. Obtained results showed that average Mn content (x) in the samples is between 0.027 and 0.138. All the studied crystals had the correct stoichiometry of $Zn_{1-x}Mn_xSnSb_2$ alloy equal to 1-x : x : 1 : 2, within our measurement accuracy of about 10% of the x value.

Based on the magnetotransport measurements [10] it was found that electrical and magnetotransport parameters, such as resistivity, carrier concentration, and carrier mobility, do not depend linearly on composition, i.e. on the Mn content. Therefore, as mentioned above, two samples with a considerable difference in free-carrier concentrations were selected. The sample with $x = 0.027$ and $p = 13 \times 10^{21}$ cm^{-3} was labeled as sample A and the one with $x = 0.076$ and $p = 1.2 \times 10^{21}$ cm^{-3} as sample B. In this way we wanted to determine the connection between the free carriers and the structural and optical properties of the alloy.

The structural properties of these samples were investigated by the XRD powder technique. Measurements were done using a Philips PW 1050 diffractometer equipped with a PW 1730 generator, 40 kV × 20 mA, using Ni filtered Co Ka radiation of 0.1778897 nm at room temperature. The x-ray diffraction patterns were collected during 2 h in the range of $10-100^{\circ}$ with a scanning step of 0.05° and 10 s scanning time per step. Phase analysis showed that besides the main phase of chalcopyrite $ZnSnSb_2$, the orthorhombic ZnSb, rhombohedral SnSb, and hexagonal MnSb phases are present in the samples. This is consistent with the literature [8,10].

An optical microscope was used to get an insight into the distribution of different phases of the material along the surface. Images were captured using Olympus BH series modular microscope with UIS objective lenses with 50x and 400x enhancement.

The surfaces of $ZnSnSb_2$ + Mn samples were examined in detail using Atomic Force Microscope (AFM), NTEGRA prima from NTMDT. The topography and phase images were acquired simultaneously by operating the AFM in semi-contact mode. NSG01 probes with a typical resonant frequency of 150 kHz and 10 nm tip apex curvature radius were used.

The far-infrared (FIR) reflectivity measurements were done with a BOMEM DA-8 Fourier-transform infrared spectrometer in the spectral range from 40 to 450 cm^{-1} at room temperature. A Hyper beamsplitter and deuterated triglycine sulfate (DTGS) pyroelectric detector were used.

3. Results and discussion

It is known that during the preparation of $ZnSnSb_2$ the polycrystalline material is formed, consisting of the main phase and ZnSb, SnSb and β-Sn inclusions [11].

The structure of the two selected samples was investigated by X-ray diffraction measurements. Obtained results with marked phases are presented in Fig. 1. In Fig. 1(b) the overlap of the results is shown, with the aim to compare their relative intensities. The list of XRD peaks positions and their corresponding Miller indices and phases is given in Table 1 in Supplementary Materials.

Besides the chalcopyrite $ZnSnSb_2$ phase the orthorhombic ZnSb, rhombohedral SnSb, Sn have also been registered, as well as weak lines from hexagonal MnSb inclusions. The idea was to detect differences in the structures of these two samples. It is obvious that diffraction lines corresponding to the $ZnSnSb_2$ phase (squares) are stronger for sample A as well as lines of SnSb phase (open circles). Also, it is clear that lines corresponding to ZnSb (black circles) are mostly stronger for sample B. Existence of the Sn phase is evident, but lines corresponding MnSb phase are barely visible.

Table 1
Expected values of $ZnSnSb_2$ phonons of B_2 and E symmetries, from literature [26].

Phonon	B_2^1	B_2^2	B_2^3	E^1	E^2	E^3	E^4	E^5	E^6
Estimated value [cm^{-1}]	189	199	70	189	185	195	111	88	54

In order to examine the spatial distribution of the existing different crystal phases, the samples were recorded by an optical microscope with two different magnifications (50 × and 400 ×). Obtained micrographs are presented in Fig. 2.

Existing phases are clearly visible and they form multiphase structures. It should be noted that this is a very non-homogeneous material and that images from different parts of the samples differed, so the characteristic ones are selected and shown in Fig. 2.

In our previous work [9] is determined that gray fields are $ZnSnSb_2$ crystal, white ones correspond SnSb phase and that dark parts consist of ZnSb. Micrometric crystals of MnSb in the shape of dark circles were registered also.

Although microstructures of similar shapes have been formed in both samples, it is apparent that the surfaces significantly differ. Based on previous work [8,9,14], it can be concluded that these spherical and needle like microcrystals are ZnSb, MnSb, Sn, and Sb phases formed during crystallization of the material. As can be seen from Fig. 2. the sample B contains a lot of micron-sizes phases relatively evenly distributed over the surface (volume).

In order to more accurately examine the surface of the samples, we used atomic force microscopy (AFM) measurements. The characteristic results are presented in Fig. 3.

The surfaces of both samples have a granular structure. The sample A has evenly distributed grains over the entire surface with a few larger clusters and an average grain height of around ~100 nm (see Fig. 3(a) and the profile in Fig. 3(c)). The phase contrast in Fig. 3(b) originates exclusively from the abrupt changes in the height, indicating that the material properties of the sample A surface are homogeneous. The grains on the surface of the sample B are exclusively arranged into clusters which are not evenly distributed over the surface. The majority of the clusters reach several tens of nm in height, with a few exceptions having a height of ~100 nm (see Fig. 3(d) and the profile in Fig. 3(f)). The phase contrast of the sample B surface shows that the larger clusters have a distinct phase shift, seen as dark and white regions in Fig. 3(e), so that clusters have different material properties than the remainder of the surface.

This material is known to be difficult to synthesize and beside $ZnSnSb_2$ the ZnSb and SnSb phases are formed [11,15]. The series of $Zn_{1-x}Mn_xSnSb_2$ samples were synthesized under the same conditions with the only difference being the starting amounts of manganese and zinc [10]. Obviously, the small variation in the starting mixture causes rather different structures and properties of the materials.

It was found that a large concentration of lattice defects, especially in the cation sublattice, in $ZnSnSb_2$, as well as in other II-IV-V_2 semiconductors [16,17], causes a high hole concentration. In particular, Zn vacancies are those defects that lead to a very high concentration of holes [18,19,20]. Typical hole concentration in $ZnSnSb_2$ is 10^{20} cm^{-3} [15–20], in two-component p-type ZnSb it is 10^{19} cm^{-3} [18,19], while SnSb is a n-type material with metallic character and electron concentration of about 10^{22} cm^{-3} at 1.8 K [21]. Evidently, the electronic structure is very complex in this material.

It is difficult to say exactly what is the cause of different hole concentrations in the $Zn_{1-x}Mn_xSnSb_2$ samples, but it could be assumed that Zn vacancies are the main reason. Sample A has a higher content of

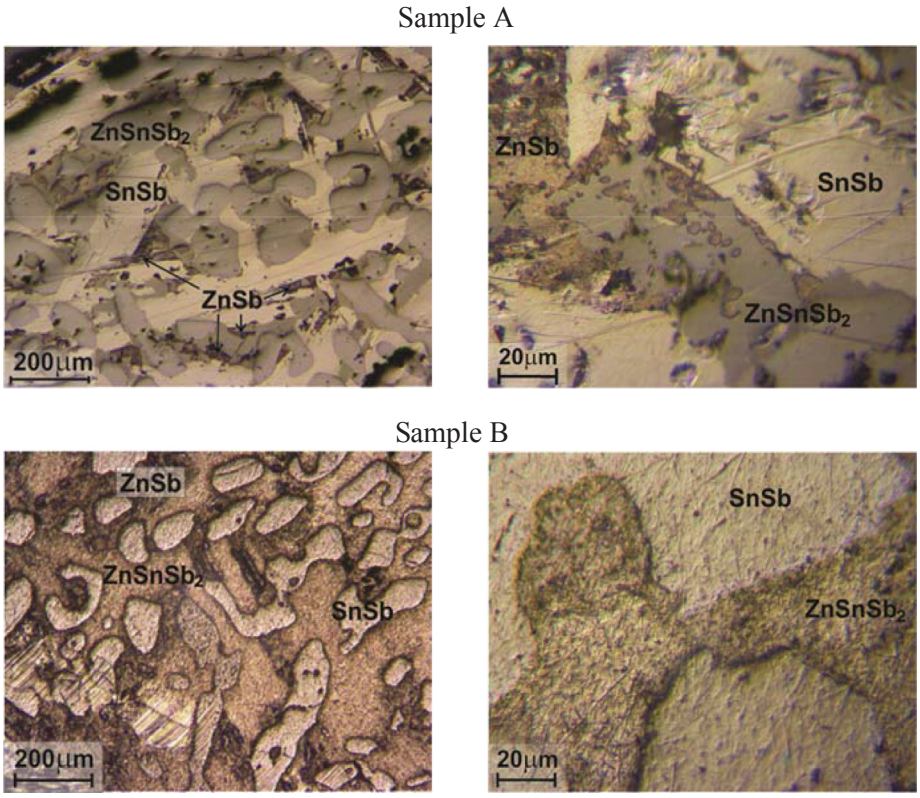

Fig. 2. Micrographs of the $ZnSnSb_2$ + Mn samples surfaces with magnifications of 50 × and 400×.

SnSb, which is related to a higher deficiency of Zn atoms, and therefore higher hole concentration. So, the different concentrations of free carriers in the samples are a consequence of various defects and microstructures which are formed.

In order to examine the interaction of free carriers and a lattice, the far-infrared reflectivity spectra in the range 40–450 cm^{-1} at room temperature have been recorded. Obtained spectra are shown in Fig. 4.

It is obvious that the most distinct difference between the spectra relates to wave numbers above 220 cm^{-1}, where the high carrier concentration has a main influence. Also, in the range from 120 to 180 cm^{-1} the spectrum for sample B (black line) contains some phonon lines which are absent or attenuated in the spectrum for sample A (red line).

A detailed analysis of the obtained results was necessary. For the analysis of the spectra the fitting procedure which includes plasmon - phonon interaction was applied.

4. Plasmon - phonon interaction

In materials with high free carrier concentration a plasmon-phonon interaction should be taken into account, as it significantly affects the properties of the material. Its influence on the dielectric properties of the material is important for the analysis of the reflection spectra.

A theoretical model of the dielectric function in bulk materials [22] has been applied. The dielectric function $\varepsilon(\omega)$ describes dielectric properties of single crystal and includes classical oscillators corresponding to the TO-modes, and Drude part which takes into account the free carrier contribution:

$$\varepsilon(\omega) = \varepsilon_\infty + \sum_{k=1}^{l} \frac{\varepsilon_\infty(\omega_{LOk}^2 - \omega_{TOk}^2)}{\omega_{TOk}^2 - \omega^2 - i\gamma_{TOk}\omega} - \frac{\varepsilon_\infty \omega_P^2}{\omega(\omega + i\Gamma_P)} \quad (1)$$

In this equation ε_∞ is the high-frequency dielectric constant, ω_{TOk} and ω_{LOk} are the transverse and longitudinal optical-phonon frequencies, l is the number of phonons,ω_P is the plasma frequency, γ_{TOk} and Γ_P are the phonon and plasmon damping. The use of such a dielectric function is valid in multiphase materials, since it is based on a phenomenological approach where the effective values of the material parameters are used, e.g. $\omega_p^2 = \omega_{p1}^2 + \omega_{p2}^2 + \omega_{p3}^2 + \cdots$.

As our $ZnSnSb_2$ + Mn samples have high concentration of free-carriers (p), and therefore high values of ω_P ($\omega_P{}^2 \sim p$), it is expected that plasma interacts with phonons. As a result the phonon frequencies are changed, i.e. their positions are shifted from the expected values. The phonon lines observed at the reflection spectra are these shifted modes i.e. coupled plasmon-phonon modes. So, the situation is much clearer if the dielectric function which takes a plasmon–phonon interaction in advance is used [23,24]. It also allows the possibilities that more than one phonon interact with plasma as well as existence of uncoupled phonons. That dielectric function is:

$$\varepsilon(\omega) = \varepsilon_\infty \frac{\prod_{j=1}^{n+1}(\omega^2 + i\gamma_{lj}\omega - \omega_{lj}^2)}{\omega(\omega + i\Gamma_P)\prod_{i=1}^{n}(\omega^2 + i\gamma_{ti}\omega - \omega_{ti}^2)} \cdot \prod_{k=1}^{s} \frac{\omega^2 + i\gamma_{LOk}\omega - \omega_{LOk}^2}{\omega^2 + i\gamma_{TOk}\omega - \omega_{TOk}^2} \quad (2)$$

The first fraction in Eq. (2) describes coupling of a plasmon and n LO phonons, where parameters ω_{lj} and γ_{lj} are eigenfrequencies and damping coefficients of the longitudinal component of the coupled phonons. ω_{ti} and γ_{ti} are frequencies and damping of transverse component of these phonons. Γ_p is the plasma damping. The second factor in Eq. (2) represents s uncoupled phonons of the crystal, wherein ω_{LOk} (ω_{TOk}) and γ_{LOk} (γ_{TOk}) are LO (TO) frequencies and damping coefficients of the k-th uncoupled phonon of the crystal.

The analysis of the obtained reflection spectra was performed by a fitting procedure, by adjusting the parameters of Eq. (2) in order to obtain a match between the experimental and theoretical curves. The values of ω_{lj} and ω_{ti} are directly obtained in this way while the ω_P and ω_{LO} values are calculated [25]. It can be seen that the positions of the ω_{l2} and ω_{l4} are significantly different for samples A and B. The behavior of phonons and interactions with plasma were analyzed based on the data thus obtained.

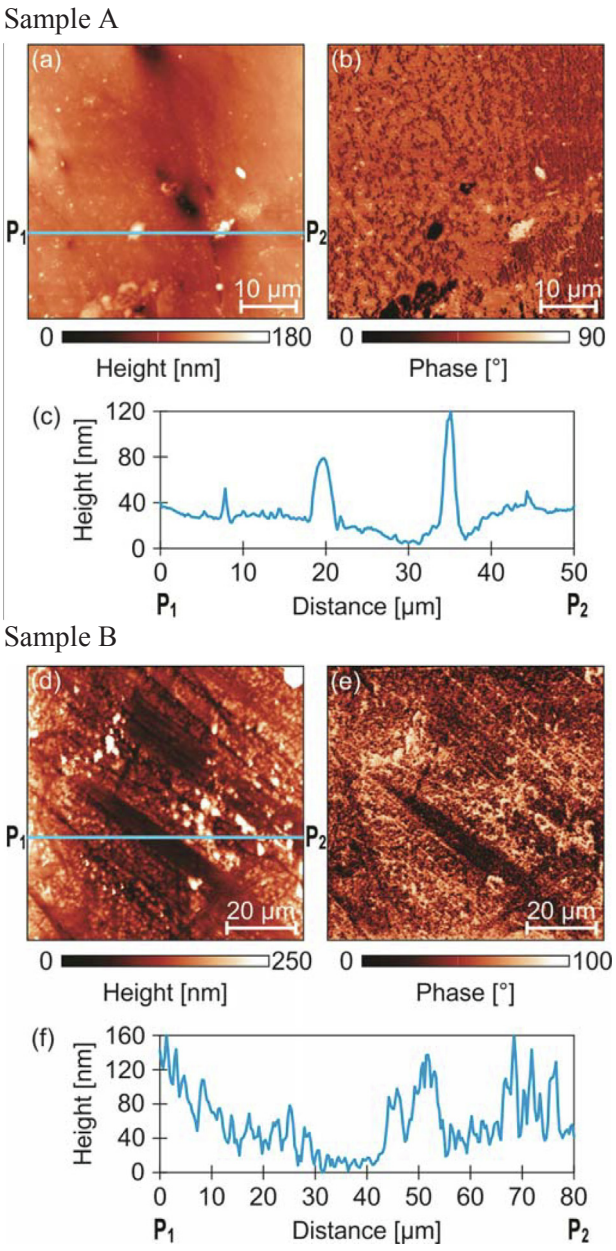

Fig. 3. (a) AFM topography and (b) corresponding phase-contrast image of sample A; (c) Height profile taken along the straight solid line in (a) from point P_1 to point P_2; Figures (d), (e), and (f) refer to sample B in the same way.

The phonons of $ZnSnSb_2$ which are IR active are known from literature [26], and they are of B_2 and E symmetries. Their estimated values are given in Table 1.

Plasmon - phonon interaction commonly refers to the coupling of the plasma and one phonon [27]. In that case two coupled modes appear ω_{l1} and ω_{l2}, often labeled as ω_+ and ω_-. In the case of $ZnSnSb_2$, based on data obtained by fitting procedure, it was established that the plasma interacts with three phonons of B_2 symmetry [28,29,30]. As a result of that their positions are shifted and instead three B_2 modes there are four coupled modes ω_{l1}, ω_{l2}, ω_{l3} and ω_{l4}. Obtained values are shown as black points in Fig. 6. Their positions are different for the two samples because of the different influences of the plasma ($\omega_P^2 \sim p$). Because of the high plasma frequency of sample A, the ω_{l4} has high value of 675 cm^{-1} which is outside of the measured range.

For ease of analysis, it is common to draw a dependency diagram of obtained parameters (ω_{lj}, ω_t, ω_{TO}, ω_{LO}) on plasma frequency ω_p, as

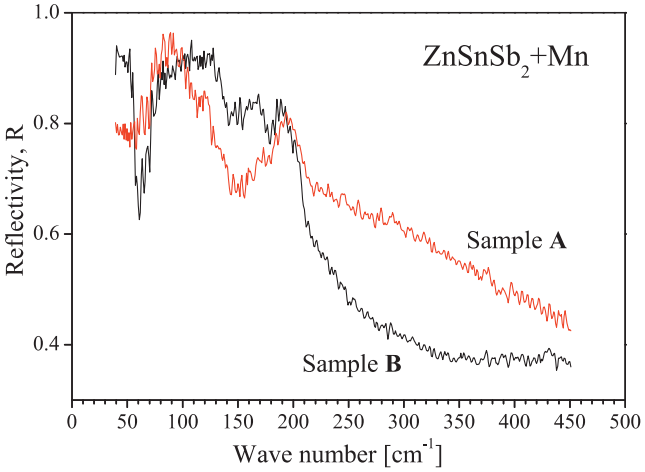

Fig. 4. Far-infrared reflectivity spectra of $ZnSnSb_2$ + Mn.

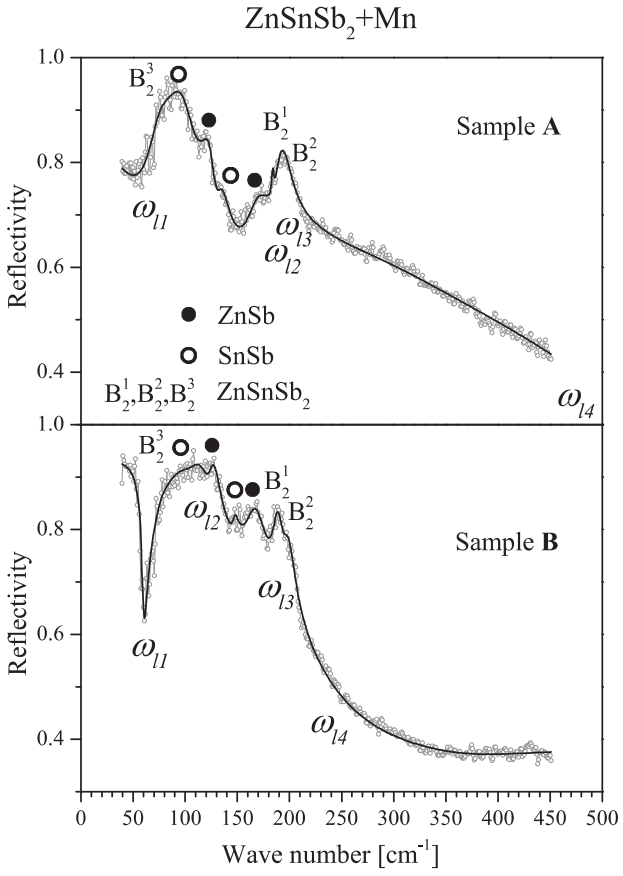

Fig. 5. Analyzed reflection spectra; experimental data are represented by circles while black lines are theoretical curves; registered optical phonons are indicated on the spectra.

shown in Fig. 6. The full lines are solutions of $Re\{\varepsilon(\omega)\} = 0$ from Eq. (1). It should be noted that line ω_{l3} between B_2^1 and B_2^2 phonons is barely visible because they are very close. The lines are calculated for five different values of plasma damping Γ_p (Fig. 6) ($\Gamma_p = 1/\tau$, where τ is a lifetime of plasmon). This was done to determine Γ_p interdependence with plasmon - phonon interaction.

The obtained values of plasma damping and plasma frequency of samples A and B are: $\Gamma_{pA} = 500$ cm^{-1}, $\Gamma_{pB} = 375$ cm^{-1}, $\omega_{pA} = 837$ cm^{-1} and $\omega_{pB} = 405$ cm^{-1}. It should be noted that these parameters represent the effective values that describe the sample as a

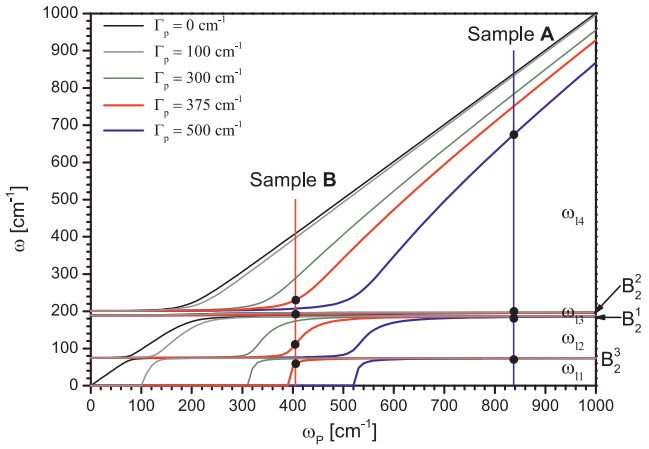

Fig. 6. Analysis of plasmon - three-phonons interaction; Full lines are obtained from Eq.(1), as the solutions of Re{$\varepsilon(\omega)$} = 0, for various values of Γ_p; Black points represent experimentally obtained data for ω_{lj} for both samples (Eq. (2)).

whole. It could be expected (based on p_A and p_B values and $\omega_p^2 \sim p$) that ω_{pA} and ω_{pB} differ about three times, which was not established. Plasma frequency is defined as $\omega_p^2 = (n_p e^2)/(\varepsilon_0 \varepsilon_\infty m_h^*)$, i.e. it includes other parameters of the material. Thus, by determining the plasma frequency and plasma damping the other properties of the material can be analyzed.

Besides phonons of B_2 symmetry which interact with plasma, other $ZnSnSb_2$ phonons are not registered on the IR reflectivity spectra. However, characteristic phonons of the other phases can be identified, as can be seen in Fig. 5. It was necessary that these phonons are not covered by the plasmon - phonon interaction. ZnSb modes are noticed at about 125 and 165 cm^{-1}, which is in agreement with results from the literature [31]. Two modes that correspond to SnSb phase are at about 94 and 145 cm^{-1}, which matches the previously obtained data [9,32]. The appearance of these modes is expected due to the significant presence of ZnSb and SnSb phases in the samples. MnSb phonons are not registered, i.e. it was not possible to discern them due to the small amount of that phase.

Based on the performed analyses, it can be seen that different microstructures formed in the investigated samples lead to high concentrations of free carriers, but which are ten times different from each other. Those high values cause plasmon - B_2 phonons interaction. That can be used to analyze optical and electrical properties of the materials, as well as other parameters, such as dielectric constants, effective mass of charge carriers and phonon lifetimes. In this way, the multiphase material with different microstructures was analyzed as a whole.

Investigation of thermoelectric properties of $ZnSnSb_2$ is a current issue [5,15,33]. The analysis of plasmon - phonon interaction performed in this paper can significantly assist in the study and understanding of thermoelectric processes in this as in other semiconducting polycrystalline materials [34].

5. Conclusion

Two samples of $ZnSnSb_2$ + Mn with different amounts of manganese were analyzed in this paper. The small difference in the initial composition of the material led to a difference of ten times in the free carrier concentrations. Their structural properties were examined by x-ray diffraction, optical microscopy, and AFM. Several different phases were registered - $ZnSnSb_2$, ZnSb, SnSb, and small amounts of Sn and MnSb. These phases form different microstructures, which is related to the large irregularities of the lattice. It was found that the high free carrier concentrations are caused by a large number of defects, especially zinc vacancies.

The optical characteristics of these multiphase materials were examined, whereby the samples were considered as a whole. Based on the analysis of IR reflection spectra the presence of a plasmon - phonons interaction was confirmed. It was determined that three $ZnSnSb_2$ phonons of B_2 symmetry interact with plasma, which led to the change of their positions. It is clear that strong plasmon - phonon interaction modifies optoelectronic properties of the $ZnSnSb_2$ + Mn samples, and that phonon positions depend on a free carrier concentration. A detailed analysis of this interaction also provides insight into the behavior of other material parameters, such as dielectric constants, effective mass of charge carriers and phonon lifetimes. Also, vibration modes of ZnSb and SnSb phases were registered on the spectra. Knowledge of phonon behavior in a material, as well as interaction with plasma, is very important for studying its thermoelectric properties.

Declaration of competing interest

The authors declare that there is no conflict of interest in this paper.

Acknowledgement

This work was supported under the Agreement of Scientific Collaboration between Polish Academy of Science and Serbian Academy of Sciences and Arts. The work in Serbia was supported by the Serbian Ministry of Education, Science and Technological Development through Project 45003.

Appendix A. Supplementary material

Supplementary data to this article can be found online at https://doi.org/10.1016/j.infrared.2020.103345.

References

[1] J.L. Shay, J.H. Wernick, Ternary Chalcopyrite Semiconductors: Growth, Electronic Properties, and Applications, Chapter 3 - Electronic Structure of II-IV-V_2 Compounds, Pergamon Press, New York, 1975, pp. 79–109 https://doi.org/10.1016/B978-0-08-017883-7.50008-1.
[2] W. Dobrowolski , J. Kossut, T. Story. II–VI and IV–VI Diluted Magnetic Semiconductors – New Bulk Materials and Low-Dimensional Quantum Structures. Handbook of Magnetic Materials 15 (2003) pp. 289-377, (Elsevier, Amsterdam, 2003). https://doi.org/10.1016/S1567-2719(03)15003-2.
[3] L. Kilanski, M. Górska, W. Dobrowolski, E. Dynowska, M. Wójcik, B.J. Kowalski, J.R. Anderson, C.R. Rotundu, D.K. Maude, S.A. Varnavskiy, I.V. Fedorchenko, S.F. Marenkin, Magnetism and magnetotransport of strongly disordered $Zn_{1-x}Mn_xGeAs_2$ semiconductor: The role of nanoscale magnetic clusters, J. Appl. Phys. 108 (2010) 073925, , https://doi.org/10.1063/1.3490231.
[4] S.F. Marenkin, A.D. Izotov, I.V. Fedorchenko, V.M. Novotortsev, Manufacture of magnetic granular structures in semiconductor-ferromagnet systems, Russ. J. Inorg. Chem. 60 (2015) 295300, , https://doi.org/10.1134/S0036023615030146.
[5] M. Ito, Y. Ohishi, H. Muta, K. Kurosaki, S. Yamanaka, Thermoelectric properties of Zn-Sn-Sb based alloys, Mater. Res. Soc. Symp. Proc. 1314 (2011), https://doi.org/10.1557/opl.2011.618.
[6] P. Balasubramanian, M. Battabyal, D. Sivaprahasam, R. Gopalan, On the formation of phases and their influence on the thermal stability and thermoelectric properties of nanostructured zinc antimonide, J. Phys. D: Appl. Phys. 50 015602 (11 (2017) pp), https://doi.org/10.1088/1361-6463/50/1/015602.
[7] G. Coquil, B. Fraisse, S. Biscaglia, D. Ayme-Perrot, M.T. Sougrati, L. Monconduit, $ZnSnSb_2$ anode: A solid solution behavior enabling high rate capability in Li-ion batteries, J. Power Sour. 441 (2019) 227165, , https://doi.org/10.1016/j.jpowsour.2019.227165.
[8] O. Zobac, J. Sopousek, J. Bursik, A. Zemanova, P. Roupcova, Experimental Study of the Sb-Sn-Zn Alloy System, Metall. Mater. Trans. 45A (2014) 1181–1188, https://doi.org/10.1007/s11661-013-2104-1.
[9] M. Romcevic, M. Gilic, L. Kilanski, W. Dobrowolski, I.V. Fedorchenko, S.F. Marenkin, N. Romcevic, Phonon properties of $ZnSnSb_2$ + Mn semiconductors: Raman spectroscopy, J. Raman Spectrosc. 49 (2018) 1678–1685, https://doi.org/10.1002/jrs.5421.
[10] L. Kilanski, M. Gorska, A. Slawska-Waniewska, S. Lewinska, R. Szymczak, E. Dynowska, A. Podgorni, W. Dobrowolski, U. Ralevic, R. Gajic, N. Romcevic, I.V. Fedorchenko, S.F. Marenkin, High temperature magnetic order in Zn_{1-x} Mn $_x$ $SnSb_2$ + MnSb nanocomposite ferromagnetic semiconductors, J. Phys.:Condens. Matter. 28 (2016) 336004, , https://doi.org/10.1088/0953-8984/28/33/336004.
[11] A. Tenga, F.J. Garcia-Garcia, A.S. Mikhaylushkin, B. Espinosa-Arronte, M. Andersson, U. Haussermann, Sphalerite – Chalcopyrite Polymorphism in Semimetallic $ZnSnSb_2$, Chem. Mater. 17 (2005) 6080–6085, https://doi.org/10.

1021/cm0516053.
[12] A. Tenga, F.J. Garcia-Garcia, Y. Wu, N. Newman, U. Haussermann, Metal-nonmetal transition in the sphalerite-type solid solution $[ZnSnSb_2]_{1-x}[2(InSb)]_x$, J. Solid State Chem. 182 (2009) 1438–1442, https://doi.org/10.1016/j.jssc.2009.03.015.
[13] M. Bostrom, S. Hovmoller, Preparation and Crystal Structure of the Pseudo-Decagonal Approximant Mn_3Ga_5, J. Solid State Chem. 153 (2000) 398–403, https://doi.org/10.1006/jssc.2000.8790.
[14] C. Wang, Y. Xu, S. Yang, H. Jiang, J. Li, J. Zhu, S. Yang, X. Liu, Experimental Determination of Phase Equilibria in the Sn-Zn-Sb System, J. Phase Equil. Diff. 36 (2015) 350–356, https://doi.org/10.1007/s11669-015-0387-1.
[15] A. Nomura, S. Choi, M. Ishimary, A. Kosuga, T. Chasapis, S. Ohno, G.J. Snyder, Y. Ohishi, H. Muta, S. Yamanaka, K. Kurosaki, Chalcopyrite $ZnSnSb_2$: A Promising Thermoelectric Material, ACS Appl. Mater. Interf. 10 (2018) 43682–43690, https://doi.org/10.1021/acsami.8b16717.
[16] V.N. Brudnyi, Electronic properties and pinning of the Fermi level in irradiated II–IV–V_2 semiconductors, Semiconductors 43 (2009) 1146–1154, https://doi.org/10.1134/S1063782609090085.
[17] V.G. Voevodin, S.N. Grinyaev, O.V. Voevodina, Nonstoichiometry and point defects in nonlinear optical crystals $A^2B^4C_2^5$, Mater. Sci. Semicond. Proces. 6 (2003) 385–388, https://doi.org/10.1016/j.mssp.2003.07.006.
[18] X. Song, M. Schrade, N. Maso, T.G. Finstad, Zn vacancy formation, Zn evaporation and decomposition of ZnSb at elevated temperatures: Influence on the microstructure and the electrical properties, J. Alloys Comp. 710 (2017) 762–770, https://doi.org/10.1016/j.jallcom.2017.03.339.
[19] L.V. Prokofieva, P.P. Konstantinov, A.A. Shabaldin, On the tin impurity in the thermoelectric compound ZnSb: Charge-carrier generation and compensation, Semicond 50 (2016) 741–750, https://doi.org/10.1134/S1063782616060208.
[20] L. Bjerg, G.K.H. Madsen, B.B. Iversen, Ab initio Calculations of Intrinsic Point Defects in ZnSb, Chem. Mater. 24 (2012) 2111–2116, https://doi.org/10.1021/cm300642t.
[21] B. Liu, J. Wu, Y. Cui, H. Wang, Y. Liu, Z. Wang, Z. Ren, G. Cao, Superconductivity in SnSb with a natural superlattice structure, Supercond. Sci. Technol. 31 (2018) 7, https://doi.org/10.1088/1361-6668/aae6fe 125011.
[22] Abstreiter G., Cardona M., Pinczuk A. Light scattering by free carrier excitations in semiconductors. In: Cardona M., Güntherodt G. (eds) Light Scattering in Solids IV. Topics in Applied Physics, vol 54. Springer, Berlin, Heidelberg. (1984) https://doi.org/10.1007/3-540-11942-6_20.
[23] A.A. Kukharskii, Plasmon-phonon coupling in GaAs, Solid State Commun. 13 (1973) 1761–1765, https://doi.org/10.1016/0038-1098(73)90724-2.
[24] N. Romcevic, M. Romcevic, W.D. Dobrovolski, L. Kilanski, M. Petrovic, J. Trajic, B. Hadzic, Z. Lazarevic, M. Gilic, J.L. Ristic-Djurovic, N. Paunovic, A. Reszka, B.J. Kowalski, I.V. Fedorchenko, S.F. Marenki, Far-infrared spectroscopy of Zn1 − xMnxGeAs2 single crystals: Plasma damping influence on plasmon – Phonon interaction, J. Alloys Comp. 649 (2015) 375–379, https://doi.org/10.1016/j.jallcom.2015.07.087.
[25] J. Trajic, N. Romcevic, M. Gilic, M. Petrovic Damjanovic, M. Romcevic, V.N. Nikiforov, Optical properties of $PbTe_{0.95}S_{0.05}$ single crystal at different temperatures: Far - infrared study, Optoelec. Adv. Mater. Rap. Comm. 6 (2012) 543–546.
[26] F.W. Ohrendorf, H. Haeuseler, Lattice Dynamics of Chalcopyrite Type Compounds. Part I. Vibrational Frequencies, Cryst. Res. Technol. 34 (1999) 339–349, https://doi.org/10.1002/(SICI)1521-4079(199903)34:3<339:: AID-CRAT339>3.0.CO;2-E.
[27] Klein M.V. Electronic Raman Scattering. In: Cardona M. (eds) Light Scattering in Solids. Topics in Applied Physics, vol 8. Springer, Berlin, Heidelberg (1975). https://doi.org/10.1007/978-3-540-37568-5_4.
[28] M. Petrovic, N. Romcevic, J. Trajic, W.D. Dobrowolski, M. Romcevic, B. Hadzic, M. Gilic, A. Mycielski, Far-infrared spectroscopy of $CdTe_{1-x}Se_x$(In): Phonon properties, Infrared Phys. Tech. 67 (2014) 323–326, https://doi.org/10.1016/j.infrared.2014.08.010.
[29] M. Romcevic, N. Romcevic, W. Dobrowolski, L. Kilanski, J. Trajic, D.V. Timotijevic, E. Dynowska, I.V. Fedorchenko, S.F. Marenkin, Optical properties and plasmon – Two different phonons coupling in ZnGeAs2 + Mn, J. Alloys Comp. 548 (2013) 33–37, https://doi.org/10.1016/j.jallcom.2012.09.017.
[30] I.J. Luxmoore, C.H. Gan, P.Q. Liu, F. Valmorra, P. Li, J. Faist, G.R. Nash, Strong coupling in the far-infrared between graphene plasmons and the surface optical phonons of silicon dioxide, ACS Photonics 1 (2014) 1151, https://doi.org/10.1021/ph500233s.
[31] D.V. Smirnov, D.V. Mashovets, S. Pasquier, J. Leotin, P. Puech, G. Landa, Yu.V. Roznovan, Long-wavelength optical phonons of $Cd_x Zn_{1-x}Sb$ mixed crystals, Semicond. Sci. Technol. 9 (1994) 333–337.
[32] P. Nithyadharseni, M.V. Reddy, B. Nalini, M. Kalpana, B.V.R. Chowdari, Sn-based Intermetallic Alloy Anode Materials for the Application of Lithium Ion Batteries, Electrochim. Acta 161 (2015) 261–268, https://doi.org/10.1016/j.electacta.2015.02.057.
[33] Yu M. Basalaev, Ab Initio Study of the $ZnSnSb_2$ Semiconductor, Semiconductors 52 (2018) 1715–1720, https://doi.org/10.1134/S1063782618130043.
[34] Q. Xu, J. Zhou, T.H. Liu, G. Chen, Effect of electron-phonon interaction on lattice thermal conductivity of SiGe alloys, Appl. Phys. Lett. 115 (2019) 023903, , https://doi.org/10.1063/1.5108836.

Република Србија
Универзитет у Београду
Факултет за физичку хемију
Д.Бр.2017/0307
Датум: 07.02.2020. године

На основу члана 29. Закона о општем управном поступку („Сл. гласник РС", бр.18/2016 и 95/2018) и службене евиденције издаје се

УВЕРЕЊЕ

Митрић (Миодраг) Јелена, бр. индекса 2017/0307, рођена 03.07.1993. године, Београд, Звездара, Република Србија, уписана школске 2019/2020. године, у статусу: финансирање из буџета: тип студија: докторске академске студије; студијски програм: Физичка хемија.

Према Статуту факултета студије трају (број година): три године.
Рок за завршетак студија: у двоструком трајању студија.

Ово се уверење може употребити за регулисање војне обавезе, издавање визе, права на дечији додатак, породичне пензије, инвалидског додатка, добијања здравствене књижице, легитимације за повлашћену вожњу и стипендије.

Овлашћено лице факултета

Република Србија
Универзитет у Београду
Факултет за физичку хемију
Д.Бр.2017/0307
Датум: 07.02.2020. године

На основу члана 29. Закона о општем управном поступку („Сл. гласник РС", бр.18/2016) и службене евиденције издаје се

УВЕРЕЊЕ

Митрић (Миодраг) Јелена, бр. индекса 2017/0307, рођена 03.07.1993. године, Београд, Звездара, Република Србија, уписана школске 2019/2020. године, у статусу: финансирање из буџета: тип студија: докторске академске студије; студијски програм: Физичка хемија.

Према Статуту факултета студије трају (број година): три године.
Рок за завршетак студија: у двоструком трајању студија.

Ово се уверење може употребити за регулисање војне обавезе, издавање визе, права на дечији додатак, породичне пензије, инвалидског додатка, добијања здравствене књижице, легитимације за повлашћену вожњу и стипендије.

Овлашћено лице факултета

Република Србија

УБ

Универзитет у Београду
Факултет за физичку хемију, Београд

Оснивач: Република Србија
Дозволу за рад број 612-00-02666/2010-04 од 10. децембра 2010.
године је издало Министарство просвете и науке Републике Србије

Диплома

Јелена, Миодраг, Митрић

рођена 3. јула 1993. године у Београду, Звездара, Република Србија, уписана школске 2012/2013. године, а дана 29. септембра 2016. године завршила је основне академске студије, првог степена, на студијском програму Физичка хемија, обима 240 (двеста четрдесет) бодова ЕСПБ са просечном оценом 9,14 (девет и 14/100).

На основу тога издаје јој се ова диплома о стеченом високом образовању и стручном називу

дипломирани физикохемичар

Број: 5948300
У Београду, 31. октобра 2016. године

Декан
Проф. др Гордана Ћирић-Марјановић

Ректор
Проф. др Владимир Бумбаширевић

00059163

Република Србија

УБ

Универзитет у Београду
Факултет за физичку хемију, Београд

Оснивач: Република Србија
Дозволу за рад број 612-00-02666/2010-04 од 10. децембра 2010. године је издало Министарство просвете и науке Републике Србије

Диплома

Јелена, Миодраг, Митрић

рођена 3. јула 1993. године у Београду, Звездара, Република Србија, уписана школске 2016/2017. године, а дана 29. јуна 2017. године завршила је мастер академске студије, другог степена, на студијском програму Физичка хемија, обима 60 (шездесет) бодова ЕСПБ са просечном оценом 9,25 (девет и 25/100).

На основу тога издаје јој се ова диплома о стеченом високом образовању и академском називу

мастер физикохемичар

Број: 6995000
У Београду, 18. јула 2017. године

Декан
Проф. др Гордана Ћирић-Марјановић

Ректор
Проф. др Владимир Бумбаширевић

00069726

УНИВЕРЗИТЕТ У БЕОГРАДУ

Адреса: Студентски трг 1, 11000 Београд, Република Србија
Тел.: 011 3207400; Факс: 011 2638818; E-mail: kabinet@rect.bg.ac.rs

ВЕЋЕ НАУЧНИХ ОБЛАСТИ ПРИРОДНИХ НАУКА

Београд, 2. јул 2020. године
02-07 Број: 61206-1720/4-20
МЦ

На основу члана 48 став 5 тачка 3 Статута Универзитета у Београду („Гласник Универзитета у Београду“, бр. 201/18) и члана 32 Правилника о докторским студијама на Универзитету у Београду („Гласник Универзитета у Београду“, бр. 191/16), а на захтев Факултета за физичку хемију, бр. 515/2 од 15. јуна 2020. године, Веће научних области природних наука, на седници одржаној 2. јула 2020. године, донело је

О Д Л У К У

ДАЈЕ СЕ САГЛАСНОСТ на одлуку Наставно-научног већа Факултета за физичку хемију о прихватању теме докторске дисертације ЈЕЛЕНЕ МИТРИЋ, под називом: „Структурна и оптичка својства полупроводничких наноматеријала: гадолинијум–цирконата и итријум-ванадата допираних еуропијумом, кадмијум-телурида и цинк-оксида модификованог рутенијумовим комплексима“ и одређивању проф. др Иване Стојковић Симатовић и др Небојше Ромчевића, научног саветника Универзитета у Београду-Института за физику за менторе.

П Р Е Д С Е Д Н И К В Е Ћ А
проф. др Надежда Недељковић

Доставити:
- Факултету
- архиви Универзитета

Република Србија
Универзитет у Београду
Факултет за физичку хемију
Број индекса: 2012/0004
Датум: 25.06.2020.

На основу члана 29. Закона о општем управном поступку („Сл. гласник РС", бр.18/2016 и 95/2018) и службене евиденције

УВЕРЕЊЕ О ПОЛОЖЕНИМ ИСПИТИМА

Јелена Митрић, име једног родитеља Миодраг, ЈМБГ 0307993715237, рођена 03.07.1993. године, Београд, општина Звездара, Република Србија, уписана школске 2012/13. године, дана 29.09.2016. године завршила је основне академске студије на студијском програму Физичка хемија, у трајању од четири године, обима 240 (двеста четрдесет) ЕСПБ бодова, и стекла стручни назив дипломирани физикохемичар. Током студија положила је испите из следећих предмета:

Р.бр.	Шифра	Назив предмета	Оцена	ЕСПБ	Фонд часова**	Датум
1.	07М1	Математика 1	9 (девет)	11	I:(60+60+0)	08.07.2013.
2.	07УСМ	Увод у структуру материје	10 (десет)	4	I:(30+30+0)	01.02.2013.
3.	07УЛР	Увод у лабораторијски рад	10 (десет)	4	I:(15+0+90)	30.01.2013.
4.	07ОКФХ1	Општи курс физичке хемије 1	9 (девет)	7	I:(60+0+60)	21.02.2013.
5.	07ПМФХ	Практикум из математике за физикохемичаре	9 (девет)	4	I:(15+30+0)	31.01.2013.
6.	07ХТД	Хемијска термодинамика	10 (десет)	6	II:(60+0+60)	25.06.2013.
7.	07НХ	Неорганска хемија	9 (девет)	6	II:(60+0+0)	01.07.2013.
8.	07Ф1	Физика 1	10 (десет)	7	II:(45+30+30)	13.09.2013.
9.	07ОКФХ2	Општи курс физичке хемије 2	8 (осам)	7	II:(60+0+60)	28.06.2013.
10.	07ПКР	Практикум из коришћења рачунара	10 (десет)	4	II:(15+0+30)	19.06.2013.
11.	07КОЛ	Колоиди	10 (десет)	4	III:(15+0+30)	30.01.2014.
12.	07ЕЈ1	Енглески језик 1	10 (десет)	2	III:(30+30+0)	29.01.2014.
13.	07М2	Математика 2	7 (седам)	10	III:(60+60+0)	28.01.2014.
14.	07Ф2	Физика 2	9 (девет)	7	III:(45+30+30)	04.07.2014.
15.	07КАХ	Класична аналитичка хемија	9 (девет)	7	III:(30+0+90)	14.07.2014.
16.	07Ф3	Физика 3	10 (десет)	6	IV:(45+15+30)	29.08.2014.
17.	07ЕЈ2	Енглески језик 2	10 (десет)	1,5	IV:(30+30+0)	24.06.2014.
18.	07АТ	Атомистика	10 (десет)	10,5	IV:(60+15+60)	26.06.2014.
19.	07УФХЖС2	Увод у физичку хемију животне средине	10 (десет)	4	IV:(15+0+30)	28.06.2014.
20.	07ОХ	Органска хемија	7 (седам)	8	IV:(60+0+60)	16.09.2014.
21.	07СТД	Статистичка термодинамика	9 (девет)	7	V:(60+30+0)	29.01.2015.
22.	07ФХП	Физичка хемија плазме	10 (десет)	5	V:(30+0+30)	06.02.2015.
23.	07РНХ	Радиохемија и нуклеарна хемија	9 (девет)	7	V:(60+0+60)	09.02.2015.
24.	07АСХ	Атомска спектрохемија	10 (десет)	7	V:(60+0+60)	22.06.2015.
25.	07БХ	Биолошка хемија	10 (десет)	4	V:(30+0+30)	02.02.2015.
26.	07ХК	Хемијска кинетика	7 (седам)	8	VI:(60+0+60)	05.02.2016.
27.	07МСХ	Молекулска спектрохемија	8 (осам)	8	VI:(60+0+60)	18.09.2015.
28.	07ЕХ	Електрохемија	8 (осам)	8	VI:(60+0+60)	26.08.2015.
29.	07ПРФХ	Примена рачунара у физичкој хемији	10 (десет)	6	VI:(60+30+0)	17.06.2015.
30.	07БФХ1	Биофизичка хемија 1	9 (девет)	7	VII:(60+0+60)	26.02.2016.

Овлашћено лице факултета

Р.бр.	Шифра	Назив предмета	Оцена	ЕСПБ	Фонд часова**	Датум
31.	07ОФ	Основи фотохемије	10 (десет)	5,5	VII:(30+0+0)	19.02.2016.
32.	07ФОРФХ	Форензичка физичка хемија	10 (десет)	5,5	VII:(30+0+30)	04.02.2016.
33.	07ММФХ	Математичке методе у физичкој хемији	10 (десет)	5	VII:(60+30+0)	06.02.2016.
34.	07КХ	Квантна хемија	6 (шест)	7	VII:(60+60+0)	04.07.2016.
35.	07ФХА	Физичкохемијска анализа	7 (седам)	7	VIII:(60+0+60)	08.07.2016.
36.	07ФХЧС	Физичка хемија чврстог стања	9 (девет)	7	VIII:(60+0+60)	14.07.2016.

* - еквивалентиран/признат испит.

** - Фонд часова је у формату (предавања+вежбе+остало).

Укупно остварено 247 ЕСПБ.
Општи успех: 9,14 (девет и 14/100) , по годинама студија (9,40, 9,20, 9,00, 8,71).
Завршни рад одбрањен је дана 29.09.2016. године са оценом 10 (десет).

Овлашћено лице факултета

Република Србија
Универзитет у Београду
Факултет за физичку хемију
Број индекса: 2017/0307
Датум: 07.02.2020.

На основу члана 29. Закона о општем управном поступку („Сл. гласник РС", бр.18/2016 и 95/2018) и службене евиденције

УВЕРЕЊЕ О ПОЛОЖЕНИМ ИСПИТИМА

Јелена Митрић, име једног родитеља Миодраг, рођена 03.07.1993.године, Београд, Звездара, Република Србија, уписана школске 2017/2018. године на докторске академске студије, школске 2019/2020. године уписана на статус финансирање из буџета, студијски програм Физичка хемија, током студија положила је испите из следећих предмета:

Р.бр.	Шифра	Назив предмета	Оцена	ЕСПБ	Фонд часова**	Датум
1.	ДІЗММФХИ	Математичке методе у физичкохемијским истраживањима	9 (девет)	15	I:(75+0+225)	05.02.2018.
2.	ДІЗНФМ	Нове физичкохемијске методе	9 (девет)	15	II:(75+0+225)	25.07.2018.
3.	ДІЗИПФ	Примењена фотохемија	10 (десет)	9	III:(45+0+120)	30.09.2019.
4.	ДІЗИССКАМ	Синтеза, структура и својства кристалних и аморфних материјала	9 (девет)	9	III:(45+0+120)	27.09.2019.

* - еквивалентиран/признат испит.
** - Фонд часова је у формату (предавања+вежбе+остало).

Укупно остварено 108 ЕСПБ.
Општи успех: 9,25 (девет и 25/100) , по годинама студија (9,00, 9,50, /).
Настава на овим студијама траје три године.

Овлашћено лице факултета

Република Србија
Универзитет у Београду
Факултет за физичку хемију
Број индекса: 2016/0204
Датум: 25.06.2020.

На основу члана 29. Закона о општем управном поступку („Сл. гласник РС", бр.18/2016 и 95/2018) и службене евиденције

УВЕРЕЊЕ О ПОЛОЖЕНИМ ИСПИТИМА

Јелена Митрић, име једног родитеља Миодраг, ЈМБГ 0307993715237, рођена 03.07.1993. године, Београд, општина Звездара, Република Србија, уписана школске 2016/17. године, дана 29.06.2017. године завршила је мастер академске студије на студијском програму Физичка хемија, у трајању од једне године, обима 60 (шездесет) ЕСПБ бодова, и стекла академски назив мастер физикохемичар. Током студија положила је испите из следећих предмета:

Р.бр.	Шифра	Назив предмета	Оцена	ЕСПБ	Фонд часова**	Датум
1.	М13ФХАНМ	Физичкохемијски аспекти науке о материјалима	9 (девет)	9	I:(75+0+180)	28.03.2017.
2.	М13ММФХИ	Методе и методологија физичкохемијских истраживања	9 (девет)	7	I:(45+0+150)	13.02.2017.
3.	М13ДЗПМ	Дифракција X-зрака на прашкастим материјалима	10 (десет)	7	II:(45+0+180)	20.06.2017.

* - еквивалентиран/признат испит

** - Фонд часова је у формату (предавања+вежбе+остало).

Укупно остварено 60 ЕСПБ.
Општи успех: 9,25 (девет и 25/100) , по годинама студија (9,33).
Завршни - мастер рад одбрањен је дана 29.06.2017. године са оценом 9 (девет).

Овлашћено лице факултета